Taylor-Aris Dispersion in Microfluidic Networks

by

Kevin David Dorfman

M.S., Massachusetts Institute of Technology (2001)
B.S., The Pennsylvania State University (1999)

Submitted to the Department of Chemical Engineering
in partial fulfillment of the requirements for the degree of

Doctor of Philosophy

at the

MASSACHUSETTS INSTITUTE OF TECHNOLOGY

September 2002

Signature of Author .....
Department of Chemical Engineering
23 July 2002

Certified by .....
Howard Brenner
Willard H. Dow Professor of Chemical Engineering
Thesis Supervisor

Accepted by .....
Daniel Blankschtein
Professor of Chemical Engineering
Chairman, Committee for Graduate Students

Taylor-Aris Dispersion in Microfluidic Networks

by

Kevin David Dorfman

Submitted to the Department of Chemical Engineering
on 23 July 2002, in partial fulfillment of the
requirements for the degree of
Doctor of Philosophy

Abstract

This thesis constitutes the development and application of a theory for the lumped parameter, convective-diffusive-reactive transport of individual, non-interacting Brownian solute particles ("macromolecules") moving within spatially periodic, solvent-filled networks — the latter representing models of chip-based microfluidic devices, as well as porous media. The use of a lumped parameter transport model and network geometrical description affords the development of a discrete calculation scheme for computing the relevant network-scale (macrotransport) parameters, namely the mean velocity vector $\bar{\mathbf{U}}^*$, dispersivity dyadic $\bar{\mathbf{D}}^*$ and, if necessary, the mean volumetric solute depletion rate $\bar{K}^*$. The ease with which these discrete calculations can be performed for complex networks renders feasible parametric studies of potential microfluidic chip designs, particularly those pertinent to biomolecular separation schemes.

To demonstrate the computational and conceptual advantages of this discrete scheme, we consider: (i) a pair of straightforward examples, dispersion analysis of (non-reactive) pressure-driven flow in spatially periodic serpentine microchannels and reactive transport in an elementary geometric model of a porous medium; and (ii) a pair of case studies based upon the microfluidic separation techniques of vector chromatography and entropic trapping. The straightforward examples furnish explicit proof that the present theory produces realistic results within the context of a simple computational scheme, at least when compared with the prevailing continuous generalized Taylor-Aris dispersion theory. In the case study on vector chromatography, we identify those factors which break the symmetry of the chip-scale particle mobility tensor, most importantly the hydrodynamic wall effects between the particles and the obstacle surfaces. In the entropic trapping case study, analytical expressions derived for the solute dispersivity, number of theoretical plates, and separation resolution are shown to furnish results that accord, at least qualitatively, with experimental trends and data reported in the literature.

Thesis Supervisor: Howard Brenner
Title: Willard H. Dow Professor of Chemical Engineering

Dedicated in loving memory to Herman Zeenberg.

We have a habit in writing articles published in scientific journals to make the work as finished as possible, to cover up all the tracks, to not worry about the blind alleys or describe how you had the wrong idea first, and so on. So there isn't any place to publish, in a dignified manner, what you actually did in order to get to do the work.

— Richard Feynman, Nobel Lecture, 1966.

Acknowledgements

First and foremost, I would like to thank Professor Brenner for creating what can only be described as the ideal atmosphere for conducting graduate research. Probably the most difficult part of working with him was distilling a coherent research program from the the innumerable topics that we discussed over the past few years. I always felt that I was working *with* Professor Brenner, rather than *for* him. His physical insights and criticisms, always focusing upon the fundamentals of the problem rather than its details, forced me to sharpen my own arguments and then stand up for them in the face of sometimes insistent opposition. Aside from these purely academic issues, the personal benefits of my daily interactions with Professor Brenner cannot be underestimated. He has acted at times as a father, at times as a friend, and always in my best interests. I only hope that, given the opportunity to be in his shoes, I can do half the job that he does on a daily basis.

I would also like to thank Professors William Deen, Howard Stone, and Patrick Doyle for taking time out of their busy schedules to serve on my thesis committee. Their input on the direction of my research, as well as my postdoc search, were especially appreciated. In this context, I would also like to thank Ali Nadim, who served on my thesis committee while he was at Boston University, and Sangtae Kim, who, while not formally a member of the committee, provided advice and encouragement.

The Brenner group, which during my tenure has included Carlos Rinaldi, Jim Bielenberg, Lino Gonzalez, Ehud Yariv and Brian Rush, made it a joy to come into work everyday. Whether discussing volume-averaged velocity, the direction of the field of chemical engineering, or why we would never move back to Houston, my interactions with these friends and collegues have made life in 66-569 a memorable time. I would also like to thank Professor Venkat Ganesan, who acted as a "senior group member," providing me with much needed advice on coursework, how to work with Brenner, and my future career plans.

The chemical engineering staff has been an outstanding resource during my time at MIT. In particular, I would like to acknowledge Joan Chisolm and Arline Benford for their help and companionship.

My family has always been very supportive of my academic pursuits. I am grateful for their encouragement, even if my sisters have not always been entirely thrilled about how far away (geographically) my academic career has taken me. Don't forget girls — you can always visit!

Of course, my time at MIT would not have been the same without the companionship of the many people I have been fortunate enough to interact with over the past few years. While any list of this type is doomed to be incomplete, mine would certainly include the members of the Brenner group, Mark Delong, Anish Goel, Murray Height, Kim and Martin Kosto, Tom Lancaster, Scott Phillips, Ley Richardson, April Ross, Patty Sullivan, Mike Timko, Steve Weiss, Paul Yelvington, and Todd Zion. Also, much thanks to hoops@mit.edu and the Thirsty Ear for all the fun times.

Finally, thanks to Ali Borhan for giving me a reason to come to MIT, and Jean-Louis Viovy for giving me a reason to leave.

This work was partially supported by a Graduate Research Fellowship from the National Science Foundation. The finanical support of Eli Lilly & Company, in the form of a grant to Howard Brenner to encourage microfluidic research, is greatly appreciated.

Foreword

Portions of this thesis have appeared (or will appear) in print in various journals. The general theory for convective-diffusive transport in microfluidic networks, which comprises much of Chapter 1, Chapters 3-5, and the example of dispersion in serpentine microchannels appearing in Chapter 8, was published in Physical Review E (Dorfman & Brenner 2002a). The application of this theory to vector chromatography, the subject of Chapter 9, also appeared in Physical Review E (Dorfman & Brenner 2002c). Portions of the entropic trapping modeling in Chapter 10 appeared in Biomedical Microdevices (Dorfman & Brenner 2002b). The extensions to reactive transport, which constitute the remainder of Chapters 1, 3 and 4, all of Chapter 6, and the second example in Chapter 8, are the basis of a manuscript under review for publication in SIAM Journal on Applied Math (Dorfman & Brenner 2002d) at the time of this writing.

Contents

List of Figures

List of Tables

Part I

Theory

Chapter 1

Introduction

The engineering design and analysis of spatially periodic microfluidic separation devices requires characterizing the functional dependence of chip-scale (L-scale) mean solute transit rates across the device upon the prescribed interstitial-scale (l-scale; $l \ll L$) parameters quantifying the repetitive unit cell configuration and local transport properties of the several distinct (macromolecular) solutes to be separated as these molecules traverse the fluid-filled interstitial space. As is often the case in such modeling schemes, a rigorous, pointwise ("continuous") description of the l-scale transport within the network tends to be exceedingly difficult (if at all possible), owing in large measure to incomplete knowledge of the detailed mechanisms quantifying the transport of flexible polymeric or biological molecules within constraining geometries. Consequently, the rigor implicit in any continuous model for predicting the L-scale solute transport across the chip as a whole, such as is embodied in classical generalized Taylor-Aris dispersion theory (Brenner & Edwards 1993), is often negated by the need to invoke coarse, *ad hoc* assumptions regarding the physical nature of the local solute transport processes, such as employing a (scalar) mean electrophoretic solute mobility in lieu of the exact pointwise mobility dyadic. This thesis aims to incorporate, *a priori*, all of our ignorance of the detailed phenomenology underlying these local issues into a discrete network theory, rendering the latter analytically and computationally tractable when compared with the more rigorous

continuous descriptions (Brenner & Edwards 1993) of such spatially periodic networks.

The analysis which follows is focused primarily upon a theory for modeling microfluidic chromatographic separation devices embossed on chips, with a subsequent extension of the latter (purely) convective-diffusive network scheme to account for the depletion of physicochemically reactive solutes within the network, either via chemical reaction or by irreversible adsorption onto the walls of the medium. In the context of chromatographic separations, micropatterned media find ready application as vector chromatographic separation devices (Dorfman & Brenner 2001), wherein the distinct species undergo simultaneous directional and temporal separation. By "directional" is meant that, on the L-scale, different species move in different directions in response to the animating force. In contrast, "temporal" separation refers to the fact that even if the several species move, on average, in the same direction, they generally do so at different *speeds*, thereby effecting their separation in time, such as occurs in conventional scalar (or unidirectional) chromatography. Experiments performed by Chou *et al.* (1999, 2000) on these micropatterned devices demonstrated the efficient separation of variable-length DNA strands.

Previous attempts to model such directional separation phenomena include our application of rigorous continuous Taylor-Aris dispersion theory (Dorfman & Brenner 2001), as well as more intuitive models developed independently by Duke & Austin (1998) and Ertas (1998). In addition to being directly applicable to the phenomenon of vector chromatography, the generic theory to be developed herein lends itself to applications involving other classes of microfluidic separation devices, such as magneto-sensitive arrays (Doyle *et al.* 2002) and entropic trapping devices (Han & Craighead 2000), as well as furnishing an elementary model for transport in porous media. Applications of the present theory to specific examples will be discussed in Part II of this thesis.

In the context of reactive networks, the integration of microscale reaction protocols with downstream microfluidic chromatographic separation techniques has spearheaded the development of miniaturized total analysis systems (μ-TAS) (Jakeway *et al.* 2000,

Krishnan *et al.* 2001, Kutter 2000) directed towards low-volume (point-of-use) chemical processes and biological assays in microchip environments. Constructing such devices with precision microfabrication techniques enables the creation of highly reproducible periodic microscale structures of any mode of arrangement, whose unit cell configurations can be designed for optimal performance. Concurrently, the relatively new field of "microreaction engineering" (Jensen 2001) has employed these fabrication techniques to produce increasingly complex microscale reactor architectures. Apart from these explicit μ-TAS and microreaction engineering applications, the generic paradigm to be developed is expected to be of broader interest in applications lying outside of these fields, such as the reactive solute transport in porous media which occurs in groundwater contamination.

To the extent that Taylor-Aris dispersion theory (Brenner & Edwards 1993) provides an adequate description of the global aspects of the solute transport processes occurring within the network, only three parameters are required to quantify the average L- or chip-scale solute transport rates: (i) the mean solute depletion rate $\bar{K}^*$, representing the exponential decay of the total solute concentration field or, equivalently, the decay of the individual solute survival probability density; (ii) the mean solute velocity vector $\bar{\mathbf{U}}^*$, representing the coefficient of the asymptotic L-scale linear temporal growth in time of the mean vector displacement of the solute particle from the point of its initial introduction into the network; and (iii) the solute dispersivity dyadic $\bar{\mathbf{D}}^*$, comparably representing the corresponding growth in time of the solute's mean-squared dyadic deviation from its current mean position. In the context of chromatographic separations, as embodied by the representative data depicted in Fig. 1-1, the latter parameters serve to characterize the separation in the following manner: The vector velocity difference $\bar{\mathbf{U}}_1^* - \bar{\mathbf{U}}_2^*$ between two distinct solute "molecules" or species 1 and 2, introduced simultaneously, quantifies the relative separation occurring between them as they traverse the network. Similarly, the respective particle dispersivities, say, $\bar{\mathbf{D}}_1^*$ and $\bar{\mathbf{D}}_2^*$, serve to characterize the extent of band-broadening of these solutes, arising from the stochastic nature of the solute transport processes occurring within the network. Computing these global param-

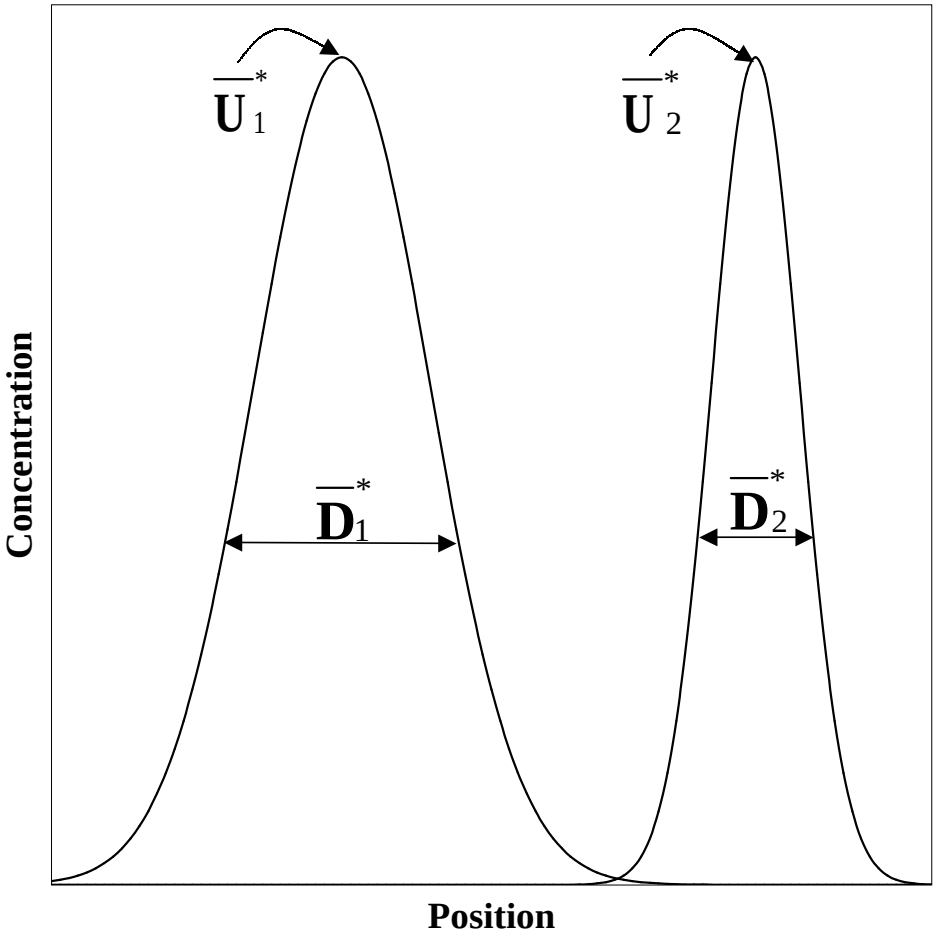

Figure 1-1: Representative data for the chromatographic separation of two distinct macromolecular species, 1 and 2. The relative band peaks and widths are characterized by the species mean velocities, $\bar{\mathbf{U}}_i^*$, and dispersivities, $\bar{\mathbf{D}}_i^*$, respectively.

eters from knowledge of the detailed microscale (unit cell) parameters characterizing the device necessitates creating theoretical tools sufficient to do justice to the technological advances implicit therein, while at the same time being sufficiently simple to render the computations tractable. This is the goal of Part I of this thesis.

1.1 Review of Network Models

Network models, albeit typically devoid of rigorous Taylor-Aris foundations, have been applied previously to a vast array of practical problems, including transport in porous media (Adler & Brenner 1984a,b,c, Aviles & Levan 1991, de Arcangelis *et al.* 1986, Fatt 1956, Koplik 1982, Koplik *et al.* 1988, Saffman 1959, Sahimi 1992, Sahimi & Jue 1989) and fractal models thereof (Adler 1985a,b,c), deep-bed filtration (Imdakm & Sahimi 1991, Rege & Fogler 1988), soil science (Berkowitz & Ewing 1998, Bruderer & Bernabe 2001), and various chromatographic separation schemes (Andrade *et al.* 1992, McGreavy *et al.* 1990, Meyers & Liapis 1998). Early work in these fields is reviewed by van Brakel (1975). To date, the majority of these network analyses have focused primarily upon dispersion in random porous media (Aviles & Levan 1991, Bruderer & Bernabe 2001, de Arcangelis *et al.* 1986, Koplik 1982, Koplik *et al.* 1988, Sahimi 1992, Sahimi *et al.* 1983, Sahimi & Jue 1989, Sorbie & Clifford 1991), or upon the inherent disorder prevailing in packed bed chromatographic separation devices (Andrade *et al.* 1992, McGreavy *et al.* 1990, Meyers & Liapis 1998), with much attention focused upon the solute dispersivity in such networks near the percolation threshold (Bruderer & Bernabe 2001, Imdakm & Sahimi 1991, Koplik *et al.* 1988, Sahimi 1992, Zhang & Seaton 1994). Moreover, network models (Adler & Brenner 1984a,b,c, Adler 1985a,b,c, Aviles & Levan 1991, Bruderer & Bernabe 2001, de Arcangelis *et al.* 1986, Fatt 1956, Imdakm & Sahimi 1991, Koplik 1982, Koplik *et al.* 1988, Meyers & Liapis 1998, Saffman 1959, Sahimi *et al.* 1983, Sorbie & Clifford 1991) have heretofore dealt mostly with unidirectional, pressure-driven, "piggy-back" solute transport through the network. In such circumstances, the mean particle motion has

invariably been regarded as being colinear with the Darcy-scale (L-scale) solvent pressure gradient, a phenomenon which is not generally true of vector chromatographic separations (when the externally applied field is viewed as analogous to a Darcy-scale pressure gradient). For reactive media, various homogenization procedures, again devoid of our rigorous Taylor-Aris network formalism, have previously been invoked to study catalysis (Andrade *et al.* 1997, Hollewand & Gladden 1992, Park & Kim 1984, Ryan *et al.* 1980, Sahimi *et al.* 1990, Wakad & Nardse 1974, Zhang & Seaton 1994), reduced kinetic models (Li & Rabitz 1991), transport in chemical reactors and porous media (Alvarado *et al.* 1997, Balakotaiah & Dommeti 1999, Dungan *et al.* 1990, Edwards *et al.* 1993, Ginn 2001, Hollewand & Gladden 1992, Mauri 1991, Mehta *et al.* 1988, Pal 1999, Sahimi *et al.* 1990), and irreversible adsorption phenomena (Aviles & Levan 1991, Leitzelement *et al.* 1984, Rege & Fogler 1988, Sahimi *et al.* 1990, Suchomel *et al.* 1998). One particularly interesting use of the notion of homogenization involves extracting macroscopically observable reaction rates from molecular-scale models of coupled reaction-diffusion phenomena (Cukier 1983a,b, Kruger 1990a,b, Mattern & Felderhof 1987, Muthukumar 1982).

In contrast will all but two (Adler & Brenner 1984b, Adler 1985b) of the preceding network analyses, we here apply a rigorous Taylor-Aris-like "method-of-moments" L-scale scheme to the lumped-parameter, l-scale transport processes occurring within the spatially periodic network[1] — ultimately deriving a generic paradigm for calculating the physically relevant macroscopic parameters, namely $\bar{K}^*$, $\bar{\mathbf{U}}^*$ and $\bar{\mathbf{D}}^*$, from knowledge of the prescribed l-scale data. Building upon the discrete framework of Adler & Brenner (1984b), the present contribution relaxes their assumption of perfect mixing at the intersections of the individual channels, in addition to incorporating molecular diffusion within the channels and chemical reactions into the analysis. With the exceptions (Adler & Brenner 1984b, Adler 1985b) cited above, our discretization contrasts with existing

[1]Such a regular, spatially periodic network theory may be employed in the modeling of "random" media by sampling numerous realizations of the randomly configured contents of unit cells, in the spirit of tube radii distributions employed elsewhere in capillary models of porous media [see, for example, (Koplik 1982)].

generalized Taylor-Aris dispersion theory analyses (Brenner & Edwards 1993), which are predicated upon a precise, pointwise, continuous description of the l-scale transport phenomena occurring in spatially periodic media. Accordingly, the generalized Taylor-Aris dispersion paradigm developed herein represents a complete discretization of the comparable classical continuous paradigm (Brenner 1980) — the present graph-theoretical framework being motivated by the creation of classes of perfectly periodic chromatographic devices (Chou *et al.* 1999, 2000, Doyle *et al.* 2002, Han & Craighead 2000). Moreover, the concomitant analytical difficulties posed by the geometric complexities of such microfluidic devices (Dorfman & Brenner 2001) motivates the subsequent use of experimentally measurable, albeit averaged, discrete l-scale transport parameters in place of classical continuous l-scale transport data.

All network models, including ours, proceed in a similar fashion, initially requiring three l-scale data inputs pertaining to: (i) the l-scale description of the entraining solvent flow field, such as that determined by an electrical resistance analog (Adler & Brenner 1984a, Adler 1985a,c, Koplik 1982) for fluid motion animated by a Darcy-scale pressure gradient; (ii) the l-scale solute transport parameters, namely the mean, interstitial-level particle velocity vector and diffusivity (dispersivity) dyadic prevailing within the individual channels of the network, as well as the local reaction rate; and (iii) the selection of a so-called "mixing" rule characterizing the choice of solute intersectional exiting protocol from the channel junctions wherein the l-scale channel contents coalesce.

1.2 Interstitial Transport Phenomena

Disagreement exists in the network modeling literature concerning delineation of the l-scale (effective) intrachannel transport processes, with existing models employing either molecular properties (Bruderer & Bernabe 2001, de Arcangelis *et al.* 1986, Zhang & Seaton 1994) or effective Taylor-Aris dispersion properties (Andrade *et al.* 1992, Koplik *et al.* 1988, McGreavy *et al.* 1990, Sahimi 1992, Sahimi & Jue 1989, Sorbie & Clifford

1991). As such, it behooves us to amplify, during the course of the subsequent analysis, the relationship existing between the effective intrachannel solute velocity and diffusivity (dispersivity) and the comparable pointwise particle velocity vector and molecular diffusivity dyadic appearing in the continuous scheme. The latter pair of microtransport parameters, $\mathbf{U}(\mathbf{r})$ and $\mathbf{D}(\mathbf{r})$, are, in principle, exactly expressible functionally in terms of the continuous l-scale local particle position vector $\mathbf{r}$ within the repetitive unit cell. In contrast, because of their coarser discrete l-scale nature, the effective channel transport parameters, $\mathbf{U}(j)$ and $\mathbf{D}(j)$, cannot be known exactly owing to the uncertainty existing in the instantaneous local position $\mathbf{r}$ of the particle within channel j arising from the stochastic nature of the molecular diffusive transport processes. For example, the transport of an entrained (point-size) particle by a parabolic Poiseuille flow field may take place entirely along the channel center, resulting thereby in a mean channel velocity significantly greater than that for a particle moving proximate to the channel walls. Such effects become more pronounced in the context of finite-size particles, wherein hydrodynamic wall effects induced by the finite size of the particles relative to the channel width (Happel & Brenner 1983) must be incorporated into the analysis.[2] This is especially true in the case of force-driven particle animation or electroosmotic flow (Russel *et al.* 1989), where wall effects constitute the *only* mechanism enabling particle vector separation. The possibility that a particle will statistically sample the entire cross-sectional area of a given channel before exiting that channel, as required for Taylor-Aris theory to be applicable, necessarily decreases monotonically with the channel's longitudinal dimension — increasing thereby the likelihood of the particle spending a statistically inordinate time resident on a given streamline, or too long in a region of unchanging mobility in the finite-size particle case. Even more tenuous than in the preceding case of modeling the solute velocity in a channel is the issue of properly defining the channel dispersivity,

[2]In the case of pressure-driven flow, the finite size of the particles results in a sterically excluded particle region, comprised of the slow-moving fluid streamline region near the wall, rendering the area-averaged mean velocity of the particle greater than that of the entraining fluid (Brenner & Gaydos 1977, Dimarzio & Guttman 1970). The latter phenomenon constitutes the dominant, first-order separation mechanism underlying (unidirectional) hydrodynamic chromatography.

given that the presence of convection gives rise to a Taylor contribution to that effective diffusivity (Taylor 1953), which formula, however, is strictly valid only for relatively long tubes, or, more precisely, for large aspect ratio channels.

A comprehensive study (Meyers & Liapis 1998) incorporating various effective transport models, both theoretical and semi-empirical, found the ensuing L-scale macrotransport parameters to be only weakly dependent upon the choice of transport model, but strongly dependent upon the connectivity of the network. In spite of this potentially weak dependence in certain circumstances, it nevertheless behooves us to formulate rational definitions for the effective channel transport parameters, especially in the asymptotic limit (cf. §5.3.1).

No differences exist in the specification of the mean velocity $U(j)$ and dispersivity $D(j)$ in the presence of chemical reactions. Rather, it proves necessary to further specify a mean solute depletion rate, k, quantifying the uniform rate of chemical reaction (or irreversible adsorption) occuring at different points within the network. The specification of the reaction rates on the network scale is considerably less equivocal than was the case for the transport rates, whereby their discussion is deferred to a later point in this thesis (see §4.2).

1.3 Intersection "Mixing" Rule

Numerous models also exist for quantifying the solute "mixing" processes occurring at the channel junctions. Unlike the mean intrachannel transport parameters, the mixing rule, serving to quantify the probability of the particle exiting the intersection through a specified channel among those available, is less equivocal, being governed by the physics of the device. Most widely used is the "perfect mixing" hypothesis (Adler & Brenner 1984b, Andrade *et al.* 1992, Aviles & Levan 1991, de Arcangelis *et al.* 1986, Koplik *et al.* 1988, McGreavy *et al.* 1990, Meyers & Liapis 1998, Sahimi & Jue 1989, Sorbie & Clifford 1991, Zhang & Seaton 1994), wherein no bias is assumed to exist regarding the choice

of intersectional egress channel, owing either to purely convective solute transport (a mixing-tank model) in the absence of molecular diffusion, or extremely vigorous molecular diffusion — in probabilistic terms, effectively a Markov process (Sahimi *et al.* 1983). At large Peclet numbers (convection dominated solute transport), the choice of intersection solute egress channel is typically assumed to be simply proportional to the flow rate prevailing within that channel (Imdakm & Sahimi 1991, Rege & Fogler 1988, Sahimi *et al.* 1983, Sorbie & Clifford 1991). At smaller Peclet numbers, where the transport process is diffusion dominated, Sorbie & Clifford (1991) invoked steric arguments to assert that the choice of intersection egress channel is proportional to that channel's cross-sectional area, while for very small intersections Bruderer & Bernabe (2001) assumed that no stream-wise molecular diffusion occurs.

Each of the preceding mixing rules represent approximations, albeit pragmatically useful ones, of the exact solute transport processes occurring at the channel intersections. A more precise determination of egress channel probabilities may be obtained from the exact solution of the prevailing continuous convective-diffusive transport problem, including proper accountings of the detailed fluid flow field and particle dynamics, e.g. hydrodynamic wall effects. The latter scheme has been employed elsewhere by Yan *et al.* (1991) for the analysis of blood hematocrit flow through microvasculature, as well as by Lee & Koplik (1999) for the Stokesian dynamics of fluid-particle-bed interactions in model porous media.

No doubt exists that a continuous description of the vertex transport processes, when compared with any of the proposed *ad hoc* probabilistic vertex mixing schemes, would furnish more physically accurate results within this discrete theory. However, given the computational resources required to more precisely quantify the detailed intersectional transport processes, it is only incrementally more difficult to solve the original, classical continuous Taylor-Aris dispersion problem (Brenner & Edwards 1993) itself! Consequently, practical applications of our discrete Taylor-Aris dispersion theory suggest choosing an appropriate vertex mixing rule in order to approximate the true physical

processes prevailing therein — rather than attempting to solve the exactly-formulated microscale problem posed at the channel intersections.

1.4 Homogenization Techniques

Having established a particular physical model for the unit-cell-level transport processes, a detailed picture of the global particle transport process is generated from such models typically by: (i) a Monte Carlo scenario (Bruderer & Bernabe 2001, Meyers & Liapis 1998, Sahimi 1992, Sahimi *et al.* 1983, Sorbie & Clifford 1991) whereby single particle (or "plume") transport through the network is statistically simulated numerous times; (ii) a Laplace transform technique (Andrade *et al.* 1992, de Arcangelis *et al.* 1986, Koplik *et al.* 1988, McGreavy *et al.* 1990, Sahimi 1992, Sahimi & Jue 1989) wherein a unidirectional, unsteady convection-diffusion equation is solved for the continuous solute concentration distribution prevailing in each discrete channel or pore within the entire network; or (iii) more involved schemes. The last category of methods is most prevalent in the analysis of (nonlinear) reactive networks, and includes computational techniques such as unidirectional capillary transport models (Alvarado *et al.* 1997, Andrade *et al.* 1997, Zhang & Seaton 1994), pore-effectiveness factors (Hollewand & Gladden 1992), or other algorithms for simulating particle transport (Rege & Fogler 1988). Alternatively, analytical techniques, such as effective-medium theories (Cukier 1983a,b, Kruger 1990a,b, Mattern & Felderhof 1987, Muthukumar 1982), multiple-scales analyses (Mauri 1991), volume-averaging (Ryan *et al.* 1980), center-manifold theory (Balakotaiah & Dommeti 1999), effective stream-tube ensembles (Ginn 2001), and general lumping analyses (Li & Rabitz 1991), have been invoked to homogenize the unsteady convection-diffusion-reaction transport equation governing the solute transport through the interstices of the periodic array. These latter techniques are well adapted to characterize disordered ("random") porous media or nonlinear chemical reaction rates (or both), along with the concomitant degree of mathematical and computational complexity accompanying such schemes. In-

deed, variations of these schemes have been employed to analyze transport in randomly connected reactive networks (Alvarado *et al.* 1997, Andrade *et al.* 1997, Aviles & Levan 1991, Hollewand & Gladden 1992, Leitzelement *et al.* 1984, Sahimi *et al.* 1990, Zhang & Seaton 1994), in particular near to the percolation limit (Andrade *et al.* 1997, Sahimi *et al.* 1990, Wakad & Nardse 1974, Zhang & Seaton 1994). Continuity of the concentrations at all channel intersections in the network, together with an (arbitrary) choice of initial solute injection point within the network as a whole, jointly with conditions at the (finite) boundaries (if any) of the network, provide sufficient conditions in such models for uniquely specifying the overall solute transport problem. The macroscale transport parameters are then calculated, either from moments of the simulation statistics or from the convective-diffusive solute concentration profile (cf. §2.3 and §4.4).

Proponents (de Arcangelis *et al.* 1986, Koplik *et al.* 1988, Sahimi 1992, Sahimi & Jue 1989) of the Laplace transform technique argue that their scheme constitutes an "exact" method for ascertaining these macrotransport parameters, having presumably solved for the complete unsteady microscale concentration field extant within each pore of the network following solute injection. As discussed in §1.2, some degree of arbitrariness invariably exists as to the applicability of Taylor-Aris l-scale dispersivity arguments for calculating the effective particle velocity and diffusivity prevailing over the length of a single channel, which parameters are strictly valid only in an L-scale asymptotic sense (Brenner & Edwards 1993, Koplik *et al.* 1988).[3] For asymptotically long times, our discrete Taylor-Aris dispersion theory, to be derived, represents a much more compact computational scheme for calculating the L-scale parameters $\bar{\mathbf{U}}^*$ and $\bar{\mathbf{D}}^*$ when compared with such Laplace transform techniques, since its use does not necessitate initially obtaining the exhaustively-detailed time-dependent solution of the underlying unsteady convection-diffusion equations for each pore of the network prerequisite to cal-

[3]Despite the ubiquitious use (Andrade *et al.* 1992, Koplik *et al.* 1988, McGreavy *et al.* 1990, Sahimi 1992, Sahimi & Jue 1989, Sorbie & Clifford 1991) of such parameters in graphical network models, the work of Koplik *et al.* (1988) represents the only contribution that we were able to identify commenting on the validity of employing individual l-scale Taylor-Aris parameters within the context of network models.

culating these parameters. Moreover, our scheme provides, *inter alia*, rigorous criteria governing use of the single channel, l-scale Taylor-Aris parameters entering into the subsequent L-scale calculation of $\bar{K}^*$, $\bar{\mathbf{U}}^*$ and $\bar{\mathbf{D}}^*$. Indeed, the ability to quantitatively obtain the macroscopic L-scale transport properties of a solute molecule traversing the medium, without the preliminary necessity for solving for the entire exact, time- and initial condition-dependent solute concentration field, constitutes the *raison d'être* underlying macrotransport theory (Brenner & Edwards 1993).

1.5 Outline of the Thesis

This thesis consists of two parts: (i) the theoretical development of a generalized Taylor-Aris paradigm for spatially periodic networks presented in Chapters 1-7; and (ii) the application of the paradigm to microfluidic separation devices and model porous media contained in Chapters 8-10. The first part continues in Chapter 2 with an overview of continuous macrotransport theory for spatially periodic media. This chapter is intended for readers who are unfamiliar with the latter theory, serving as a general reference for theoretical concepts which will be invoked in subsequent chapters. Experienced readers may skip immediately to Chapter 3, where we begin the new theoretical developments in this thesis with a discussion on the formal discretization of continuum descriptions of periodic media into graphical network models, including the proper adaptation of this discretization procedure for reactive networks. This discussion culminates in a set of three graphs and the specification of the relevant transport parameters governing solute transport processes on the graph. We continue in Chapter 4 with the derivation of detailed conservation equations (master equations) for non-reactive and reactive transport on the graphs constructed in Chapter 3. In Chapter 5, a generalized Taylor-Aris dispersion "method of moments" scheme is developed and applied to homogenize the non-reactive master equation derived in the preceding chapter. The homogenization procedure furnishes a pair of matrix equations for computing the node-based macrotransport "fields"

$P_0^\infty(i)$ and $\mathbf{B}(i)$, whose edge-based summations ultimately furnish the network-scale solute velocity vector $\bar{\mathbf{U}}^*$ and dispersivity dyadic $\bar{\mathbf{D}}^*$. It is demonstrated that significant model reductions are possible for a class of so-called "simple networks," the latter possessing immediate applicability to the case studies comprising much of the second part of this thesis. Chapter 6 presents a similar homogenization scheme for the reactive master equation. In contrast with the non-reactive transport theory of Chapter 5, the reactive network homogenization scheme furnishes a pair of adjoint matrix eigenvalue problems for computing the node-based macrotransport fields $P_0^\infty(i)$ and $A(i)$ (ultimately required to calculate the mean solute velocity $\bar{\mathbf{U}}^*$ by an edge-based summation), jointly with the network-scale, effective first-order irreversible reaction rate constant $\bar{K}^*$. The dispersion calculation for reactive networks is similar to their non-reactive counterparts, requiring the solution of a matrix equation for the node-based macrotransport field $\mathbf{B}(i)$, which is ultimately used to determine the Taylor-Aris solute dispersivity $\bar{\mathbf{D}}^*$ by an edge-base summation.

With a complete theory in hand, Part II of this thesis focuses upon its application to several model problems. We will show that the present theory agrees well with intuition, existing theoretical results and available experimental data (both qualitative and quantitative), thereby lending concrete weight to the abstract Taylor-Aris dispersion arguments invoked for the theoretical development. Chapter 8 considers a pair of straightforward examples, both of which demonstrate the computational simplicity of the network scheme over and above the existing continuous calculation scheme (Brenner & Edwards 1993). The first example, representing an application of the non-reactive theory, involves computing the mean velocity and dispersion of point-size solutes in microfluidic serpentine chromatography channels. We demonstrate that the results computed from the present theory compare favorably with those derived from both continuous generalized Taylor-Aris dispersion theory and porous media theory. The second example, representing an application of the reactive theory, considers a simple model of a reactive porous media. It is shown that the highly non-linear network-scale results computed from the present

theory accord well with intuition.

Whereas the examples discussed in Chapter 8 serve to illustrate the computational simplicity of the theory, the case studies considered in Chapters 9 and 10 correspond to recently developed microfluidic protocols for the separation of DNA. Importantly, the networks employed for these separation processes constitute "simple networks," whereby minimal mathematical manipulations are required to apply our discrete Taylor-Aris dispersion analysis. In Chapter 9, we consider the vector chromatography of finite sized particles, accounting for the reduced particle mobility from wall effects. A generic design equation is derived for computing the mean direction of a Brownian body as a function of the device geometry, applied force and the size of the particle. In Chapter 10, microfluidic entropic trapping devices are modeled, again invoking the simple network theory. The qualitative and quantitative theoretical results compare favorably with the available experimental data. We conclude in Chapter 11 with some closing remarks.

Chapter 2

Review of Macrotransport Theory

This chapter constitutes a self-contained review of generalized Taylor-Aris dispersion theory (macrotransport theory) for spatially periodic systems. Much of what follows is based upon Chapters 4 and 8 of the monograph by Brenner & Edwards (1993), with some supplemental information culled from a trio of foundational papers on the subject (Brenner 1980, Brenner & Adler 1982, Dungan *et al.* 1990) (These references will not be cited explicitly hereafter.) For those readers unfamiliar with macrotransport theory, this review aims to provide sufficient background for understanding the discrete macrotransport theory developed in this thesis; only those elements of classical macrotransport theory which pertain directly to the discrete theory will be presented here. Readers interested in an elementary overview of the statistical foundations of the theory are referred to Chapter 8 of the thesis by Ganesan (1999), as well as the review paper by Brenner (1991). Experienced readers may proceed directly to the new material beginning in Chapter 3.

The elements of macrotransport theory pertinent to this thesis entail the computation of a trio of averaged "macrotransport parameters" governing the asymptotic linear transport of Brownian solute particles in unbounded spatially periodic media: (i) the mean volumetric solute depletion rate, $\bar{K}^*$; (ii) the mean solute velocity vector, $\bar{\mathbf{U}}^*$; and (iii) the solute dispersivity dyadic, $\bar{\mathbf{D}}^*$. The conceptual framework for calculating

these macrotransport parameters is predicated upon the use of a conditional probability density function, which quantifies the likelihood of locating the (center of the) Brownian particle at the (continuous) position $\mathbf{R}$ at time t during its stochastic trajectory through the medium. Consequently, macrotransport analyses of this type are valid for both a single Brownian particle and a non-interacting collection of particles (which may be viewed as a continuum solute field). The solute (particle) conditional probability density field is governed by an unsteady, three-dimensional partial differential equation, which may be solved, at least in principle, subject to appropriate attenuation conditions at the external boundaries of the infinitely extended medium, as well as appropriate conditions at internal boundaries. With this exhaustively detailed solution in hand, it is possible to then calculate the macrotransport parameters from asymptotic moments of the conditional probability density. In contrast, macrotransport theory employs a rigorous method of moments scheme for computing these parameters *without first ascertaining the exact solution*, thereby representing a significant computational savings. Moreover, macrotransport theory furnishes a simple conceptual framework for interpreting asymptotic transport processes in heterogeneous media, especially when compared with extracting such information from the overwhelming amount of data embodied in the exact solution.

We proceed here with a brief introduction to geometrical descriptions of externally unbounded spatially periodic media, as well as the conditional probability density function which quantifies the likelihood of locating the Brownian particle at a given point in space during its convective-diffusive-reactive transport through such media. Assuming that the equation governing the probability density can be solved, at least in principle, Lagrangian interpretations are set forth for calculating the macrotransport parameters. An alternative "method-of-moments" calculation scheme is then developed for both non-reactive and reactive transport, culminating in a "macrotransport equation," which furnishes an Eulerian interpretation to the macrotransport parameters.

2.1 Geometrical Description

Attention is restricted here to infinitely-extended, spatially periodic media. By spatially periodic is meant that there exists a primitive parallelepipedal (or curvilinear, if necessary) unit-cell, which, when repeated indefinitely in all spatially dimensions, reproduces the entire unbounded medium. When the medium contains two phases (i.e. a model porous medium consisting of a stationary solid phase and flowing liquid phase), it is typically assumed that the fluid constitutes a continuous phase, where every point in the fluid is accessible from every other point therein, and that the solid comprises a discontinuous phase. By convention, the boundaries of the unit cell are assumed to lie entirely in the continuous phase, although the geometric (and computational) scheme may be altered to take advantage of computational savings which might accrue from placing the boundaries of the unit cell in both phases (Dorfman & Brenner 2001). The geometry of the unit cell is characterized by a trio of basic lattice vectors, $\mathbf{l}_1$, $\mathbf{l}_2$ and $\mathbf{l}_3$, whose magnitudes are subject to the restriction that their scalar triple product $|\mathbf{l}_1 \cdot \mathbf{l}_2 \times \mathbf{l}_3|$ is equal to the total superficial volume of the unit cell, τ_0. Translating the unit cell through any of these basic lattice vectors reproduces an adjacent cell. The choice of unit cell is not unique, since, for example, a new unit cell could be constructed which contains two (or more) of the original unit cells. Regardless of the particular choice of unit cell, translation of any one of the infinitely many possible unit cell choices through its respective base lattice vectors will furnish exactly the same unbounded medium as would be constructed from the translation of an alternate choice of unit cell through its base lattice vectors. Consequently, the ultimate results for $\bar{K}^*$, $\bar{\mathbf{U}}^*$ and $\bar{\mathbf{D}}^*$ (and any other macroscopic, averaged property) must prove to be independent of the arbitrary choice of unit cell.

The spatial location of cell $\mathbf{n}$ $[\mathbf{n} \equiv (n_1, n_2, n_3)\,,\ (-\infty < n_i < \infty)]$ is quantified by its discrete position vector, $\mathbf{R}_\mathbf{n}$, which is defined as pointing from an origin situated at a fixed point (the locator point) of cell $\mathbf{n} = (0, 0, 0)$ to the locator point of cell $\mathbf{n} = (n_1, n_2, n_3)$. The unit cell centroid is typically chosen as the locator point, although any arbitrary

point in the unit cell may be selected as the locator point.[1] Explicitly, the discrete position vector possesses the form

$$\mathbf{R_n} = n_1\mathbf{l}_1 + n_2\mathbf{l}_2 + n_3\mathbf{l}_3. \tag{2.1}$$

Averaged transport properties must prove to be independent of the arbitrary choices of both the locator point and the origin. The exact, continuous location vector of any point in the medium, $\mathbf{R}$, may be decomposed, using the discrete position vector, into a discrete|continuous sum,

$$\mathbf{R} = \mathbf{R_n} + \mathbf{r}, \tag{2.2}$$

where $\mathbf{r} \in \tau_0\{\mathbf{n}\}$ represents the "local" position vector, pointing from the locator point of cell $\mathbf{n}$ to a given point in the interior of cell $\mathbf{n}$.

By way of example, consider the model porous medium depicted in Fig. 2-1. The medium consists of a two-dimensional, rectangular array of stationary, deformed ellipsoidal bed particles, twelve of which are depicted in the figure. The shaded region denotes one possible choice of unit cell, where each cell contains a single particle in its upper left-hand corner. Clearly, many other unit cells could be chosen, say, with the centroid of the unit cell coincident with the centroid of the particle, or with the unit cell containing multiple particles. The unit cell is characterized by a pair of basic lattice vectors, $\mathbf{l}_x$ and $\mathbf{l}_y$, which correspond to the continuous x- and y-dimensions of the unit cell in a rectangular (x, y) Cartesian coordinate system. The superficial volume (area) of the unit cell is the scalar product of these lattice vectors, $\tau_0 = |\mathbf{l}_x \times \mathbf{l}_y| = l_x l_y$. The discrete (integer) location of the unit cell is given by the index notation $\mathbf{n} = (i, j)$, with the origin $\mathbf{n} = (0, 0)$ coincident the x-y location $(0, 0)$. The cell locator point is chosen to be the centroid of the unit cell, whereupon the local, intracellular position vector $\mathbf{r}$ points from the centroid of the cell to the continuous position $\mathbf{R} - \mathbf{R_n}$.

[1] By chosing the locator point in the *unit cell*, we have enforced the restriction that the locator points in adjacent cells be displaced by the same base lattice vector that quantifies the relative displacements of these adjacent cells; that is, the locator points are spatially periodic.

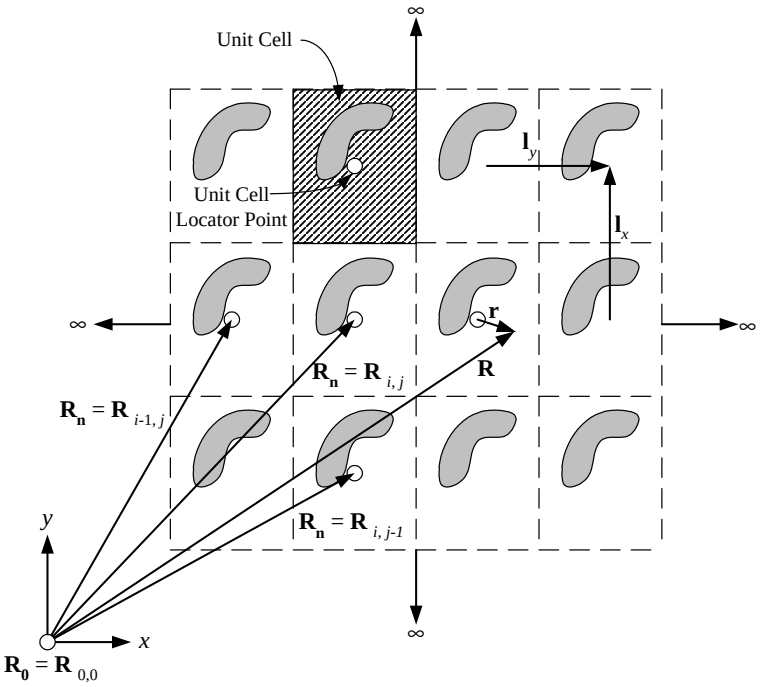

Figure 2-1: Schematic of an infinitely extended model spatially periodic porous medium. A representative unit cell is depicted by the shaded region, with twelve unit cells shown *en toto*. The cell is characterized geometrically by the basic lattice vectors $\mathbf{l}_x$ and $\mathbf{l}_y$, together with its discrete cell location (i, j) in the array. A quartet of discrete unit vectors $\mathbf{R_n}$ are depicted, each pointing from the origin to their respective cell locator points.

2.2 Conditional Probability Density

Consider the conditional probability density $P_r \equiv P_r\,(\mathbf{R},t\,|\,\mathbf{R}_0)$ of locating the (generally reactive) Brownian particle at the continuous position $\mathbf{R}$ at time t, given its introduction into the medium at the location $\mathbf{R}_0$ at time $t = 0$.[2] Using the discrete|continuous decomposition (2.2) of the position vector, the probability density possesses the alternate functional form $P_r(\mathbf{R_n}, \mathbf{r}, t\,|\,\mathbf{R}_{\mathbf{n}_0}, \mathbf{r}_0)$, with $\mathbf{R}_{\mathbf{n}_0} \equiv n_{1_0}\mathbf{l}_1 + n_{2_0}\mathbf{l}_2 + n_{3_0}\mathbf{l}_3$ the location of

[2]For the time being, we employ the notation $P_r\,(\mathbf{R},t\,|\,\mathbf{R}_0)$ for both reactive and non-reactive solute transport. In §2.4.2, we will introduce a change of variables $P_r \rightarrow P\,(\mathbf{R},t\,|\,\mathbf{R}_0)$, where $P\,(\mathbf{R},t\,|\,\mathbf{R}_0)$ is an effective non-reactive probability density. The latter transformation is trivial for purely convective-diffusive solute transport, for which reactions are absent, i.e. $P = P_r$.

the unit cell $\mathbf{n}_0$ in which the solute was introduced initially at the local position $\mathbf{r}_0$ at time $t = 0$. Inasmuch as the choice of origin is arbitrary, the conditional probability (and subsequent macrotransport results) can only depend upon the displacement vector from the origin, $\mathbf{R_n} - \mathbf{R_{n_0}}$, rather than being functionally dependent upon $\mathbf{R_n}$ and $\mathbf{R_{n_0}}$ separately. Consequently, without any loss of generality, we are free to set $\mathbf{R_{n_0}} = \mathbf{0}$, which is equivalent in its consequences to repositioning the arbitrarily placed origin at $\mathbf{0}$ to a new origin at $\mathbf{R_{n_0}}$.[3] With the latter choice, the conditional probability density adopts its canonical form

$$P_r \equiv P_r\left(\mathbf{R_n}, \mathbf{r}, t \,|\, \mathbf{r}_0\right). \tag{2.3}$$

The convective-diffusive-reactive transport of the conditional probability density at each point $\mathbf{R}$ in the medium is governed by the unsteady partial differential equation

$$\frac{\partial P_r}{\partial t} + \nabla \cdot \mathbf{J}_r + k(\mathbf{r}) P_r = \delta(\mathbf{R_n}) \delta\left(\mathbf{r} - \mathbf{r}_0\right) \delta(t), \tag{2.4}$$

with δ the Dirac delta function. The reactive probability flux density, $\mathbf{J}_r$, is assumed to possess the constitutive form

$$\mathbf{J}_r = \mathbf{U}(\mathbf{r}) P_r - \mathbf{D}(\mathbf{r}) \cdot \nabla P_r, \tag{2.5}$$

where $\mathbf{U}\left(\mathbf{r}\right)$ and $\mathbf{D}(\mathbf{r})$ are the (local) solute velocity vector and diffusivity dyadic, respectively. The solute velocity vector includes contributions to deterministic solute convection arising from "piggy-back" transport in an entraining fluid flow, as well as from the action of any externally applied forces. The parameter $k\left(\mathbf{r}\right)$ $(k \geq 0)$ quantifies a position-dependent, first-order, irreversible reaction rate occurring within the medium, with $k = 0$ corresponding to non-reactive transport. The parameters $\mathbf{U}(\mathbf{r})$, $\mathbf{D}(\mathbf{r})$ and

[3] In what follows, we choose to set $\mathbf{R}_0 = \mathbf{r}_0$, which corresponds to $\mathbf{R_{n_0}} = \mathbf{0}$. This leads to notational differences between the present review and the classical reference (Brenner & Edwards 1993). In the latter, the initial position $\mathbf{R_{n_0}}$ is retained throughout the derivation.

$k(\mathbf{r})$ are restricted to be spatially periodic functions,

$$\mathbf{U}(\mathbf{r}) = \mathbf{U}(\mathbf{r} + \mathbf{l}_k), \tag{2.6}$$

$$\mathbf{D}(\mathbf{r}) = \mathbf{D}(\mathbf{r} + \mathbf{l}_k), \tag{2.7}$$

$$k(\mathbf{r}) = k(\mathbf{r} + \mathbf{l}_k), \quad (k = 1, 2, 3). \tag{2.8}$$

Consequently, these microtransport parameters only depend upon the local position vector $\mathbf{r}$, rather than upon the global position vector $\mathbf{R}$. Whereas the geometric periodicity of the medium typically defines the overall spatial periodicity of the microtransport processes, in some circumstances it is the spatial periodicity of the microtransport parameters which serve to determine the overall spatial periodicity, such as is the case for transport in spatially periodic potential fields (Nitsche & Brenner 1988).

It is assumed that the probability density decays sufficiently fast with distance from the point of introduction into the system such as to be attenuated completely at infinity,

$$P_r \to 0 \quad \text{as} \quad |\mathbf{R} - \mathbf{R}_0| \to \infty. \tag{2.9}$$

So that subsequent integrals converge, it is necessary to require further that all moments of the probability density and flux density decay faster than algebraically,

$$|\mathbf{R} - \mathbf{R}_0|^m (P_r, \mathbf{J}_r) \to \mathbf{0} \quad \text{as} \quad |\mathbf{R} - \mathbf{R}_0| \to \infty, \quad (m = 0, 1, 2, \ldots). \tag{2.10}$$

Integrating eq. (2.4) over all space, namely $\mathbf{R}_\infty$, together with use of the attenuation condition (2.10), reveals that the conditional probability density P satisfies the following conservation conditions:

$$\int_{\mathbf{R}_\infty} P_r \, d^3\mathbf{R} = \begin{cases} 0, & t < 0, \\ 1, & t = 0, \\ \leq 1, & t > 0, \end{cases} \tag{2.11}$$

with the inequality $P_r \leq 1$ reducing to the equality $P_r = 1$ for purely convective-diffusive transport, where $k(\mathbf{r}) = 0$.

Whereas the aforementioned conditional probability density suffices to completely characterize the exactly-posed microtransport processes, it sometimes proves convenient to consider instead an intracellular conditional probability density.[4] With the decomposition of the physical space into discrete unit cells, the infinite integral (2.11) may be instead expressed in terms of the intracellular probability density,

$$\int_{\mathbf{R}_\infty} P_r \, d^3\mathbf{R} \equiv \sum_{\mathbf{n}} \int_{\tau_0\{\mathbf{n}\}} P_r \, d^3\mathbf{r}, \tag{2.12}$$

with

$$\sum_{\mathbf{n}} \equiv \sum_{n_1=-\infty}^{\infty} \sum_{n_2=-\infty}^{\infty} \sum_{n_3=-\infty}^{\infty} \tag{2.13}$$

and $\mathbf{R}_\infty = \sum_{\mathbf{n}} \tau_0\{\mathbf{n}\}$. Within a given unit cell, the governing equation (2.4) adopts the form

$$\frac{\partial P_r}{\partial t} + \nabla \cdot \mathbf{J}_r + k(\mathbf{r}) P_r = \delta_{\mathbf{n},\mathbf{n}_0} \delta(\mathbf{r} - \mathbf{r}_0)\delta(t), \tag{2.14}$$

with $\delta_{\mathbf{n},\mathbf{n}_0} = \delta_{\mathbf{n},\mathbf{0}}$ a Kronecker delta function. The intracellular conditional probability density must satisfy continuity of probability density and flux density across the faces of the unit cells, which requires that P_r and ∇P_r satisfy the relations[5]

$$P_r(\mathbf{R}_\mathbf{n} - \mathbf{l}_k, \mathbf{r} + \mathbf{l}_k) = P_r(\mathbf{R}_n, \mathbf{r}), \tag{2.15}$$

$$\nabla P_r(\mathbf{R}_\mathbf{n} - \mathbf{l}_k, \mathbf{r} + \mathbf{l}_k) = \nabla P_r(\mathbf{R}_n, \mathbf{r}) \quad (k = 1, 2, 3)\,. \tag{2.16}$$

In general, the complete specification of the microscale transport problem also requires

[4]The notation $P_r\,(\mathbf{R}_\mathbf{n}, \mathbf{r}, t \,|\, \mathbf{r}_0)$ is employed for both the original conditional probability density, which is defined throughout all space, as well as the intracellular probability density. Aside from *conceptual* differences, both probability density fields satisfy essentially identical governing equations, boundary conditions and continuity conditions. It will be clear from context whether we are referring to the original or the intracellular probability density function.

[5]The non-intracellular conditional probability density also obeys the continuity relationships (2.15)-(2.16) across the faces of the unit cell.

stating boundary conditions at the intracellular phase interfaces, if any. Such conditions typically involve continuity of flux density (or no penetration), partitioning of P_r across the interface, an so forth. However, these boundary conditions exist on a length scale which is smaller than that which will be resolved by the discrete network model. Consequently, further discussion of these boundary conditions will be suppressed. The reader is referred to the monograph of Brenner & Edwards (1993) for the details on intracellular boundary conditions and their impact upon the method of moments macrotransport scheme.

2.3 Lagrangian Definitions of the Macrotransport Parameters

In principle, given sufficient computational resources, the governing equation (2.4) may be solved exactly, subject to the attenuation condition (2.9). In the present section, we outline a procedure for computing the macrotransport parameters $\bar{K}^*$, $\bar{\mathbf{U}}^*$ and $\bar{\mathbf{D}}^*$ from this exact solution, based upon their Lagrangian definitions. Subsequently, we use this information to show how these parameters may be calculated without knowledge of this hypothetical exact solution.

In the presence of depletion reactions, the total probability density of the system diminishes towards zero from its initial value for times $t > 0$. Consequently, it proves convenient in what follows to define the survival probability density of the Brownian particle,

$$\mathbf{M}_{0r}\left(t \,|\, \mathbf{r}_0\right) \stackrel{\text{def.}}{=} \sum_{\mathbf{n}} \int_{\tau_0\{\mathbf{n}\}} P_r\left(\mathbf{R}_{\mathbf{n}}, \mathbf{r}, t \,|\, \mathbf{r}_0\right)\, d^3\mathbf{r}, \tag{2.17}$$

which corresponds to the total amount of solute present in the system at time t. Clearly, in the absence of chemical reactions, $M_{0r} = 1$ for all times $t \geq 0$. Moreover, the conser-

vation condition (2.11) now adopts the simplified form,

$$\frac{1}{\mathbf{M}_{0r}\left(t \,|\, \mathbf{r}_0\right)} \int_{\mathbf{R}_\infty} P_r\left(\mathbf{R_n}, \mathbf{r}, t \,|\, \mathbf{r}_0\right) d^3\mathbf{R} = \begin{cases} 0, & t < 0, \\ 1, & t \geq 0. \end{cases} \tag{2.18}$$

When chemical reactions are present within the medium, it is expected (and can be shown) that the total conditional probability density will decay exponentially in time, at least at long-times. The mean reaction rate, $\bar{K}^*$, is chosen so as to quantify the exponential decay of the survival probability density,

$$\bar{K}^* \stackrel{\text{def.}}{=} -\lim_{t\to\infty} \frac{d}{dt} \ln\left(M_{0r}\right). \tag{2.19}$$

In the absence of chemical reactions, $M_{0r} = 1$, consistent with the intuitive result $\bar{K}^* = 0$ for this case.

The mean velocity vector, $\bar{\mathbf{U}}^*$, which quantifies the asymptotic, linear growth of the mean displacement, $\overline{\Delta\mathbf{R}}$, of the Brownian particle in time, is computed by evaluating the asymptotic limit,

$$\bar{\mathbf{U}}^* \stackrel{\text{def.}}{=} \lim_{t\to\infty} \frac{d}{dt} \overline{\Delta\mathbf{R}}, \tag{2.20}$$

where the overbar ($\overline{\Delta\mathbf{R}}$) indicates an ensemble-average over the solute probability density [cf. eq. (2.24)]. Explicitly, the long-time condition $t \to \infty$ requires that the time t be long compared with the diffusion time scale for solute movement across a unit cell,

$$t \gg \frac{l^2}{|\mathbf{D}|}, \tag{2.21}$$

where l is a characteristic linear dimension of the unit cell, i.e. $l = \max\left(|\mathbf{l}_k|\right)$, and $|\mathbf{D}|$ is some suitable norm of the diffusivity dyadic. An additional long-time requirement [cf. eq. (2.74)] must also be satisfied for the case of reactive transport.

The dispersivity dyadic, $\bar{\mathbf{D}}^*$, which quantifies the linear growth of the mean-squared deviation about the mean position, $\overline{\left(\Delta\mathbf{R} - \overline{\Delta\mathbf{R}}\right)^2}$, is computed from the Einstein-like

relationship

$$\bar{\mathbf{D}}^{*} \overset{\text{def.}}{=} \frac{1}{2} \lim_{t\to\infty} \frac{d}{dt} \overline{\left(\Delta\mathbf{R} - \overline{\Delta\mathbf{R}}\right)^{2}}. \tag{2.22}$$

The preceding definitions for computing $\bar{\mathbf{U}}^{*}$ and $\bar{\mathbf{D}}^{*}$ are Lagrangian in nature, and reflect only the contribution of the solute probability density which is still present in the medium at time t. So that depleted solute probability density does not contribute to $\bar{\mathbf{U}}^{*}$ and $\bar{\mathbf{D}}^{*}$, it is necessary to define the ensemble average, $\bar{\zeta}$, of any tensor-valued property ζ as

$$\bar{\zeta} \overset{\text{def.}}{=} \frac{1}{M_{0r}} \int_{\mathbf{R}_{\infty}} \zeta P_{r}\left(\mathbf{R}_{\mathbf{n}}, \mathbf{r}, t \,|\, \mathbf{r}_{0}\right)\, d^{3}\mathbf{R}, \tag{2.23}$$

which may alternatively be expressed in terms of the intracellular probability density,

$$\bar{\zeta} \overset{\text{def.}}{=} \frac{1}{M_{0r}} \sum_{\mathbf{n}} \int_{\tau_{0}\{\mathbf{n}\}} \zeta P_{r}\left(\mathbf{R}_{\mathbf{n}}, \mathbf{r}, t \,|\, \mathbf{r}_{0}\right)\, d^{3}\mathbf{r}. \tag{2.24}$$

Although, for reactive transport, $P_{r} \to 0$ as $t \to \infty$, the ratio (2.24) formed with M_{0r} tends to a finite limit as $t \to \infty$.

Upon using the ensemble average definition (2.24), the mean displacement of the particle's position, $\mathbf{R}$, from its initial position, $\mathbf{R_0}$, adopts the functional form

$$\overline{\Delta\mathbf{R}} = \frac{1}{M_{0r}} \sum_{\mathbf{n}} \int_{\tau_{0}\{\mathbf{n}\}} \left(\mathbf{R} - \mathbf{R_0}\right) P_{r}\left(\mathbf{R}_{\mathbf{n}}, \mathbf{r}, t \,|\, \mathbf{r}_{0}\right)\, d^{3}\mathbf{r}. \tag{2.25}$$

However, computation of the *macroscopic* transport properties $\bar{\mathbf{U}}^{*}$ and $\bar{\mathbf{D}}^{*}$ does not necessitate considering the particle position on a *microscopic* scale as fine as $\mathbf{R}$. Rather, it suffices to consider coarse-grained (unit-cell scale) macrotransport parameters defined on a macroscopic (Darcy) scale, the latter scale possessing a coarseness equivalent to the discrete position vector, $\mathbf{R}_{\mathbf{n}}$. Consequently, the average position (2.25) may be computed, based upon a coarse-scale (unit-cell) location, with the initial coarse-grained position $\mathbf{R_0} = \mathbf{0}$,

$$\overline{\Delta\mathbf{R}} = \frac{1}{M_{0r}} \sum_{\mathbf{n}} \mathbf{R}_{\mathbf{n}} \int_{\tau_{0}\{\mathbf{n}\}} P_{r}\left(\mathbf{R}_{\mathbf{n}}, \mathbf{r}, t \,|\, \mathbf{r}_{0}\right)\, d^{3}\mathbf{r}. \tag{2.26}$$

For sufficiently long times (and unbounded media), it is expected that differences between the average positions computed from eqs. (2.25) and (2.26) will be exponentially small. Again adopting a coarse-grained approach, the mean-squared displacement adopts the form

$$\overline{\left(\Delta\mathbf{R}-\overline{\Delta\mathbf{R}}\right)^2} = \frac{1}{M_{0r}}\sum_{\mathbf{n}}\left(\mathbf{R}_{\mathbf{n}}-\bar{\mathbf{R}}\right)^2\int_{\tau_0\{\mathbf{n}\}} P_r\left(\mathbf{R}_{\mathbf{n}},\mathbf{r},t\,|\,\mathbf{r}_0\right)\,d^3\mathbf{r}, \tag{2.27}$$

which, with use of eqs. (2.18) and (2.26), may be restated as the symmetric difference,

$$\overline{\left(\Delta\mathbf{R}-\overline{\Delta\mathbf{R}}\right)^2} = \frac{1}{M_{0r}}\sum_{\mathbf{n}}\mathbf{R}_{\mathbf{n}}\mathbf{R}_{\mathbf{n}}\int_{\tau_0\{\mathbf{n}\}} P_r\left(\mathbf{R}_{\mathbf{n}},\mathbf{r},t\,|\,\mathbf{r}_0\right)\,d^3\mathbf{r} - \overline{\boldsymbol{\Delta}\mathbf{R}}\,\overline{\boldsymbol{\Delta}\mathbf{R}}. \tag{2.28}$$

Upon introducing the m^{th}-order moments of the probability density

$$\mathbf{M}_{mr}\left(t\,|\,\mathbf{r}_0\right) \stackrel{\text{def.}}{=} \sum_{\mathbf{n}}\mathbf{R}_{\mathbf{n}}^m\int_{\tau_0\{\mathbf{n}\}} P_r\left(\mathbf{R}_{\mathbf{n}},\mathbf{r},t\,|\,\mathbf{r}_0\right)\,d^3\mathbf{r} \quad (m=0,1,2,\ldots), \tag{2.29}$$

in which $\mathbf{R}_{\mathbf{n}}^m \equiv \mathbf{R}_{\mathbf{n}}\mathbf{R}_{\mathbf{n}}\cdots\mathbf{R}_{\mathbf{n}}$ (m-times), the canonical forms of $\bar{\mathbf{U}}^*$ and $\bar{\mathbf{D}}^*$ adopt the respective forms

$$\bar{\mathbf{U}}^* = \lim_{t\to\infty}\frac{d}{dt}\left(\frac{\mathbf{M}_{1r}}{M_{0r}}\right), \tag{2.30}$$

$$\bar{\mathbf{D}}^* = \frac{1}{2}\lim_{t\to\infty}\left[\frac{\mathbf{M}_{2r}}{M_{0r}} - \frac{\mathbf{M}_{1r}\mathbf{M}_{1r}}{M_{0r}^2}\right]. \tag{2.31}$$

With knowledge of the exhaustively detailed, pointwise conditional probability density $P_r\left(\mathbf{R}_{\mathbf{n}},\mathbf{r},t\,|\,\mathbf{r}_0\right)$, the macrotransport parameters $\bar{K}^*$, $\bar{\mathbf{U}}^*$ and $\bar{\mathbf{D}}^*$ may be calculated from eqs. (2.19), (2.29), (2.30) and (2.31) for a given choice of $\mathbf{r}_0$. The computational resources requisite for effecting such a calculation are overwhelming, and only furnish, at least in principle, values of the macrotransport parameters corresponding to a particular intracell location, $\mathbf{r}_0$.[6] In contrast, macrotransport theory furnishes a rigorous

[6]Subsequent analysis will show that the macrotransport parameters are in fact independent of $\mathbf{r}_0$ in the long-time limit, although a fictitious initial condition (dependent upon $\mathbf{r}_0$) must be employed in the reactive case. Without the *conceptual* framework of macrotransport theory, however, there exists no rational methodology for ascertaining the independence from $\mathbf{r}_0$ or the fictitious initial condition from

physico-mathematical scheme for making such a calculation for any value of $\mathbf{r}_0$, without first requiring knowledge of the exact solution.

2.4 Method of Moments

Details of macrotransport theory for non-reactive and reactive microtransport processes are outlined in the present section. To summarize, computation of the various moments $\mathbf{M}_{mr}$ from eq. (2.29) requires performing unit-cell quadratures of the intracellular probability densities, P_r, over the unit cell volumes $\tau_0\{\mathbf{n}\}$, followed by a weighted infinite summation over $\mathbf{n}$. The elegance of macrotransport theory lies in reversing the order of these operations: by first forming the moments of the governing equation, one arrives at so-called "local moments," which are governed by differential equations and boundary conditions which only depend upon the local position vector $\mathbf{r}$. Upon constructing asymptotic solutions to these local moment equations and summing over $\mathbf{n}$, the asymptotic properties of the total moments (2.29) are ascertained without ever computing the exact solution P_r.

2.4.1 Non-Reactive Transport

Moment Scheme

We begin here with an overview of the calculation scheme for non-reactive transport, wherein $k(\mathbf{r}) = 0$. Define the m^{th}-local moment of the conditional probability density as the m-adic,

$$\mathbf{P}_m\left(\mathbf{r}, t \,|\, \mathbf{r}_0\right) \stackrel{\text{def.}}{=} \sum_{\mathbf{n}} \left(\mathbf{R}_{\mathbf{n}}\right)^m P_r\left(\mathbf{R}_{\mathbf{n}}, \mathbf{r}, t \,|\, \mathbf{r}_0\right). \tag{2.32}$$

---

the exactly posed microtransport problem.

Multiplying the governing equation (2.4) by $\mathbf{R}_{\mathbf{n}}^{m}$, with $k(\mathbf{r})$ =0, and summing over $\mathbf{n}$ furnishes the local moment equation

$$\frac{\partial \mathbf{P_m}}{\partial t} + \nabla \cdot \mathbf{J}_m = \delta_{m,0}\delta\left(\mathbf{r}-\mathbf{r}_0\right)\delta\left(t\right), \tag{2.33}$$

where $\delta_{m,0}$ is a Kronecker delta function, and $\mathbf{J}_m$ is the moment flux density,

$$\mathbf{J}_m = \mathbf{U}\mathbf{P}_m - \mathbf{D}\cdot\nabla\mathbf{P}_m. \tag{2.34}$$

Multiplying the boundary conditions (2.15)-(2.16) by $\mathbf{R}_{\mathbf{n}}^{m}$ $(m = 0, 1, 2)$, followed by some algebraic manipulations, furnishes the following "jump" conditions of the unit cell faces:[7]

$$\|P_0\| = 0, \qquad \|\nabla P_0\| = \mathbf{0}, \tag{2.35}$$

$$\|\mathbf{P}_1\| = -\|\mathbf{r}P_0\|, \qquad \|\nabla\mathbf{P}_1\| = -\|\nabla\left(\mathbf{r}P_0\right)\|, \tag{2.36}$$

$$\|\mathbf{P}_2\| = -\|\mathbf{P}_1\mathbf{P}_1/P_0\|, \qquad \|\nabla\mathbf{P}_2\| = -\|\nabla\left(\mathbf{P}_1\mathbf{P}_1/P_0\right)\|, \tag{2.37}$$

where the "jump" operator, for an arbitrary tensor valued function ζ, possesses the functional form

$$\|\zeta\| \stackrel{\text{def.}}{=} \zeta(\mathbf{r}+\mathbf{l}_k) - \zeta\left(\mathbf{r}\right) \quad (k = 1, 2, 3). \tag{2.38}$$

To complete the moment scheme, define the m^{th}-total moment of the conditional probability density as the m-adic,

$$\mathbf{M}_m\left(t \,|\, \mathbf{r}_0\right) \stackrel{\text{def.}}{=} \int_{\tau_0} \mathbf{P}_m\left(\mathbf{r}, t \,|\, \mathbf{r}_0\right) d^3\mathbf{r}. \tag{2.39}$$

Integrating eq. (2.33) over the unit cell volume and applying the divergence theorem

[7]The gradient operator commutes with the jump operator whenever the boundaries of the unit cell lie wholly within the continuous phase (Iosilevskii & Brenner 1995), such as would be the case in Fig. 2-1. For some circumstances, however, it proves computationally convenient to situate the boundaries of the unit cell at the interface between the continuous and discontinuous phases (Dorfman & Brenner 2001), whereupon the boundary conditions and jump conditions must be altered appropriately.

furnishes the following ordinary differential equation governing the $\mathbf{M}_m$:

$$\frac{d\mathbf{M}_m}{dt} = -\oint_{\partial\tau_0} d\mathbf{s}\cdot\mathbf{J}_m + \delta_{m,0}\delta(t)\,. \tag{2.40}$$

Consequently, determination of the macrotransport parameters requires constructing asymptotic solutions for the lower order $\mathbf{P}_m$ from eq. (2.33), computing the flux density $\mathbf{J}_m$ from eq. (2.34), and then solving for the growth of the total moments from eq. (2.40). The moments $\mathbf{M}_m$ (2.39) are indistinguishable from the moments $\mathbf{M}_{mr}$ (2.29), since for the non-reactive case the survival probability density $M_{0r} = 1$.

Asymptotic Moments

Setting $m = 0$ in eq. (2.33) reveals that the asymptotic probability density possesses the form

$$P_0(\mathbf{r}, t\,|\,\mathbf{r}_0) \approx P_0^\infty(\mathbf{r}) + \exp, \tag{2.41}$$

where $P_0^\infty(\mathbf{r})$ is an unconditional probability density (being independent of the initial position $\mathbf{r}_0$), and "exp" denotes terms which are exponentially small in time. This asymptotic solution obeys the steady state conservation equation,

$$\nabla\cdot\mathbf{J}_0^\infty = 0, \tag{2.42}$$

with $\mathbf{J}_0^\infty$ the unconditional flux density,

$$\mathbf{J}_0^\infty = \mathbf{U}P_0^\infty - \mathbf{D}\cdot\nabla P_0^\infty. \tag{2.43}$$

Substitution of the asymptotic solution (2.41) into the boundary conditions (2.35) reveals that P_0^∞ satisfies the jump conditions

$$\|P_0^\infty\| = 0 \quad \text{and} \quad \|\nabla P_0^\infty\| = \mathbf{0}. \tag{2.44}$$

Since the delta function input no longer appears in the asymptotic equation set, it is necessary to impose the normalization condition,

$$\int_{\tau_0} P_0^{\infty} d^3\mathbf{r} = 1. \tag{2.45}$$

With use of the asymptotic solution (2.41) and the moment flux density (2.34), comparison of the first-total moment (2.40) with eq. (2.30) furnishes the asymptotic result

$$\frac{d\mathbf{M}_1}{dt} \approx \bar{\mathbf{U}}^* + \text{exp}, \tag{2.46}$$

with the mean velocity vector to be computed from the unit-cell quadrature,

$$\bar{\mathbf{U}}^* = \int_{\tau_0} \mathbf{J}_0^{\infty} d^3\mathbf{r}. \tag{2.47}$$

In conjunction with the definition of the total moments (2.39), the solution (2.46) suggests (subject to *a posteriori* verification) a trial solution for the first local moment of the form

$$\mathbf{P}_1 \approx P_0^{\infty}(\mathbf{r}) \left[\bar{\mathbf{U}}^* t + \mathbf{B}(\mathbf{r})\right] + \text{exp}, \tag{2.48}$$

where $\mathbf{B}(\mathbf{r})$ is a time-independent field to be determined. Integrating $\mathbf{P}_1$ over the unit cell domain, using the normalization condition (2.45), furnishes the first total moment,

$$\mathbf{M}_1 \approx \bar{\mathbf{U}}^* t + \bar{\mathbf{B}} + \text{exp}, \tag{2.49}$$

wherein

$$\bar{\mathbf{B}} = \int_{\tau_0} P_0^{\infty} \mathbf{B}\, d^3\mathbf{r}. \tag{2.50}$$

Substitution of (2.48) into the boundary conditions (2.36) furnishes the following boundary conditions imposed upon $\mathbf{B}$:

$$\|\mathbf{B}\| = -\|\mathbf{r}\| \quad \text{and} \quad \|\nabla\mathbf{B}\| = \mathbf{0}. \tag{2.51}$$

Form the governing equation for the first local moment from eq. (2.33) by setting $m = 1$, and substitute into the resulting expression the trial solution (2.48). This eventually furnishes the differential equation governing the **B**-field,

$$\nabla \cdot (P_0^\infty \mathbf{D} \cdot \nabla \mathbf{B}) - \mathbf{J}_0^\infty \cdot \nabla \mathbf{B} = P_0^\infty \bar{\mathbf{U}}^*. \tag{2.52}$$

The latter differential equation is exact, and specifies the **B**-field only to within an arbitrary, additive vector constant, whose value proves irrelevant in the eventual computation of the dispersivity dyadic. Moreover, the derivation of a solvable, time-independent differential equation and boundary conditions for **B** constitutes *a posteriori* verification of the trial solution (2.48).

Substitution of the trial solution (2.48) into the total moment equation (2.40) (with $m = 2$), followed by significant manipulations, ultimately furnishes the following differential equation governing $\mathbf{M}_2$:

$$\frac{d\mathbf{M}_2}{dt} \approx 2\bar{\mathbf{U}}^*\bar{\mathbf{U}}^* t + \oint_{\tau_0} d\mathbf{s} \cdot [P_0^\infty \mathbf{D} \cdot \nabla (\mathbf{B}\mathbf{B}) - \mathbf{J}_0^\infty \mathbf{B}\mathbf{B}] + \exp. \tag{2.53}$$

Introduction of eqs. (2.49) and (2.53) into eq. (2.31) furnishes the following unit-cell quadrature for computing the solute dispersivity dyadic:

$$\bar{\mathbf{D}}^* = \int_{\tau_0} P_0^\infty (\nabla \mathbf{B})^\dagger \cdot \mathrm{sym}\,(\mathbf{D}) \cdot \nabla \mathbf{B}\, d^3\mathbf{r}, \tag{2.54}$$

where $\dagger$ is the transpose operator and, for any dyadic ζ, the symmetry operator is defined as

$$\mathrm{sym}\,(\zeta) \stackrel{\text{def.}}{=} \frac{1}{2}\left(\zeta + \zeta^\dagger\right). \tag{2.55}$$

2.4.2 Reactive Transport

Moment Scheme

The essential difference between the preceding "non-reactive" moment scheme and the present "reactive" moment scheme arises from non-conservation of the reactive solute probability density for times $t > 0$, owing to solute depletion reactions. This leads to a "non-conservation" statement for P_r,

$$\sum_{\mathbf{n}} \int_{\tau_0\{\mathbf{n}\}} P_r d^3\mathbf{r} < 1 \quad \text{for} \quad t > 0. \tag{2.56}$$

In order to invoke a moment scheme analogous to that employed in the previous subsection for conserved (non-reactive) transport, define the "non-reactive" conditional probability density,

$$P\left(\mathbf{R_n}, \mathbf{r}, t \,|\, \mathbf{r}_0\right) \overset{\text{def.}}{=} \frac{\exp\left(\bar{K}t\right)}{A\left(\mathbf{r}_0\right)} P_r\left(\mathbf{R_n}, \mathbf{r}, t \,|\, \mathbf{r}_0\right), \tag{2.57}$$

with the constant $\bar{K}$ and the fictitious initial condition $A(\mathbf{r}_0)$ to be specified later. Substituting the change of variables (2.57) into the governing equation (2.4) for P_r furnishes the following differential equation governing the field P:

$$\frac{\partial P}{\partial t} + \nabla \cdot \mathbf{J} = \left[\bar{K} - k\left(\mathbf{r}\right)\right] P + \frac{1}{A\left(\mathbf{r}_0\right)} \delta(\mathbf{R_n}) \delta\left(\mathbf{r} - \mathbf{r}_0\right) \delta(t), \tag{2.58}$$

with $\mathbf{J}$ the non-reactive flux density,

$$\mathbf{J} = \frac{\exp\left(\bar{K}t\right)}{A\left(\mathbf{r}_0\right)} \mathbf{J}_r. \tag{2.59}$$

The attenuation conditions (2.10) and unit cell boundary conditions (2.35)-(2.37) are unaltered by this change of variables.

Define the m^{th}-local moment and the (unweighted) total moment,

$$\mathbf{P}_m\left(\mathbf{r}, t \,|\, \mathbf{r}_0\right) \stackrel{\text{def.}}{=} \sum_{\mathbf{n}} \left(\mathbf{R}_{\mathbf{n}}\right)^m P\left(\mathbf{R}_{\mathbf{n}}, \mathbf{r}, t \,|\, \mathbf{r}_0\right), \tag{2.60}$$

$$\mathbf{M}'_m\left(t \,|\, \mathbf{r}_0\right) \stackrel{\text{def.}}{=} \int_{\tau_0} \mathbf{P}_m\left(\mathbf{r}, t \,|\, \mathbf{r}_0\right) d^3\mathbf{r}. \tag{2.61}$$

In addition, define the m^{th}-weighted total moment,

$$\mathbf{M}_m\left(t \,|\, \mathbf{r}_0\right) \stackrel{\text{def.}}{=} \int_{\tau_0} A\left(\mathbf{r}\right) \mathbf{P}_m\left(\mathbf{r}, t \,|\, \mathbf{r}_0\right) d^3\mathbf{r}. \tag{2.62}$$

The unweighted total moments are intrinsically related to the reactive total moments (2.29),

$$\mathbf{M}_{mr}\left(t \,|\, \mathbf{r}_0\right) = A\left(\mathbf{r}_0\right) \exp\left(-\bar{K}t\right) \mathbf{M}'_m\left(t \,|\, \mathbf{r}_0\right). \tag{2.63}$$

The latter definitions permit the following solution scheme: (i) determine the parameter $\bar{K}$ and the field $A\left(\mathbf{r}\right)$ so that M_0 is conserved for all times; (ii) compute the asymptotic properties of the weighted total moments, $\mathbf{M}_m$, by a scheme analogous to that employed for non-reactive transport; (iii) show that the weighted total moments, $\mathbf{M}_m$, differ from their unweighted counterparts, $\mathbf{M}'_m$, by exponentially small terms at long times; and (iv) compute the macrotransport parameters from the reactive moments $\mathbf{M}_{mr}$. In the interest of brevity, the manipulations required to prove (iii) are suppressed here, since such calculations are performed in detail for the discrete theory in Chapter 6.

The differential equation governing the local moments $\mathbf{P}_m$ may be derived in a manner similar to its non-reactive counterpart, ultimately furnishing the expression

$$\frac{\partial \mathbf{P}_m}{\partial t} + \nabla \cdot \mathbf{J}_m - \left[\bar{K} - k\right] \mathbf{P}_m = \frac{1}{A\left(\mathbf{r}_0\right)} \delta_{m,0} \delta\left(\mathbf{r} - \mathbf{r}_0\right) \delta(t), \tag{2.64}$$

with the flux density moments defined by eq. (2.34). To derive the equation governing

M_0, set $m = 0$ in eq. (2.64), multiply by $A(\mathbf{r})$, and integrate by parts over τ_0 to obtain[8]

$$\frac{dM_0}{dt} = \int_{\tau_0} P_0 \left[\mathbf{U} \cdot \nabla A + \nabla \cdot \left(\mathbf{D}^\dagger \cdot \nabla A \right) + \left(\bar{K} - k \right) A \right] d^3\mathbf{r} - \oint_{\partial\tau_0} d\mathbf{s} \cdot \left(\mathbf{J}_0 A - P_0 \mathbf{D}^\dagger \cdot \nabla A \right) + \delta(t). \tag{2.65}$$

In order for M_0 to be conserved for all times $t \geq 0$, the field $A(\mathbf{r})$ is to be chosen as the solution of the eigenvalue problem,

$$\mathbf{U} \cdot \nabla A + \nabla \cdot \left(\mathbf{D}^\dagger \cdot \nabla A \right) + \left(\bar{K} - k \right) A = 0, \tag{2.66}$$

subject to the boundary conditions[9]

$$\| A \| = 0 \quad \text{and} \quad \| \nabla A \| = \mathbf{0}. \tag{2.67}$$

Proper normalization of the A-field, as well as the physically relevant eigenvalue, $\bar{K}_0$, and eigensolution, A_0, will be specified later. Integration of eq. (2.65), with eq. (2.66), reveals that the zeroth-weighted moment is indeed conserved for all times $t \geq 0$,

$$M_0 = \begin{cases} 0, & t < 0, \\ 1, & t \geq 0. \end{cases} \tag{2.68}$$

Multiplying eq. (2.64) by $A(\mathbf{r})$ and integrating over τ_0, together with use of (2.66), furnishes the following differential equation governing the total weighted moments:

$$\frac{d\mathbf{M}_m}{dt} = \oint_{\partial\tau_0} d\mathbf{s} \cdot \left[A \mathbf{J}_m + \mathbf{D}^\dagger \cdot (\nabla A) \, \mathbf{P}_m \right] + \delta_{m,0} \delta(t). \tag{2.69}$$

[8] There are several typographical errors in Chapter 8 of the monograph by Brenner & Edwards (1993), including the following equation. The foundational paper of Dungan *et al.* (1990) should be considered the definitive reference for reactive macrotransport processes in spatially periodic media.

[9] The jump conditions (2.67) enforce a spatial periodicity of A and ∇A, whereupon the contribution of the surface integral appearing in eq. (2.65) to M_0 vanishes in light of the fact that $\mathbf{J}_0$, P_0 and $\mathbf{D}$ are themselves spatially periodic functions.

Asymptotic Moments

As was the case for non-reactive transport, the zeroth local moment of non-reactive probability density asymptotically approaches the unconditional value $P_0^\infty(\mathbf{r})$,

$$P_0(\mathbf{r}, t \,|\, \mathbf{r}_0) \approx P_0^\infty(\mathbf{r}) + \exp. \tag{2.70}$$

Substituting this solution into eq. (2.64) furnishes the following eigenvalue problem for P_0^∞:

$$\nabla \cdot \mathbf{J}_0^\infty - \left(\bar{K} - k\right) P_0^\infty = 0, \tag{2.71}$$

with the flux density given by (2.43) and the jump conditions specified by eq. (2.44). The eigenvalue problems (2.66) and (2.71) serve only to define the P_0^∞ and A fields to within arbitrary, constant multipliers. To fix these multipliers, we enforce the normalization conditions,

$$\int_{\tau_0} P_0^\infty d^3\mathbf{r} = 1, \tag{2.72}$$

$$\int_{\tau_0} A P_0^\infty d^3\mathbf{r} = 1. \tag{2.73}$$

Denote the smallest eigenvalue of eq. (2.71) by $\bar{K}_0$ and the second smallest eigenvalue by $\bar{K}_1$. The long-time asymptotic description of the transport processes requires satisfying the long-time restriction,

$$t \gg \frac{1}{\bar{K}_0} - \frac{1}{\bar{K}_1}, \tag{2.74}$$

which must be satisfied in conjunction with eq. (2.21). In this limit, the smallest eigenvalue, $\bar{K}_0$, corresponds to the slowest decaying mode of the exact solution, whereupon we identify $\bar{K}_0$ as being the reaction rate appearing in eq. (2.19), $\bar{K}_0 = \bar{K}^*$. Moreover, the physically relevant unconditional probability density field P_0^∞ is the eigensolution corresponding to $\bar{K} = \bar{K}^*$. Equations (2.66) and (2.71) are adjoint, whence $\bar{K}^*$ is recognized

as the physically relevant eigenvalue of (2.66), $\bar{K}_0 = \bar{K}^*$, and the physically relevant field A_0 is the eigensolution A corresponding to $\bar{K}_0 = \bar{K}^*$.

From this point onward, the reactive moment scheme follows a procedure identical to its non-reactive counterpart. Equation (2.46) may again be derived for the first weighted total moment $\mathbf{M}_1$, wherein

$$\bar{\mathbf{U}}^* = \int_{\tau_0} A J_0^\infty + P_0^\infty \mathbf{D}^\dagger \cdot \nabla A \, d^3\mathbf{r}. \tag{2.75}$$

Upon assuming a trial solution of the form of eq. (2.48), a first moment $\mathbf{M}_1$ equivalent to (2.49) is recovered, wherein

$$\bar{\mathbf{B}} = \int_{\tau_0} A P_0^\infty \mathbf{B} d^3\mathbf{r}. \tag{2.76}$$

Substitution of the trial solution into eq. (2.64) furnishes the same differential equation (2.52) and boundary conditions (2.51). With the trial solution confirmed, eq. (2.69) furnishes the second moment,

$$\frac{1}{2}\frac{d\mathbf{M}_2}{dt} \approx \bar{\mathbf{U}}^*\bar{\mathbf{U}}^* t + \mathrm{sym}\left(\bar{\mathbf{U}}^*\bar{\mathbf{B}}\right) + \int_{\tau_0} A P_0^\infty \left(\nabla \mathbf{B}\right)^\dagger \cdot \mathrm{sym}\left(\mathbf{D}\right) \cdot \nabla \mathbf{B} \, d^3\mathbf{r}. \tag{2.77}$$

Use of the definition (2.31) ultimately yields the following expression for the dispersivity dyadic:

$$\bar{\mathbf{D}}^* = \int_{\tau_0} A P_0^\infty \left(\nabla \mathbf{B}\right)^\dagger \cdot \mathrm{sym}\left(\mathbf{D}\right) \cdot \nabla \mathbf{B} \, d^3\mathbf{r}. \tag{2.78}$$

2.5 The Macrotransport Equation

In addition to their Lagrangian interpretations, the macrotransport parameters possess Eulerian interpretations as coefficients appearing in an averaged "macrotransport equation" governing the long-time solute transport processes. To this extent, define a coarse-grained discrete conditional probability density, based upon the non-reactive probability

density,

$$\bar{P}\left(\mathbf{R}_{\mathbf{n}}, t \,|\, \mathbf{r}_0\right) \stackrel{\text{def.}}{=} \frac{1}{\tau_0} \int_{\tau_0} A\left(\mathbf{r}\right) P\left(\mathbf{R}_{\mathbf{n}}, \mathbf{r}, t \,|\, \mathbf{r}_0\right) d^3\mathbf{r}, \tag{2.79}$$

whose total moments adopt the form

$$\mathbf{M}_m\left(t \,|\, \mathbf{r}_0\right) \stackrel{\text{def.}}{=} \tau_0 \sum_{\mathbf{n}} \left(\mathbf{R}_{\mathbf{n}}\right)^m \bar{P}\left(\mathbf{R}_{\mathbf{n}}, t \,|\, \mathbf{r}_0\right). \tag{2.80}$$

For sufficiently long-times, the latter total moments become independent of $\mathbf{r}_0$, whereupon our prior asymptotic analyses furnish the values of these first few moments, M_0, $\mathbf{M}_1$ and $\mathbf{M}_2$. Alternatively, one can define a coarse-grained continuous probability density,

$$\bar{P} \equiv \bar{P}\left(\bar{\mathbf{R}}, t\right), \tag{2.81}$$

where $\bar{\mathbf{R}}$ represents a continuous coarse-grained position vector defined on the scale of $\mathbf{R}_{\mathbf{n}}$. The moments of the latter probability density are given by the quadrature[10]

$$\mathbf{M}_m\left(t\right) = \int_{\mathbf{R}_\infty} \bar{\mathbf{R}}^m \bar{P}\left(\bar{\mathbf{R}}, t\right) d^3\bar{\mathbf{R}}. \tag{2.82}$$

The coarse-grained probability density $\bar{P}$ is thereby governed by the (non-reactive) macrotransport equation,

$$\frac{\partial \bar{P}}{\partial t} + \bar{\mathbf{U}}^* \cdot \nabla \bar{P} - \bar{\mathbf{D}}^* : \nabla\nabla \bar{P} = \delta(\bar{\mathbf{R}}) \delta\left(t\right). \tag{2.83}$$

For non-reactive transport, the latter equation is valid without alteration since the probability densities P_r and P are indistinguishable. For reactive transport, the change of variables (2.57) is invoked to derive the reactive macrotransport equation,

$$\frac{\partial \bar{P}_r}{\partial t} + \bar{\mathbf{U}}^* \cdot \nabla \bar{P}_r - \bar{\mathbf{D}}^* : \nabla\nabla \bar{P}_r + \bar{K}^* \bar{P}_r = A\left(\mathbf{r}_0\right) \delta(\bar{\mathbf{R}}) \delta\left(t\right). \tag{2.84}$$

[10] It would appear that one would need to retain the initial condition $\mathbf{R}_0 = \mathbf{r}_0$ when computing the total moments, i.e. $\bar{\mathbf{R}}^m$ should be replaced by $\left(\bar{\mathbf{R}} - \mathbf{R}_0\right)^m$, in order to reflect the dependence of the total moments upon the initial local position $\mathbf{r}_0$, in spite of the fact that $\mathbf{R}_{\mathbf{n}_0} = \mathbf{0}$. However, the position $\mathbf{r}_0$ cannot be resolved on the scale of the coarse-grained position vector $\bar{\mathbf{R}}$, whereupon $\mathbf{M}_m\left(t \,|\, \mathbf{r}_0\right) \approx \mathbf{M}_m(t)$.

The interpretation of the fictitious initial condition $A(\mathbf{r}_0)$ now becomes apparent as furnishing a correction to the true initial condition $\delta(\bar{\mathbf{R}})\delta(t)$ in order to reflect short-time transients which arise from the initial placement of the particle, and which persist for long-times.

Chapter 3

Graphical Modeling

3.1 Geometrical Description

The devices encompassed by our analysis consist of strongly connected, spatially periodic networks of intersecting channels embedded within a three-dimensional space, as depicted in Figs. 3-1 and 3-2 for a non-reactive and reactive medium, respectively.[1] By "strongly connected" is meant that each fluid point in the medium is accessible to a solute molecule from every other point in the medium. Transport through networks that are not strongly connected may be characterized within the framework of the present scheme by considering the individual Taylor-Aris dispersion processes occurring within each of the separately strongly connected networks which, together, collectively comprise the composite medium (Adler & Brenner 1984b) as a whole. The spatial periodicity of the network is reflected in the existence of a primitive (parallelepipedal or, if need be, curvilinear) unit cell repeated indefinitely in all directions. The use of infinitely-extended networks eliminates the need to explicitly account for "end effects." As real networks are finite in extent, the present analysis is strictly asymptotically valid only for circumstances where the number, N, of unit cells comprising the real system is large, i.e.

[1] While the microfluidic devices of interest constitute two-dimensional networks, the theory developed herein is valid for a network of *any* dimensionality. Three dimensions are chosen strictly for the sake of definiteness.

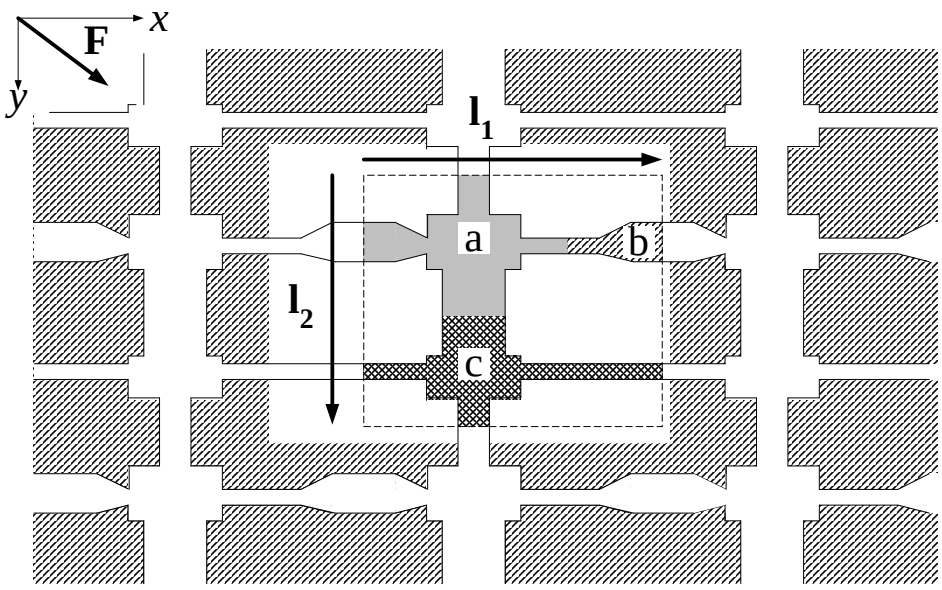

Figure 3-1: Schematic of a spatially periodic medium, with solute particle animation effected by the application of an externally-applied vector force, **F**. The repetitive unit cell is enclosed in the dashed box, with the subsequent discretization of the continuous unit cell regions indicated by the trio of shaded regions labeled a, b, and c. Lattice vectors $\mathbf{l_1}$ and $\mathbf{l_2}$ are indicated.

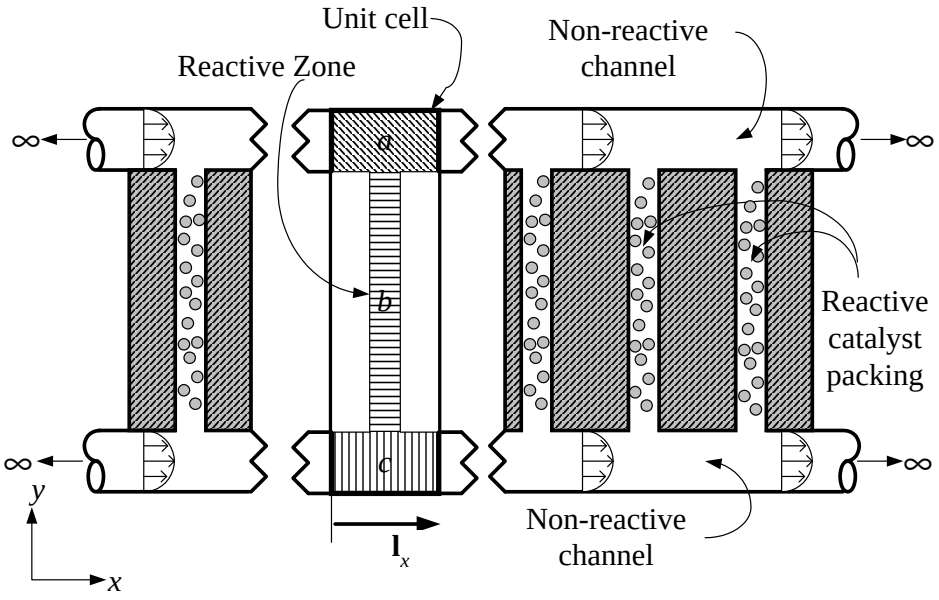

Figure 3-2: Spatially periodic, unidirectional reactive network consisting of two continuous, infinitely-extended, non-reactive cylindrical ducts, periodically connected by thin, cylindrical tubes containing a reactive catalyst packing. The periodicity of the network is reflected by the presence of the unit cell, indicated by the highlighted box, with base lattice vector $\mathbf{l_x}$. The white portion of the unit cell indicates the inacessible volume occupied by the blocks separating adjacent reactive domains. The unit cell is subdivided into the three discrete volumetric domains, a, b and c, so as to facilitate subsequent graphical analysis of the network.

$N \gg 1$. The entire composite medium may be imagined as constructed by translating this primitive unit cell (together with its contents) parallel to itself through a trio of basic lattice vectors $(\mathbf{l}_1, \mathbf{l}_2, \mathbf{l}_3)$ satisfying the requirement that their scalar triple product, $|\mathbf{l}_1 \cdot \mathbf{l}_2 \times \mathbf{l}_3|$, is equal to the superficial volume, τ_0, of the cell (Adler & Brenner 1984a).

The position of a given cell, say, the $\mathbf{I}^{\text{th}}$ cell, within the three-dimensional space can be identified by specifying the discrete L-scale position vector, $\mathbf{R_I}$, of, say, the centroid of the cell relative to an origin, $\mathbf{R_{I_0}} = \mathbf{0}$, at the centroid of the zeroth cell:

$$\mathbf{R_I} = I_1\mathbf{l}_1 + I_2\mathbf{l}_2 + I_3\mathbf{l}_3, \tag{3.1}$$

with (I_1, I_2, I_3) a triplet of positive or negative integers, including zero. The location of the $\mathbf{I}^{\text{th}}$ cell can also be identified by this triplet of integers $\mathbf{I} \equiv (I_1, I_2, I_3)$, itself regarded as a vector $\mathbf{I}$. The exact continuous $l \oplus L$-scale position vector $\mathbf{R}$, specifying the location of a point within the three-dimensional space, may be represented by the mixed discrete|continuous vector pair $(\mathbf{R_I}, \mathbf{r}) \equiv \mathbf{R}$, where the l-scale continuous vector $\mathbf{r}$ is the local position vector of a point within any unit cell with respect to that particular cell's centroid. This corresponds to the standard decomposition employed in classical generalized Taylor dispersion theory for spatially periodic media (Brenner 1980, Brenner & Edwards 1993), in the sense that the subsequently defined $l \oplus L$-scale continuous fields (velocity field, solute concentration field, etc.) are regarded as being exactly defined at each and every fluid point $\mathbf{R}$ of the $\mathbf{R} \equiv (\mathbf{R_I}, \mathbf{r})$-space encompassing the entire interstitial fluid region (at each instant in time). This detailed description quantifies the exact, or "continuous," case, in contrast with the subsequent graph-theoretical network treatment (the "discrete" case), where fields will be defined only at the discrete points in the subsequently defined $l \oplus L$-scale discrete $\mathcal{I} \equiv (\mathbf{I},i)$-space, where $i = (1, 2, \ldots n)$ identifies one of the n channel intersectional subvolume elements within a unit cell.

3.2 The Basic Graph

Significant computational advantages accrue to converting the classical (Brenner 1980, Brenner & Edwards 1993) continuous **R**-space decomposition of the spatially periodic medium into a discrete $\mathcal{I}$-space graphical representation. The internal configuration of each cell consists of a finite number of intersecting channels, some of which are wholly contained within the unit cell (such as the channel connecting a to b in the x-direction of Fig. 3-1), others being intersected by the unit cell boundaries (such as the channel connecting b to a in the x-direction of Fig. 3-1). The finite basic graph (Adler & Brenner 1984a), Γ_b, is then constructed from the coordination of the channels and their intersections, with the m_b channels in the unit cell comprising the edge set, $j \in E\Gamma_b$, whereas the n_b intersections of the latter edges comprise the vertex set, $i \in V\Gamma_b$. By virtue of the periodicity of the network, there exists within the unit cell two equivalent (homologous) channels intersected by the unit cell boundary, say, one edge with initial vertex at i in cell $\mathbf{I}$ with terminal vertex at i' in cell $\mathbf{I}'$, and a second edge with initial vertex at i in cell $\mathbf{I}''$ and terminal vertex at i' in cell $\mathbf{I}$. By convention, we retain only those edges which are directed *into* the unit cell (with the direction specified forthwith), assigning them the "macroscopic" jump vector[2]

$$\mathbf{R}(j) \stackrel{\text{def.}}{=} \mathbf{R}_{\mathbf{I}} - \mathbf{R}_{\mathbf{I}'}. \tag{3.2}$$

The edge set is characterized completely by each edge's respective orientation and geometry. The orientation of the edge set, which provides an unambiguous definition of the incidence matrix [cf. eq. (3.7)], as well as classifying the basic graph as a directed graph (Bollobas 1979), is chosen such that the scalar convective transport coefficient $c(j)$ is non-negative [cf. eq. (4.7)].[3] The latter criterion is satisfied by considering the mean

[2]The notation $\mathbf{I}'$ is invoked to generically denote a cell adjacent to $\mathbf{I}$. For networks with multiple adjacent cells, possessing a number of edges entering cell $\mathbf{I}$, the respective cells would be referred to notationally as $\mathbf{I}'$, $\mathbf{I}''$, etc.

[3]Since the macrotransport parameters $\bar{K}^*$, $\bar{\mathbf{U}}^*$ and $\bar{\mathbf{D}}^*$ are invariant to choice of coordinate system

l-scale convective velocity $\langle \mathbf{U}^C \rangle_j$ in edge j imparted to the particle by the entraining fluid flow in the channel, together with the mean l-scale particle velocity $\langle \mathbf{U}^F \rangle_j = \langle \mathbf{M} \rangle_j \cdot \mathbf{F}$ imparted by the action of an externally-applied force $\mathbf{F}$ acting on the particle in edge j. Here, $\langle \mathbf{M} \rangle_j$ denotes the mean l-scale solute mobility dyadic in channel j. As in classical macrotransport theory (Brenner & Edwards 1993), the mean l-scale particle velocity, $\langle \mathbf{U} \rangle_j = \langle \mathbf{U}^C \rangle_j + \langle \mathbf{U}^F \rangle_j$, within the edge must be unidirectional, either proceeding spatially from the region represented by vertex i to i', or vice versa. Consequently, the edge is directed such that the edge unit vector $\mathbf{e}(j)$, defined so as to point from the initial to the terminal vertex, is colinear with the mean velocity vector $\langle \mathbf{U} \rangle_j$ in that edge.

While many problems of interest involve channels of uniform cross-sectional configuration, the generic formulation presented herein is not similarly restricted. Regardless of channel tortuosity, it is possible to unequivocally define both a channel volume, $v_e(j)$, and channel length, $l(j)$, the latter being equal to the distance between the adjacent intersections corresponding to the initial and terminal vertices of edge j. For subsequent calculations requiring a flux per unit area, we define the effective cross-sectional area $A(j)$ of a channel as the ratio of its volume to length:

$$A(j) \overset{\text{def.}}{=} \frac{v_e(j)}{l(j)}. \tag{3.3}$$

So as to render explicit the preceding discretization scheme, Fig. 3-3 depicts the basic graph derived from the continuous medium depicted in Fig. 3-1, with homologous vertices (i.e. identical vertices present on the basic graph in an adjacent unit cell) denoted by affixing a prime, e.g. a and a'. Similarily, Fig. 3-4 is the basic graph corresponding to the reactive medium in Fig. 3-2. In the latter, we employ the alternate notation $(\mathbf{I}, i)$ to denote the nodes of the graph, as opposed to the single node affix-notation in Fig. 3-3.

The spatially periodic structure of the composite medium is reflected in the global

---

or abstract representation of the physical medium (Brenner & Edwards 1993), *any* edge orientation will suffice. However, the microscale convection-diffusion equations [cf. eqs. (4.6) and (4.10)] are valid only for $c(j) \geq 0$, a convention which does not arise in the continuous theory (Brenner & Edwards 1993).

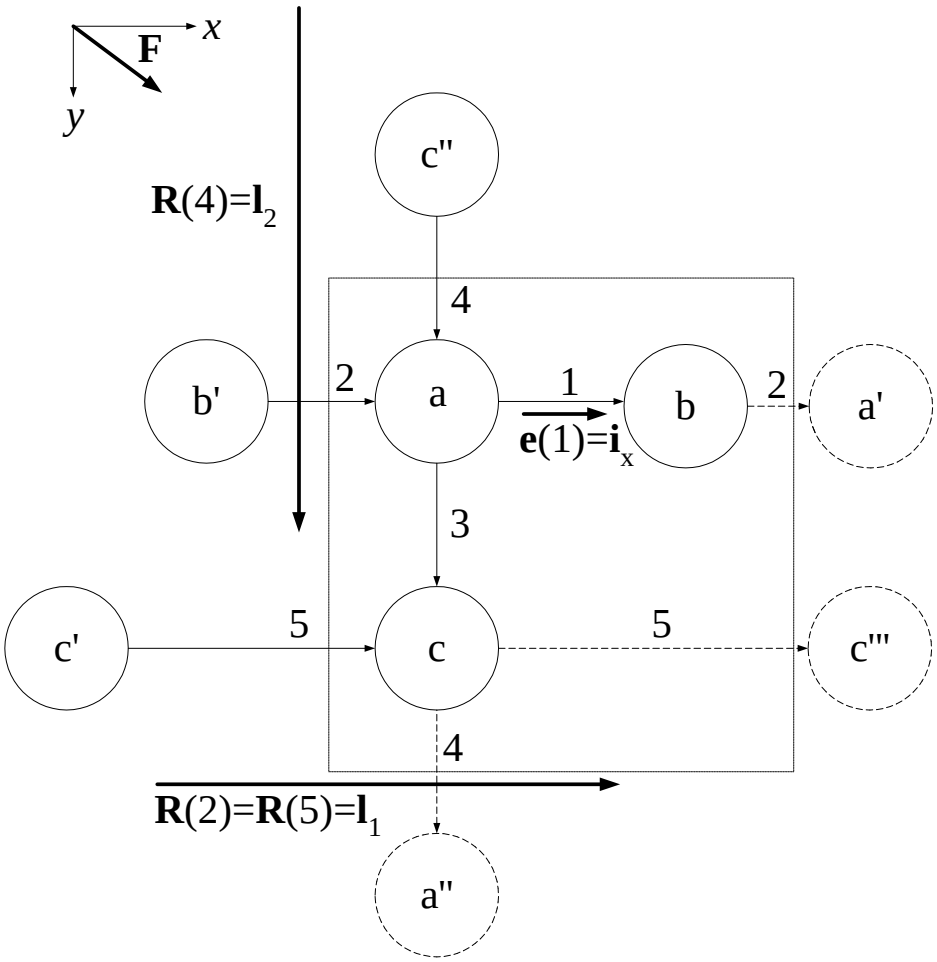

Figure 3-3: Basic graph for the spatially periodic medium of Fig. 3-1, with the unit cell enclosed within the box. The five different types of channels appearing in Fig. 3-1 are indicated by edge numbers 1 to 5. Homologous vertices existing outside the unit cell are denoted with a prime affix. Edges exiting the unit cell (and their associated homologous vertices), not otherwise included in the basic graph, are indicated by the dashed lines. A representative edge orientation vector, $\mathbf{e}(1)$, as well as the macroscopic jump vectors, are depicted. Macroscopic jump vectors for edges wholly contained within the unit cell are zero, i.e. $\mathbf{R}(1) = \mathbf{R}(3) = \mathbf{0}$.

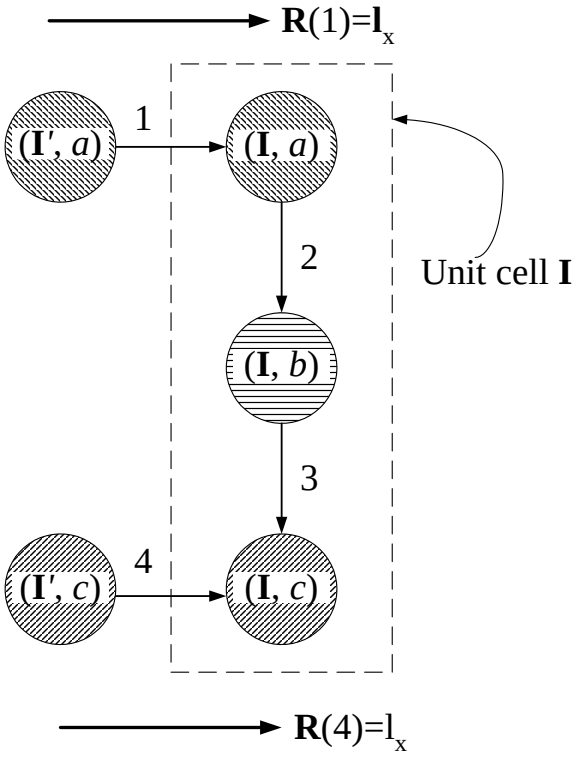

Figure 3-4: Basic graph constructed from the continuous description of Fig. 3-2. Vertices $i = \{a, b, c\}$ on the basic graph correspond to the volume elements depicted in Fig. 3-2. The edges $j = \{1, 2, 3, 4\}$ connecting adjacent vertices represent intrachannel transport pathways situated between the individual volume elements i, within each edge, in which the solute is transported at the convective rate $c(j)$ and diffusive rate $d(j)$. The macroscopic jump vector $\mathbf{R}(j = \{1, 4\}) = \mathbf{l_x}$ corresponds to a "Darcy-scale" displacement vector drawn between the adjacent cells $\mathbf{I}'$ and $\mathbf{I}$. Homologous vertices whose edges exit the unit cell, which would correspond to $(\mathbf{I}'', a)$ and $(\mathbf{I}'', b)$, are omitted here.

graph (Adler & Brenner 1984a), Γ_g, which is defined by basic vertices $\{v_i = 1 \leq i \leq n_b\}$ together with the transformation

$$\mathcal{L} = \{\Lambda + v_i;\, 1 \leq i \leq n_b\}\,, \tag{3.4}$$

where Λ is the simple lattice corresponding to the base vectors $(\mathbf{l}_1, \mathbf{l}_2, \mathbf{l}_3)$ and $\mathcal{L}$ is the derived lattice. Analogous to the continuous $l \oplus L$-scale $\mathbf{R}$-space description (3.1), the discrete $l \oplus L$-scale $\mathcal{I}$-space global graph Γ_g is formed by translation through the simple lattice.

3.3 The Local Graph

Although the union of the basic graph Γ_b and the transformation of eq. (3.4) constitutes a complete geometrical discretization of the continuous spatially periodic network, use of the basic graph proves cumbersome in applications, owing to superfluous information implicitly embedded in the homologous vertices. Combining homologous vertices and contracting the additional edges between them furnishes the local graph (Adler & Brenner 1984a), Γ_l, which will be utilized for all subsequent asymptotic calculations.

Upon contraction, the local graph contains $n \leq n_b$ vertices and $m \leq m_b$ directed edges. Edges connecting homologous vertices, say, i and i', result in a loop, rendering the local graph non-simple. In exchange for this non-simplicity, the local graph is independent of the particular configuration invoked for the basic unit cell (Adler & Brenner 1984a), as well as requiring minimal computational effort in the subsequent dispersion calculation.[4] For each of the n vertices i on the local graph, assign to the set $j \in \Omega^+(i)$ the subset of those edges j with terminal vertex i, and to the set of edges $j \in \Omega^-(i)$ the subset of those edges j with initial vertex i. From the basic graph of Fig. 3-3, the latter

[4]Further reductions in computational effort may be effected by specifying certain equation-specific rules for excluding loops from some of the ensuing summations. We eschew such reductions in what follows since they result in overly burdensome notation, obscuring thereby the inherent simplicity of the scheme itself.

homologous contraction process furnishes the local graph of Fig. 3-5, where, for example, $\Omega^+(c) = \{j = 3, 5\}$ and $\Omega^-(c) = \{j = 4, 5\}$, with the loop obviously a member of both sets. Likewise, Fig. 3-6 is the local graph for the reactive basic graph in Fig. 3-4.

The unit cell volume is subdivided in a discrete manner on the local graph to its vertices so as to facilitate exposition of the subsequent "exactly"-posed description of the solute transport process [cf. eq. (4.6)].[5] For the case where no chemical reactions are present, the volume, $v(i)$, of a vertex on the local graph is then defined as being equal to the volume, $v_i(i)$, of its channel intersection plus half the volume of all channels incident to that intersection:

$$v(i) \stackrel{\text{def.}}{=} v_i(i) + \frac{1}{2} \sum_{j \in \Omega^+(i)} v_e(j) + \frac{1}{2} \sum_{j \in \Omega^-(i)} v_e(j). \tag{3.5}$$

This definition is relaxed in the reactive case, since we will require there that the reaction rate, $k(i)$, be uniform within a given subvolume element. Regardless of the choice of discretization of the unit cell volume, the total volume of the vertices in the unit cell must be equal to the total superficial unit cell volume,

$$\sum_{i \in \Gamma_l} v(i) = \tau_0. \tag{3.6}$$

In addition to assigning the physical volume to a given vertex, we assign the particle's local continuous position $\mathbf{r}$ to the discrete location of vertex i situated, say, at the centroid of the subvolume element $v(i)$, whenever the particle resides within the subvolume $v(i)$. Consequently, the continuous $\mathbf{R}$-space particle location vector pair $(\mathbf{R_I}, \mathbf{r})$

[5] Assigning the volume to the vertices, despite the fact that a large portion of the unit cell's interstitial fluid volume may reside within the channels (edges) of the networks of real devices (Chou *et al.* 1999), lies counter to the rationale for assigning the volume to the vertices in a previous network model of this type by Adler & Brenner (1984b). There, it was assumed that the capillary tubes comprising the network linkages were thin, hence occupying little volume, whereas their intersections occupied large mixing volumes. Although not the case in present circumstances, the assignation of volume during the course of graphically coarse-graining the network geometry is at its very nature *ad hoc*. Therefore, the present scheme does not suffer rationally by prohibiting (by convention) the edges from possessing any volume.

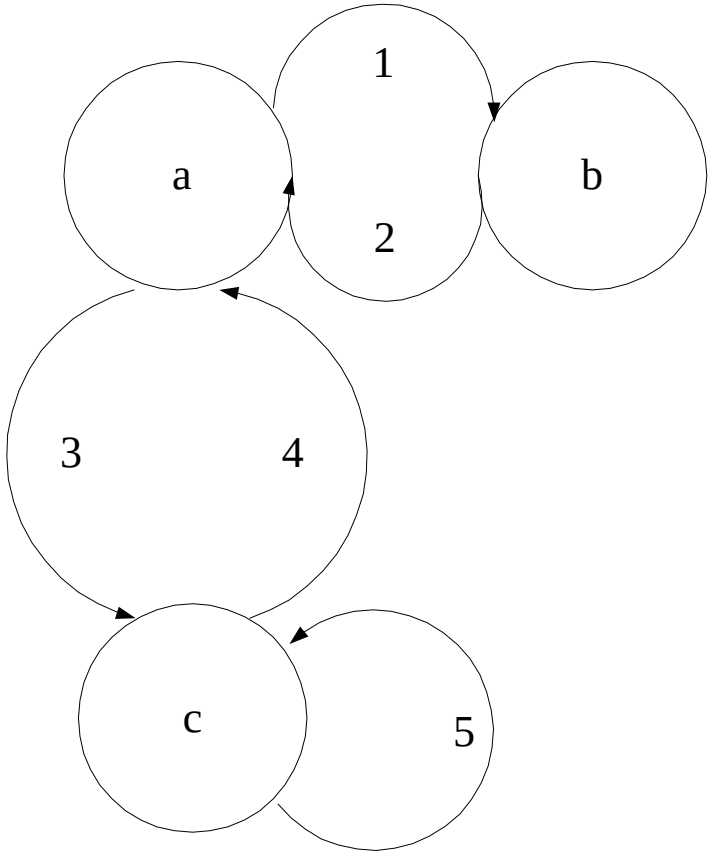

Figure 3-5: Local graph constructed from the basic graph of Fig. 3-3 by combining all homologous vertices and contracting the edges between them. The connectivity between c-type vertices results in a loop in the local graph, rendering it non-simple. The local (x, y) coordinate system is no longer necessary, having been embedded in the macroscopic jump vectors $\mathbf{R}(j)$ and the orientations of the edges.

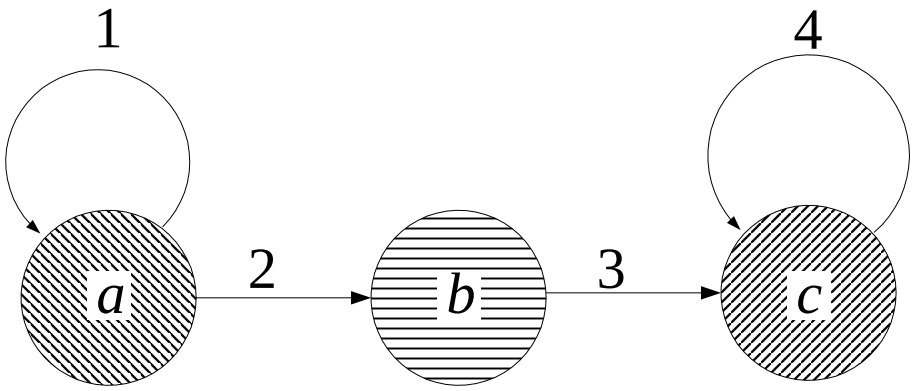

Figure 3-6: Local graph constructed by contracting homologous vertices in the basic graph of Fig. 3-4.

finds its discrete, coarse-grained $\mathcal{I}$-space counterpart in the discrete pair $(\mathbf{I}, i)$, the latter corresponding to the particle being in the subvolume element represented by node i in the unit cell located at discrete position $\mathbf{I}$.

3.4 Pertinent Elements of Graph Theory

In graph-theoretical terms (Bollobas 1979) the local graph is a finite directed graph, composed of the m member edge set $j \in E\Gamma_l$ and the n member vertex set $i \in V\Gamma_l$, thereby permitting the introduction of the $n \times m$ incidence matrix D_{ij}:[6]

$$D_{ij} \stackrel{\text{def.}}{=} \begin{cases} 1 \text{ if vertex } i \text{ is the terminal vertex of edge } j, \\ -1 \text{ if vertex } i \text{ is the initial vertex of edge } j, \\ 0 \text{ otherwise.} \end{cases} \tag{3.7}$$

The rank of the incidence matrix is $n-1$, owing to the connectivity of the graph. It will also prove convenient to decompose the incidence matrix into its positive and negative

[6]The incidence matrix here is opposite in sign from its traditional graph-theoretical definition (Bollobas 1979).

components,

$$D_{ij} = \Pi_{ij}^{(+)} - \Pi_{ij}^{(-)}, \tag{3.8}$$

where the nonzero entries in $\Pi_{ij}^{(+)}$ are the positive elements of D_{ij}, and the nonzero entries in $\Pi_{ij}^{(-)}$ are the absolute values of the negative elements of D_{ij}.

In what follows, matrix equations for the non-reactive, node-based macrotransport "fields" will be formulated in the cocycle space. Briefly, the cocycle space is constructed by partitioning the vertex space into two connected subgraphs: $V\Gamma = V_1\Gamma \cup V_2\Gamma$. A cocycle H consists of those edges (cuts) with one vertex in subgraph V_1 and a second vertex in subgraph V_2. The vector $\xi_H(e_j)$ associated with cocycle H may be defined as being positive for, say, edges terminating in V_1 (Berge 1973):

$$\xi_H(e_j) \stackrel{\text{def.}}{=} \begin{cases} 1 \text{ if } e_j \in H \text{ and its terminal vertex is in } V_1, \\ -1 \text{ if } e_j \in H \text{ and its initial vertex is in } V_1, \\ 0 \text{ otherwise.} \end{cases} \tag{3.9}$$

The $n-1$ cocycles forming the basis of the cocycle space may then be collected into the $m \times (n-1)$ cocycle matrix $\mathbf{K}$. An alternative, more convenient method for constructing $\mathbf{K}$ involves removing the row of the incidence matrix $\mathbf{D}$ that corresponds to the vertex not appearing as a cut set in the fundamental basis of the cocycle space, and then transposing the result. The latter technique, which preserves the structure of the incidence matrix, will be employed in what follows. The cocycle matrix, being of rank $n-1$, furnishes an alternative, formal method to that of the incidence matrix for incorporating the graph connectivity.

Chapter 4

Microscale Transport Phenomena

The present chapter furnishes the conservation equations governing the phenomenological, lumped-parameter description of the solute transport processes occurring at each node of the global graph. We refer to this node-based conservation equation as constituting an "exactly"-posed network problem, in the sense that no finer-scale model is contemplated of the unsteady-state transport process undergone by the Brownian solute particle, except, perhaps, for estimating the effective edge transport coefficients in certain limiting circumstances. The subsequent conservation equations represent the discrete counterparts of the continuous $l \oplus L$-scale convection-diffusion equation [cf. eq. (4.9)] and convection-diffusion-reaction equation (Brenner & Edwards 1993), the latter of which serve as the starting points for the method-of-moments homogenization scheme in classical generalized Taylor-Aris dispersion analyses of macrotransport phenomena.

4.1 Conditional Probability Density on the Global Graph

4.1.1 Non-Reactive Transport

Consider the conditional probability density $P(\mathbf{I}, i, t \,|\, \mathbf{I}_0, i_0, t_0)$ of the Brownian particle being located in cell $\mathbf{I}$ within the unit cell subvolume element represented by vertex i at time t, given its initial introduction at time t_0 into the network in cell $\mathbf{I}_0$ at the vertex i_0.[1] Given this impulsive introduction of the particle, and choosing $t_0 = 0$ without any loss of generality, conservation of probability density requires that P satisfy the normalization condition

$$\sum_{\Gamma_g} v(i) P(\mathbf{I}, i, t \,|\, \mathbf{I}_0, i_0) = \begin{cases} 0, & t \leq 0, \\ 1, & t > 0, \end{cases} \tag{4.1}$$

reflecting the fact that the probability is unity of the particle being located somewhere within the infinitely-extended network at any time following its initial introduction.

Since the spatially periodic network is assumed to be generated by translational displacements of the base lattice vectors, or equivalently of the simple lattice (3.4), it is assumed that the attenuation of P with distance from the point of introduction of the particle into the network is sufficiently rapid to insure that $P \to 0$ as $|\mathbf{I} - \mathbf{I}_0| \to \infty$. Indeed, in order that the summations involved in forming the local moments of P [cf. eq. (5.1)] converge, as in the continuous case (Brenner & Edwards 1993), it is further assumed that all moments of the probability density decay faster than algebraically with distance, such that

$$|(\mathbf{R}_\mathbf{I} - \mathbf{R}_{\mathbf{I}_0})^m| \, P \to 0 \quad \text{as} \quad |\mathbf{I} - \mathbf{I}_0| \to \infty \quad (m = 0, 1, 2, \ldots), \tag{4.2}$$

where, generically, for any vector $\mathbf{V}$, the polyadic $\mathbf{V}^m = \mathbf{V}\mathbf{V}\cdots\mathbf{V}$ (m-times) is an m-

[1] The cell index, $\mathbf{I}$, and its position vector counterpart, $\mathbf{R}_\mathbf{I}$, will be alternately employed in the following, as necessary.

adic.

Of course, real systems are of bounded extent. Consequently, the analysis pursued herein is expected to be valid in the limit where the number, N, of unit cells in the actual device is large: $N \gg 1$. The latter condition is equivalent to that employed previously in the continuous modeling of micropatterned devices (Dorfman & Brenner 2001), where the infinite system analysis was expected to be valid in the limit $l/L \ll 1$, with l a characteristic dimension of the unit cell and L the characteristic size of the finite macroscopic system as a whole.

As is true for both continuous (Brenner & Edwards 1993) and discrete (Adler & Brenner 1984b) unbounded models of spatially periodic systems, P is dependent only upon the global displacement $\mathbf{I} - \mathbf{I}_0$ (or, equivalently, $\mathbf{R}_\mathbf{I} - \mathbf{R}_{\mathbf{I}_0}$) of the particle from its initial position, rather than separately upon both its current and initial positions, $\mathbf{I}$ and $\mathbf{I}_0$, respectively. This fact is equivalent in its consequences to translating the arbitrarily-positioned origin, situated at $\mathbf{R} = \mathbf{0}$, to a new origin, situated at the point $\mathbf{R} = \mathbf{R}_{\mathbf{I}_0}$. As such, we can arbitrarily choose $\mathbf{I}_0 = \mathbf{0}$ and $\mathbf{R}_{\mathbf{I}_0} = \mathbf{0}$ (so that $\mathbf{I}$ and $\mathbf{R}_\mathbf{I}$ are now measured relative to an origin located within the unit cell into which the particle was originally introduced into the system). Consequently, P possesses the canonical functional form

$$P \equiv P(\mathbf{I}, i, t \,|\, i_0). \tag{4.3}$$

4.1.2 Reactive Transport

Consider the conditional reactive-probability density, $P_r\,(\mathbf{I},i,t \,|\, i_0) \geq 0$, that the solute "molecule" (particle) being tracked is instantaneously present in cell $\mathbf{I}$ and situated at vertex i at time t, given that the particle was initially introduced into cell $\mathbf{I}_0 = \mathbf{0}$ and vertex i_0 at time $t = 0$.[2] This probability density necessarily obeys the normalized

[2]We being the reactive discussion with the canonical form $P_r\,(\mathbf{I},i,t \,|\, i_0)$, equivalent to its non-reactive counterpart (4.3). The rationale involved in reducing the full reactive probability density $P_r\,(\mathbf{I},i,t \,|\, \mathbf{I_0}, i_0, t_0)$ to its canonical form is identical in the reactive case to that given above for the non-reactive probability density.

"conservation" equation

$$\sum_{i\in\Gamma g} P_r\left(\mathbf{I},i,t\,|\,i_0\right) = \begin{cases} 0, & t<0, \\ 1, & t=0, \\ <1, & t>0. \end{cases} \tag{4.4}$$

The last inequality arises from the attenuation of the total amount of solute present in the system at time $t>0$ caused by its disappearance via chemical reaction or irreversible adsorption. Indeed, after sufficient time has elapsed, the amount of solute remaining in the system, and hence its probability density, would be expected to be completely depleted [corresponding to $P_r\left(\mathbf{I},i,t\,|\,i_0\right)=0,\,\forall\left(\mathbf{I},i\right)$], a fact which will be subsequently confirmed.

As was the case for the non-reactive probability density, the reactive probability density is also required to attenuate faster than algebraically at infinity,

$$\left|\left(\mathbf{R}_{\mathbf{I}}-\mathbf{R}_{\mathbf{I}_0}\right)^m\right| P_r \to 0 \quad \text{as} \quad \left|\mathbf{I}-\mathbf{I}_0\right|\to\infty \quad (m=0,1,2,\ldots)\,. \tag{4.5}$$

4.2 Lumped-Parameter Microscale Transport

A particle navigating the network is assumed to translate through the edges via convection (either "piggy-back" convection entrained in a flowing fluid or by the action of an externally imposed force field, such as an electric field, or both), as well as by Brownian motion. In constructing the basic graph, the direction of the mean convective transport occurring within the channel, which must of necessity be unidirectional, was embedded in the edge unit vector $\mathbf{e}(j)$. Consequently, transport within the edge is fully characterized by the edge velocity vector, $U(j)\mathbf{e}(j)$, together with the edge diffusivity dyadic, $D(j)\mathbf{e}(j)\mathbf{e}(j)$.

For circumstances in which net solvent motion arises from a Darcy-scale (macroscopic) pressure gradient, the graph-theoretical techniques of Adler & Brenner (1984a) may be

applied directly to the present graphical framework. Alternatively, the network resistance models of Koplik (1982) and Adler (1985a,c) may be adopted. Such techniques furnish a coarse-grained approach for calculating the mean fluid velocity prevailing in each of the edges, without requiring detailed knowledge of the finer-scale, **r**-dependent velocity field existing therein. Although the mean *solvent* velocity may thereby be determined unambiguously, establishing the mean *solute* particle velocity $U(j)$ and diffusivity $D(j)$ is considerably more equivocal, as addressed in §1.2. Within the context of an "exact" microscale description of the solute transport process [cf. eq. (4.6)], the edge transport parameters must then be classified as stochastic variables.[3] It is important, nevertheless, to recognize that despite its stochastic nature, the edge transport process will be rendered amenable to rational analysis in the asymptotic Taylor-Aris dispersion limit in Chapters 5 and 6. Consequently, we will proceed in our "exact" analysis using the equivocal, stochastic quantities $U(j)$ and $D(j)$, reserving their unambiguous, *asymptotic* definitions for a later stage of the analysis (cf. §5.3.1).

The stochastic nature of our "exactly"-posed network problem is augmented by the mixing processes occurring in those regions situated at the channel intersections.[4] Since multiple edges j are typically associated with a single node i,[5] the preference for the solute to choose a particular edge j upon exiting node i is assumed to be governed quantitatively by a mixing parameter $K(j)$ which furnishes the probability of egress channel (edge) j for the particle as it exits intersection i [and consequently exits the unit cell subvolume $v(i)$

[3]The edge transport parameters are known *exactly* only for the specific case of infinitesimally small particles translating exclusively under the influence of an externally applied force in an isothermal fluid, since the mobility and the animating force are then each independent of position **r** within the channel.

[4]The mixing rule is the only *vertex* transport process accounted for within this discrete model. There exists no fundamental inconsistency between the continuous model, which implicitly includes convective-diffusive solute mixing processes at the channel intersections, and the present discrete model, since all sensible Lagrangian displacements within the system in the latter model are assigned to the vertex-to-vertex displacement processes occurring within the edges of the graph. Consequently, any "transport" occurring internally within the vertex results in no net Lagrangian motion on the macroscale, aside from selecting a new edge.

[5]A node possessing a single incident edge corresponds to a "dead-end" bond in the network model. The strong connectivity of the network requires that at least one node in the unit cell possess multiple incident edges.

via edge j]. So as to formulate a generic scheme, applicable to all such network problems, one may envision a set of stochastic vertex-edge probability variables, $0 \leq K(i,j) \leq 1$, characterizing the probability of the particle entering or exiting the channel represented by edge j from the channel intersection represented by vertex i.[6] However, such a set of variables overspecifies the problem, since the graphical network discretization of the real medium entailed assigning all of the physical volume to the nodes. Consequently, the constraint of zero accumulation of probability density within the volume-less edges is enforced by redefining the mixed vertex-edge parameter K as an edge-based parameter, $K(i,j) \equiv K(j)$. For definiteness, we choose the value of $K(j)$ to correspond to the probability of the particle entering the edge at its initial vertex (i.e., the probability of exiting the vertex in edge j), thereby providing internal consistency with the various mixing-rule schemes enumerated in Chapter 1.

The edge probability parameter $K(j)$ possesses an alternate interpretation as a probabilistic "check-valve" for the vertex. The extreme value $K(j) = 0$ corresponds to an edge that is inaccessible to the Brownian particle — say, a conduit of circular cross-section whose radius is less than that of the particle (the latter assumed rigid and spherical). Conversely, the extreme value $K(j) = 1$ corresponds to a channel into whom solute entry proceeds without bias. It follows that the special value $K(j) = 1$ for all edges j reproduces the earlier perfect mixing model of Adler & Brenner (1984b).

For reactive networks, it also proves necessary to specify the reaction rate constant, $k(i)$ ($k \geq 0 \; \forall i$), quantifying the rate of solute depletion when the solute is extant in the subvolume element represented by node i on the graph. Inasmuch as the reaction rate is assumed to be uniform within each subvolume element (but inhomogeneous with respect to different elements), the periodic network may be envisioned as composed of a strongly connected network of homogeneous, continuous stirred-tank flow reactors (CSTFR's).

[6]The factor $K(i,j)$ represents the probability of the particle being located within edge j, whereas $1 - K(i,j)$ is the probability of the particle remaining within vertex i. This should not be confused with the probability of the particle exiting in one of the k edges $(j_1, j_2, \ldots, j_k)$ incident to vertex i.

4.3 Nodal Conservation Equation

4.3.1 Non-Reactive Transport

Given the preceding identifications of the local transport processes occurring within the edges and vertices, the following "exact" discrete $l \oplus L$-scale conservation equation governs the conditional probability density that the particle instantaneously, at time t, resides on the global graph at the location $(\mathbf{I}, i)$:

$$v(i)\frac{dP\left(\mathbf{I},i\right)}{dt} = \delta_{\mathbf{I},\mathbf{0}}\delta_{i,i_0}\delta(t) + \sum_{\substack{j\in\Omega^+(i)\\ j=\{i',i\}}} c(j)P\left(\mathbf{I}',i'\right) + d(j)\left[P\left(\mathbf{I}',i'\right) - P\left(\mathbf{I},i\right)\right] - \\ - \sum_{\substack{j\in\Omega^-(i)\\ j=\{i,i'\}}} c(j)P\left(\mathbf{I},i\right) + d(j)\left[P\left(\mathbf{I},i\right) - P\left(\mathbf{I}',i'\right)\right], \tag{4.6}$$

with $\delta_{\mathbf{I},\mathbf{0}}$ and δ_{i,i_0} Kronecker delta functions, and $\delta(t)$ the Dirac delta function. For notational simplicity, the explicit dependence of P upon both the time t and the initial vertex location i_0 has been suppressed in its argument. The summation index $j \in \Omega^+(i)$ ($j = \{i', i\}$) serves to indicate those edges which enter vertex i from vertex i'. Likewise, $j \in \Omega^-(i)$ ($j = \{i, i'\}$) indicates edges exiting vertex i and proceeding to vertex i'. The non-negative edged-based parameters $c(j)$ and $d(j)$ appearing above correspond to the respective magnitudes of the convective and diffusive "volumetric flow rates" prevailing in edge j:[7]

$$c(j) \overset{\text{def.}}{=} K(j)U(j)A(j), \quad d(j) \overset{\text{def.}}{=} \frac{K(j)D(j)A(j)}{l(j)}. \tag{4.7}$$

The equality,

$$\sum_{\substack{j\in\Omega^+(i)\\ j=\{i',i\}}} c(j) = \sum_{\substack{j\in\Omega^-(i)\\ j=\{i,i'\}}} c(j), \tag{4.8}$$

[7] In contrast to the molecular diffusivity, the volumetric diffusive transport rate $d(j)$ may be zero if an edge is inaccessible to the particle, corresponding to $K(j) = 0$.

while always true for a solute molecule entrained in a flowing fluid with perfect mixing at intersection i (Adler & Brenner 1984a), does not necessarily obtain for imperfect mixing or purely force-driven motion. In the former case, the solute mixing bias embodied in the parameter $K(j)$ may negate the equality (4.8); in the latter case, even for perfect mixing and infinitesimally small particles, wherein both K and the (scalar) mobility M are invariant to choice of edge j, the "volumetric flow rate" is not necessarily conserved at an intersection i, say, at which an expansion in channel size occurs, such that $A(j)$ then differs between the two colinear edges incident to vertex i.

The preceding exact discrete $l \oplus L$-scale vertex conservation equation, akin to the master equations (van Kampen 1981) prevalent in statistical physics, is considerably more *ad hoc* in nature than is its continuous counterpart [cf. eq. (4.9)], thereby warranting further elaboration of the interpretation ascribed to eq. (4.6). The LHS represents the accumulation of probability density within the nodal volume given by eq. (3.5). The first term on the RHS represents the unit impulse addition at time $t_0 = 0$ of solute into unit cell $\mathbf{I}_0 = \mathbf{0}$ within the volume assigned to vertex i_0. The remaining terms respectively account for the mechanisms whereby the particle enters and exits the volume assigned to vertex $(\mathbf{I}, i)$. Explicitly, convection through the edges transports the particle from the vertex $(\mathbf{I}', i')$ to the vertex $(\mathbf{I},i)$, or, equivalently, removes the particle from vertex $(\mathbf{I},i)$. Terms involving differences, $P(\mathbf{I}',i') - P(\mathbf{I},i)$, in conditional probability densities between connected vertices account for an assumed Fickian-type diffusional process occurring as a consequence of a presumed linear probability gradient existing between the two vertices, the diffusion length scale having been explicitly incorporated *a priori* into the edge transport parameter $d(j)$.

The intractability of the stochastic difference equation (4.6) for the graphical network points up a striking contrast between the present discrete formulation and its continuous analog (Brenner & Edwards 1993). The comparable exact continuous $l \oplus L$-scale conservation counterpart of eq. (4.6), governing the conditional probability density

$P(\mathbf{R}, t \,|\, \mathbf{R}_0) \equiv P(\mathbf{R_I}, \mathbf{r}, t \,|\, \mathbf{r}_0)$, possesses the form (Brenner & Edwards 1993):

$$\frac{\partial P}{\partial t} + \nabla \cdot \left[\mathbf{U}\left(\mathbf{r}\right) P - \mathbf{D}(\mathbf{r}) \cdot \nabla P \right] = \delta\left(\mathbf{R_I}\right) \delta\left(\mathbf{r} - \mathbf{r}_0\right) \delta(t), \tag{4.9}$$

where $\mathbf{U}(\mathbf{r})$ and $\mathbf{D}(\mathbf{r})$ are, respectively, the exactly defined continuous l-scale particle velocity vector and molecular diffusivity dyadic. This latter equation possesses a well-defined mathematical and physical structure, and may be solved, at least in principle, subject to requiring an appropriate spatial rate of attenuation of P with increasing distance from the cell $\mathbf{R}_{\mathbf{I}_0} = \mathbf{0}$ at which the particle was initially introduced. In contrast, the graph-theoretical framework proposed herein possesses no exactly solvable discrete $l \oplus L$-scale formulation, except for circumstances wherein the respective mean edge transport and mixing rules are well defined, i.e. deterministic.

4.3.2 Reactive Transport

For the case of a reactive solute traversing the network, the reactive probability density, with the explicit time dependence suppressed, is governed by the following $l \oplus L$-scale convection-diffusion-reaction master equation at each node i on the global graph Γ_g:

$$\begin{aligned} v(i)\frac{dP_r(\mathbf{I},i,t \,|\, i_0)}{dt} = {} & \delta_{\mathbf{I},\mathbf{0}}\delta_{i,i_0}\delta(t) - k(i)v(i)P_r\left(\mathbf{I},i,t \,|\, i_0\right) + \\ & + \sum_{\substack{j \in \Omega^+(i) \\ j=\{i',i\}}} c(j) P_r(\mathbf{I}',i',t \,|\, i_0) + d(j) \left[\begin{array}{c} P_r(\mathbf{I}',i',t \,|\, i_0) - \\ -P_r(\mathbf{I},i,t \,|\, i_0) \end{array} \right] - \\ & - \sum_{\substack{j \in \Omega^- \\ j=\{i,i'\}}} c(j) P_r(\mathbf{I},i,t \,|\, i_0) + d(j) \left[\begin{array}{c} P_r(\mathbf{I},i,t \,|\, i_0) - \\ -P_r(\mathbf{I}',i',t \,|\, i_0) \end{array} \right], \end{aligned} \tag{4.10}$$

with $\delta_{\mathbf{I},\mathbf{0}}$ and δ_{i,i_0} Kronecker delta functions, $\delta\left(t\right)$ the Dirac delta function, and with $j = \{a, b\}$ again denoting an edge whose initial vertex is a and whose terminal vertex is b. The dependence of P_r upon the initial condition i_0 is explicitly retained in eq. (4.10). The rationale for retaining i_0 in the argument of P_r, especially when compared

to its suppression in the non-reactive case, will be discussed in Chapter 6. Proper interpretations of all but one of the terms appearing in eq. (4.10) are as discussed in the context of eq. (4.6). The new term, $k(i)v(i)P_r\left(\mathbf{I}, i, t \,|\, i_0\right)$, accounts for the CSTFR model of solute depletion, with P_r identified with the volumetric solute concentration (i.e. solute mass per unit volume).

4.4 Discrete Lagrangian Definitions of the Macrotransport Parameters

In spite of the stochastic nature of eqs. (4.6) and (4.10), their solutions at every node of the global graph furnish, in principle, the complete set of probability densities $P(\mathbf{I}, i, t \,|\, i_0)$ and $P_r\left(\mathbf{I}, i, t \,|\, i_0\right)$ there. With l the characteristic unit cell linear dimension and D_m the characteristic Brownian particle molecular diffusivity, the asymptotic definitions of the macrotransport parameters $\bar{K}^*$, $\bar{\mathbf{U}}^*$ and $\bar{\mathbf{D}}^*$ become valid in the long-time limit, $t \gg l^2/D_m$ (Brenner & Edwards 1993).[8] The proper Langrangian interpretations of these parameters (Brenner & Edwards 1993), which differ in the respective reactive and non-reactive cases, are discussed below.

The non-reactive case, being more straightforward, is the subject of our initial discourse. With $\mathbf{R}_{\mathcal{I}} \equiv \mathbf{R}_{\mathbf{I}} + \mathbf{r}_i$ the location of the centroid of vertex i in unit cell $\mathbf{I}$ within which the particle is instantaneously located at time t, the solution of eq. (4.6) for P permits calculation of the mean particle velocity vector $\bar{\mathbf{U}}^*$ as the average displacement of a non-reactive Brownian particle with respect to its initial position $\mathbf{R}_{\mathcal{I}_0} \equiv \mathbf{0} + \mathbf{r}_{i_0}$ (Brenner & Edwards 1993):

$$\langle \mathbf{R}_{\mathcal{I}} - \mathbf{r}_{i_0} \rangle = \langle \mathbf{R}_{\mathcal{I}} \rangle - \mathbf{r}_{i_0} \approx \bar{\mathbf{U}}^* t, \tag{4.11}$$

with angular brackets defined below in eq. (4.13). Similarly, calculation of the disper-

[8] An additional asymptotic requirement will be imposed in the reactive network case [cf. eq. (6.24)].

sivity dyadic $\bar{\mathbf{D}}^*$ follows from knowledge of the mean-squared vector displacement of the Brownian particle from its mean position $\langle \mathbf{R}_{\mathcal{I}} \rangle$ at time t (Brenner & Edwards 1993):

$$\langle [\mathbf{R}_{\mathcal{I}} - \langle \mathbf{R}_{\mathcal{I}} \rangle] [\mathbf{R}_{\mathcal{I}} - \langle \mathbf{R}_{\mathcal{I}} \rangle] \rangle \approx 2\bar{\mathbf{D}}^* t. \tag{4.12}$$

The average values appearing in these expressions represent summations over the global graph:

$$\langle \mathbf{R}_{\mathcal{I}} \rangle = \sum_{\Gamma_g} (\mathbf{R}_{\mathbf{I}} + \mathbf{r}_i) \, P(\mathbf{I}, i, t \,|\, i_0). \tag{4.13}$$

Since the decay of the transient solution of eq. (4.6) is exponential in time (Brenner & Edwards 1993), the average values defined above become asymptotically independent of i_0 (and, equivalently, $\mathbf{r}_{i_0}$). This tendency of the particle to lose "memory" of the position i_0 of its initial local (vertex) introduction into the network proves fundamental in the asymptotic theory to follow (cf. §5.3.1).

The proper Lagrangian interpretations of the mean transport rates for reactive solutes are altered when compared to their non-reactive counterparts, since the total probability density eventually decays to zero by virtue of the chemical depletion reactions occuring within the network. Indeed, if one were to naively replace $P\,(\mathbf{I},i,t \,|\, i_0)$ with $P_r\,(\mathbf{I},i,t \,|\, i_0)$ in eq. (4.13), $\bar{\mathbf{U}}^*$ and $\bar{\mathbf{D}}^*$ would vanish at long times by eqs. (4.11)-(4.12)! Instead of focusing upon the true reactive solute probability density, P_r, it proves necessary to consider instead the survival probability density (Brenner & Edwards 1993, Shapiro & Brenner 1986),[9]

$$M_{0r}(t \,|\, i_0) \stackrel{\text{def.}}{=} \sum_{\Gamma_g} v(i) P_r(\mathbf{I}, i, t \,|\, i_0), \tag{4.14}$$

which represents the global conditional probability density that the initial input of solute is still present somewhere within the network (the global graph) at time t. Summing eq.

[9]We use the notation M_{0r}, in accordance with Brenner & Edwards (1993), to denote the zeroth-order global moment of the reactive probability density. This should not be confused with other global moments for the reactive networks which will be defined later [cf. eqs. (6.9)-(6.10)].

(4.10) over Γ_g furnishes the differential equation governing M_{0r},

$$\frac{dM_{0r}}{dt} = \delta\,(t) - \sum_{\Gamma_g} k(i)v(i)P_r(\mathbf{I}, i, t \,|\, i_0), \tag{4.15}$$

where we have made use of the attenuation condition (4.5), as well as the strong connectivity of the graph [cf. eqs. (6.13)- (6.14)]. The structure of eq. (4.15), when combined with the restriction $k(i) \geq 0 \;\forall\; i$, dictates that the survival probability density M_{0r} decrease monotonically for all times t after the introduction of the solute into the network at time $t = 0$. In order for our macrotransport theory be an accurate asymptotic representation of the long-time averaged solute transport processes, the proper Langrangian definitions of $\bar{K}^*$, $\bar{\mathbf{U}}^*$ and $\bar{\mathbf{D}}^*$ must reflect the fact that the solute is being depleted for all times. In accordance with Shapiro & Brenner (1986), these parameters possess the asymptotic forms

$$M_{or} \;\approx\; \exp\left(-\bar{K}^* t\right), \tag{4.16}$$

$$\langle \mathbf{R}_{\mathcal{I}} \rangle_r - \mathbf{r}_{i_0} \;\approx\; \bar{\mathbf{U}}^* t, \tag{4.17}$$

$$\left\langle [\mathbf{R}_{\mathcal{I}} - \langle \mathbf{R}_{\mathcal{I}} \rangle_r]\,[\mathbf{R}_{\mathcal{I}} - \langle \mathbf{R}_{\mathcal{I}} \rangle_r] \right\rangle_r \;\approx\; 2\bar{\mathbf{D}}^* t, \tag{4.18}$$

where the "reactive" average values of the reactive probability density are normalized by the global survival probability density,

$$\langle \mathbf{R}_{\mathcal{I}} \rangle_r = (M_{0r})^{-1} \sum_{\Gamma_g} (\mathbf{R}_{\mathbf{I}} + \mathbf{r}_i)\, P_r(\mathbf{I}, i, t \,|\, i_0). \tag{4.19}$$

In essence, the normalization factor M_{0r} negates the contribution of the depleted solute to the overall transport rates, thereby rendering the parameters $\bar{\mathbf{U}}^*$ and $\bar{\mathbf{D}}^*$ accurate asymptotic representations of the mean transport rates of those solutes which are still present in the network at time t. Inasmuch as the survival probability density for the non-reactive case is unity by eq. (4.1) (ie. $M_{ro} = 1$), the definitions (4.16)-(4.18) reduce

to their non-reactive counterparts, (4.11) and (4.12), where we would also have $\bar{K}^* = 0$.

Chapter 5

Method of Moments: Non-Reactive Transport

Calculation of the macrotransport parameters $\bar{\mathbf{U}}^*$ and $\bar{\mathbf{D}}^*$ from the present network model derives via a Taylor-Aris-like moment-matching scheme for the asymptotic global moments of the probability density, as detailed in §5.3. As a prelude to this, we invoke the generic scheme employed by Adler & Brenner (1984b) to calculate these moments prior to effecting their asymptotic expansions, including appropriate modifications allowing for the incorporation of molecular diffusion effects into the analysis. Consideration of the reactive master equation (4.10) is deferred to Chapter 6.

5.1 Local Moments

Define the m^{th}-local moment ($m = 0, 1, 2, \ldots$) of the conditional probability density as the m-adic,[1]

$$\mathbf{P}_m(i,t\,|\,i_0) \stackrel{\text{def.}}{=} \sum_{\mathbf{I}} (\mathbf{R}_\mathbf{I})^m\, P\,(\mathbf{I},i,t\,|\,i_0)\,, \tag{5.1}$$

the indicated summation being defined as the triple sum over all unit cell indices:

$$\sum_{\mathbf{I}} \stackrel{\text{def.}}{=} \sum_{I_1=-\infty}^{\infty} \sum_{I_2=-\infty}^{\infty} \sum_{I_3=-\infty}^{\infty}\,. \tag{5.2}$$

The differential equation governing $\mathbf{P}_m$ is formed by multiplying the node conservation equation (4.6) by the quantity $(\mathbf{R}_\mathbf{I})^m \equiv \mathbf{R}_\mathbf{I}\mathbf{R}_\mathbf{I}\cdots\mathbf{R}_\mathbf{I}$ (m-times), and subsequently performing the triple summation (5.2), thereby furnishing the following ordinary differential equation for $\mathbf{P}_m(i,t\,|\,i_0)$:

$$\begin{aligned} v(i)\frac{d\mathbf{P}_m(i,t\,|\,i_0)}{dt} = {} & \delta_{i,i_0}\delta_{m,0}\delta(t) + \sum_{\substack{j\in\Omega^+(i)\\ j=\{i',i\}}} [c(j)+d(j)] \left[\sum_{\mathbf{I}} (\mathbf{R}_\mathbf{I})^m\, P\,(\mathbf{I}',i',t\,|\,i_0)\right] - \\ & - \sum_{\substack{j\in\Omega^+(i)\\ j=\{i',i\}}} d(j)\mathbf{P}_m(i,t\,|\,i_0) - \sum_{\substack{j\in\Omega^-(i)\\ j=\{i,i'\}}} [c(j)+d(j)]\,\mathbf{P}_m(i,t\,|\,i_0) + \\ & + \sum_{\substack{j\in\Omega^-(i)\\ j=\{i,i'\}}} d(j) \left[\sum_{\mathbf{I}} (\mathbf{R}_\mathbf{I})^m\, P\,(\mathbf{I}',i',t\,|\,i_0)\right], \end{aligned} \tag{5.3}$$

where $\delta_{m,0}$ is a Kronecker delta function. Whereas the ordinary differential equation governing the evolution of P itself on the global graph requires detailed information regarding the behavior of P throughout the entire infinite network, the solution of the governing equations for $\mathbf{P}_m$ is contained wholly within the local graph Γ_l.

[1] In what follows, infinite summations effected over discrete variables constitute counterparts of infinite $\mathbf{R}$-space quadratures effected over continuous variables employed in generalized Taylor-Aris dispersion analyses of continuous systems (Brenner & Edwards 1993). Similarily, the subsequent mathematical manipulations of the resulting sums in (5.1) constitute discrete counterparts of "integration by parts" in quadratures of continuous variables.

Evaluation of sums involving terms of the type $(\mathbf{R_I})^m P(\mathbf{I}', i', t \,|\, i_0)$ appearing in eq. (5.3) may be effected by adding and subtracting $\mathbf{R_{I'}}$, as follows (Adler & Brenner 1984b):

$$\mathbf{R_I} = (\mathbf{R_I} - \mathbf{R_{I'}}) + \mathbf{R_{I'}} = \mathbf{R}(j) + \mathbf{R_{I'}}, \tag{5.4}$$

whereupon the first few moments are found to obey the following sequence of recurrence relations:

$$\begin{aligned} v(i)\frac{dP_0(i,t \,|\, i_0)}{dt} = {} & \delta_{i,i_0}\delta(t) + \sum_{\substack{j\in\Omega^+(i)\\ j=\{i',i\}}} c(j)P_0(i',t \,|\, i_0) + d(j)\left[P_0(i',t \,|\, i_0) - P_0(i,t \,|\, i_0)\right] - \\ & - \sum_{\substack{j\in\Omega^-(i)\\ j=\{i,i'\}}} c(j)P_0(i,t \,|\, i_0) + d(j)\left[P_0(i,t \,|\, i_0) - P_0(i',t \,|\, i_0)\right], \end{aligned} \tag{5.5}$$

$$\begin{aligned} v(i)\frac{d\mathbf{P}_1(i,t \,|\, i_0)}{dt} = {} & \sum_{\substack{j\in\Omega^+(i)\\ j=\{i',i\}}} c(j)\left[\mathbf{R}(j)P_0(i',t \,|\, i_0) + \mathbf{P}_1(i',t \,|\, i_0)\right] - \sum_{\substack{j\in\Omega^-(i)\\ j=\{i,i'\}}} c(j)\mathbf{P}_1(i,t \,|\, i_0) + \\ & + \sum_{\substack{j\in\Omega^+(i)\\ j=\{i',i\}}} d(j)\left[\mathbf{R}(j)P_0(i',t \,|\, i_0) + \mathbf{P}_1(i',t \,|\, i_0) - \mathbf{P}_1(i,t \,|\, i_0)\right] - \\ & - \sum_{\substack{j\in\Omega^-(i)\\ j=\{i,i'\}}} d(j)\left[\mathbf{P}_1(i,t \,|\, i_0) - \mathbf{P}_1(i',t \,|\, i_0) + \mathbf{R}(j)P_0(i',t \,|\, i_0)\right], \end{aligned} \tag{5.6}$$

$$v(i)\frac{d\mathbf{P}_2\left(i,t\,|\,i_0\right)}{dt} = \sum_{\substack{j\in\Omega^+(i)\\ j=\{i',i\}}} c(j)\left[\begin{array}{c}\mathbf{R}(j)\mathbf{R}(j)P_0\left(i',t\,|\,i_0\right)+\mathbf{R}(j)\mathbf{P}_1\left(i',t\,|\,i_0\right)+\\ +\mathbf{P}_1\left(i',t\,|\,i_0\right)\mathbf{R}(j)+\mathbf{P}_2\left(i',t\,|\,i_0\right)\end{array}\right] -$$
$$- \sum_{\substack{j\in\Omega^-(i)\\ j=\{i,i'\}}} c(j)\mathbf{P}_2\left(i,t\,|\,i_0\right) +$$
$$+ \sum_{\substack{j\in\Omega^+(i)\\ j=\{i',i\}}} d(j)\left[\begin{array}{c}\mathbf{R}(j)\mathbf{R}(j)P_0\left(i',t\,|\,i_0\right)+\mathbf{R}(j)\mathbf{P}_1\left(i',t\,|\,i_0\right)+\\ +\mathbf{P}_1\left(i',t\,|\,i_0\right)\mathbf{R}(j)+\mathbf{P}_2\left(i',t\,|\,i_0\right)-\mathbf{P}_2\left(i,t\,|\,i_0\right)\end{array}\right] -$$
$$- \sum_{\substack{j\in\Omega^-(i)\\ j=\{i,i'\}}} d(j)\left[\begin{array}{c}\mathbf{P}_2\left(i,t\,|\,i_0\right)-\mathbf{R}(j)\mathbf{R}(j)P_0\left(i',t\,|\,i_0\right)+\\ +\mathbf{R}(j)\mathbf{P}_1\left(i',t\,|\,i_0\right)+\mathbf{P}_1\left(i',t\,|\,i_0\right)\mathbf{R}(j)-\mathbf{P}_2\left(i',t\,|\,i_0\right)\end{array}\right]. \tag{5.7}$$

The appearance of the macroscopic jump vector in the summations over $j \in \Omega^-(i)$ in eqs. (5.6)-(5.7) necessitates using $-\mathbf{R}(j)$, rather than $\mathbf{R}(j)$, owing to the fact that the macroscopic jump vector was previously defined in eq. (3.2) for edges *entering* the unit cell, whereas that in $j \in \Omega^-(i)$ involves edges *exiting* the unit cell. It is trivial to show that the macroscopic jump vector for an edge exiting the unit cell is equal in magnitude and opposite in direction to that for a homologous edge entering the unit cell; hence, the change in algebraic sign. The latter issue, solely a by-product of incorporating molecular diffusion into our model, did not arise in the prior, exclusively convective, solute transport model of Adler & Brenner (1984b).

With the continued presence of the unit impulse, appearing in the differential equation for the zeroth-order moment (5.5), the conservation principle embodied in eq. (4.1) for the global graph adopts the form

$$\sum_{i\in V\Gamma_l} v(i)P_0\left(i,t\,|\,i_0\right) = 1 \qquad (t>0)\,, \tag{5.8}$$

reflecting the unitary probability that the particle is located for all times after its introduction into the network within some unit cell subvolume element. In contrast,

higher-order local moments are not similarly "conserved," but rather grow in time.

5.2 Global Moments

Define the m^{th}-global-moment ($m = 0, 1, 2, \ldots$) as the m-adic,

$$\mathbf{M}_m(t \,|\, i_0) \stackrel{\text{def.}}{=} \sum_{i \in V\Gamma_l} v(i) \mathbf{P}_m \left(i, t \,|\, i_0\right). \tag{5.9}$$

In performing summations over the local graph, it is useful to note that for a given nodal quantity $\phi(i)$ and edge quantity $\epsilon(j)$, the strong connectivity of the graph furnishes the identity:

$$\sum_{\substack{j \in E\Gamma_l \\ j \in \Omega^+}} \epsilon(j) \phi(i') = \sum_{\substack{j \in E\Gamma_l \\ j \in \Omega^-}} \epsilon(j) \phi(i). \tag{5.10}$$

In expressing the latter, we have made use of the compact summation notation,

$$\sum_{\substack{j \in E\Gamma_l \\ j \in \Omega^+}} \stackrel{\text{def.}}{=} \sum_{i \in V\Gamma_l} \sum_{\substack{j \in \Omega^+(i) \\ j = \{i', i\}}}, \qquad \sum_{\substack{j \in E\Gamma_l \\ j \in \Omega^-}} \stackrel{\text{def.}}{=} \sum_{i \in V\Gamma_l} \sum_{\substack{j \in \Omega^-(i) \\ j = \{i, i'\}}}. \tag{5.11}$$

To arrive at the differential equations governing the global moments, differentiate eq. (5.9) with respect to time and substitute the resulting expression into the appropriate local moment from eqs. (5.5)-(5.7), using the identity (5.10). For the zeroth-order moment, this procedure yields

$$\frac{dM_0}{dt} = \delta(t). \tag{5.12}$$

The latter relation expresses the conservation of total probability principle (4.1), which is directly verified by integrating eq. (5.12) to obtain

$$M_0 = \begin{cases} 0, & t \leq 0, \\ 1, & t > 0, \end{cases} \tag{5.13}$$

independently of i_0.

As regards higher-order moments, the first- and second-order global moments obey the respective equations:

$$\frac{d\mathbf{M}_1(t\,|\,i_0)}{dt} = \sum_{\substack{j\in E\Gamma_l \\ j\in\Omega^+}} [c(j)+d(j)]\,\mathbf{R}(j)P_0\,(i',t\,|\,i_0) - \sum_{\substack{j\in E\Gamma_l \\ j\in\Omega^-}} d(j)\mathbf{R}(j)P_0\,(i',t\,|\,i_0)\,, \tag{5.14}$$

$$\begin{aligned}\frac{d\mathbf{M}_2(t\,|\,i_0)}{dt} = &\sum_{\substack{j\in E\Gamma_l \\ j\in\Omega^+}} [c(j)+d(j)] \left[\begin{array}{l} \mathbf{R}(j)\mathbf{R}(j)P_0\,(i',t\,|\,i_0) + \mathbf{R}(j)\mathbf{P}_1\,(i',t\,|\,i_0) + \\ +\mathbf{P}_1\,(i',t\,|\,i_0)\,\mathbf{R}(j) \end{array}\right] + \\ &+ \sum_{\substack{j\in E\Gamma_l \\ j\in\Omega^-}} d(j) \left[\begin{array}{l} \mathbf{R}(j)\mathbf{R}(j)P_0\,(i',t\,|\,i_0) - \mathbf{R}(j)\mathbf{P}_1\,(i',t\,|\,i_0) - \\ -\mathbf{P}_1\,(i',t\,|\,i_0)\,\mathbf{R}(j) \end{array}\right]. \end{aligned} \tag{5.15}$$

5.3 Asymptotic, Long-Time Limits

5.3.1 Zeroth-Order Moments

Asymptotic integration of the zeroth-order local moment equation (5.5) furnishes the long-time solution

$$P_0\,(i,t\,|\,i_0) \approx P_0^\infty(i) + \text{exp.} \tag{5.16}$$

Here and hereafter, the generic symbol "exp" denotes terms that are exponentially attenuated in time as $t\to\infty$. As was true of the continuous paradigm counterpart $P_0^\infty(\mathbf{r})$ to eq. (5.16) (Brenner & Edwards 1993), the time-independent probability density $P_0^\infty(i)$ is unconditional, whereby the probability of locating the Brownian particle at vertex i becomes independent of the initial local vertex i_0 of its introduction into the network. Substitution of eq. (5.16) into both eq. (5.5) and eq. (5.8) furnishes the following steady-

state conservation equation for $P_0^\infty(i)$:

$$\sum_{\substack{j\in\Omega^+(i)\\ j=\{i',i\}}} c(j)P_0^\infty(i') + d(j)\left[P_0^\infty(i') - P_0^\infty(i)\right] -$$

$$- \sum_{\substack{j\in\Omega^-(i)\\ j=\{i,i'\}}} c(j)P_0^\infty(i) + d(j)\left[P_0^\infty(i) - P_0^\infty(i')\right] = 0, \tag{5.17}$$

supplemented by the requisite normalization condition,

$$\sum_{i\in V\Gamma_l} v(i)P_0^\infty(i) = 1. \tag{5.18}$$

The latter pair of equations governing $P_0^\infty(i)$ constitute the discrete analogs of the comparable continuous conservation equation and normalization condition governing the continuous intracellular field $P_0^\infty(\mathbf{r})$ arising in classical continuous macrotransport theory (Brenner & Edwards 1993). Moreover, in the presence of vanishing molecular diffusivity and conserved convective transport (4.8), the probability density tends towards the asymptotic value $P_0^\infty(i) = \tau_0^{-1}$ for all i, in accord with the results of Adler & Brenner (1984b) for that case.

Edge Transport Properties in the Long-Time Limit

The equivocal nature of the edge transport properties, which hindered a deterministic solution of the discrete "exact" $l \oplus L$-scale governing equation (4.6), vanishes in the long-time Taylor-Aris dispersion limit, $t \gg l^2/D_m$. Explicitly, satisfaction of the latter inequality assures that the Brownian particle has had the opportunity to sample *all* locations i within the unit cell numerous times, effectively achieving an equilibrium distribution $P_0^\infty(i)$ with respect to its local position. Since the characteristic transverse linear dimension H of a channel is assumed to be less than the length l of the unit cell (often $H \ll l$), the Brownian particle will, concomitantly, have had the opportunity to sample all channel locations within each subvolume element $v(i)$ of the cell numer-

ous times. Consequently, achieving the asymptotic long-time limit necessitates that $t \gg H^2/D_m$, whereby the edge velocity $U(j)$ and diffusivity $D(j)$ represent *mean* l-scale solute transport properties, arising from numerous samplings of the individual channels within a cell. The latter parameters may be obtained either: (i) experimentally, using a single long channel so as to satisfy the inequality $t \gg H^2/D_m$ (where $t = l/U$ is the nominal holdup time of the particle traversing the channel of length l with mean velocity U) before the particle exits the experimental channel; or (ii) via classical macrotransport theory (Brenner & Edwards 1993), in circumstances where hydrodynamic fluid-particle data exists.

As a further consequence of attaining this asymptotic limit, the exit channel parameter $K(j)$ constitutes the *equilibrium* distribution of edge choices. For diffusion dominated transport processes it is our contention that the hindered-diffusion partition coefficient (Deen 1987) governs the probability of the particle choosing differing intersectional egress channels, inasmuch as the partition coefficient is an equilibrium property. This coefficient may be derived rigorously, enabling systematic incorporation of a vast array of effects, including steric and electrostatic hindrances (Deen 1987).

This ability to furnish formal definitions for the requisite transport parameters in a rigorous, well-defined, and experimentally realizable long-time limit renders the present discrete generalized Taylor-Aris dispersion scheme markedly less equivocal than previous network models (Andrade *et al.* 1992, Bruderer & Bernabe 2001, de Arcangelis *et al.* 1986, Koplik *et al.* 1988, McGreavy *et al.* 1990, Meyers & Liapis 1998, Sahimi 1992, Sahimi & Jue 1989, Sorbie & Clifford 1991, Zhang & Seaton 1994) of periodically configured systems.

Solution for $P_0^\infty(i)$ in the Cocycle Space

In order to facilitate a formal matrix solution for the probability density, define the $n \times 1$ vector $\mathbf{P}$ whose rows are the probability densities $P_0^\infty(i)$. In addition, define the following

pair of $m \times m$ diagonal matrices containing the effective edge transport parameters:[2]

$$\mathbf{c} = c(j)\delta_{i,j}, \qquad \mathbf{d} = d(j)\delta_{i,j}, \tag{5.19}$$

where $\delta_{i,j}$ is the Kronecker delta function. These definitions permit the conservation equation (5.17) to be represented in the compact matrix form

$$\mathbf{D}\cdot\left[(\mathbf{c}+\mathbf{d})\cdot\left(\Pi^{(-)}\right)^{\dagger} - \mathbf{d}\cdot\left(\Pi^{(+)}\right)^{\dagger}\right]\cdot\mathbf{P} = \mathbf{0}, \tag{5.20}$$

with $\dagger$ the transposition operator. Clearly, eq. (5.20) is satisfied by the trivial solution $\mathbf{P} = \mathbf{0}$ for the n vector elements $P_0^{\infty}(i)$, since the incidence matrix $\mathbf{D}$ is of rank $n-1$. Indeed, this rank-deficient property of the incidence matrix necessitates retaining the probability density normalization condition (4.1) in the asymptotic limit. To incorporate this normalization condition into the formal solution, define the $(n-1)\times n$ coefficient matrix $\mathcal{A}$,

$$\mathcal{A} \stackrel{\text{def.}}{=} \mathbf{K}^{\dagger}\cdot\left[(\mathbf{c}+\mathbf{d})\cdot\left(\Pi^{(-)}\right)^{\dagger} - \mathbf{d}\cdot\left(\Pi^{(+)}\right)^{\dagger}\right], \tag{5.21}$$

as well as the $1\times n$ vector of the nodal volumes,

$$\mathbf{v} \stackrel{\text{def.}}{=} v(i). \tag{5.22}$$

These permit the linearly independent, rank n matrix equation for the probability density to be expressed in the partitioned matrix form,

$$\begin{bmatrix} \mathcal{A} \\ \mathbf{v} \end{bmatrix}\cdot\mathbf{P} = \begin{bmatrix} \mathbf{0} \\ 1 \end{bmatrix}. \tag{5.23}$$

[2]The matrices $\mathbf{c}$ and $\mathbf{d}$ in the present scheme correspond to transition matrices in classical statistical physics (van Kampen 1981).

5.3.2 First-Order Moments

Mean Velocity Vector $\bar{\mathbf{U}}^*$

As in classical generalized Taylor-Aris dispersion theory (Brenner & Edwards 1993), the mean particle velocity vector may be calculated from the following asymptotic expression derived from eqs. (4.11), (4.13), (5.1) and (5.9):

$$\bar{\mathbf{U}}^* = \lim_{t\to\infty} \frac{d\mathbf{M}_1}{dt}. \tag{5.24}$$

Substitution of (5.14) into the latter, together with use of eqs. (5.10) and (5.16), enables $\bar{\mathbf{U}}^*$ to be calculated from knowledge of $P_0^\infty(i)$ via the following generic paradigmatic relation:

$$\bar{\mathbf{U}}^* = \sum_{\substack{j\in E\Gamma_l \\ j\in\Omega^+}} c(j)\mathbf{R}(j)P_0^\infty(i') + d(j)\mathbf{R}(j)\left[P_0^\infty(i') - P_0^\infty(i)\right]. \tag{5.25}$$

Upon setting $d(j) = 0\ \forall j$ and $P_0^\infty(i') = \tau_0^{-1}$, the latter agrees with the expression previously derived elsewhere by Adler & Brenner (1984b) for the case of purely convective solute transport.

Derivation of the B-Equation

Assume, subject to *a posteriori* verification, an asymptotic trial solution of the form

$$\mathbf{P}_1(i,t\,|\,i_0) \approx P_0^\infty(i)\left[\bar{\mathbf{U}}^* t + \mathbf{B}(i)\right] + \exp, \tag{5.26}$$

with $\mathbf{B}(i)$ a time- and i_0-independent vector to be determined. Introduce eqs. (5.16) and (5.26) into eq. (5.6), subsequently canceling time-dependent terms with eq. (5.17), so as to arrive at the following difference equation governing the vector $\mathbf{B}(i)$ at each node on

the local graph:

$$\sum_{\substack{j\in\Omega^+(i)\\ j=\{i',i\}}} c(j)P_0^\infty(i')\,\mathbf{B}(i') + d(j)\left[P_0^\infty(i')\mathbf{B}(i') - P_0^\infty(i)\mathbf{B}(i)\right] -$$
$$- \sum_{\substack{j\in\Omega^-(i)\\ j=\{i,i'\}}} c(j)P_0^\infty(i)\mathbf{B}(i) + d(j)\left[P_0^\infty(i)\mathbf{B}(i) - P_0^\infty(i')\mathbf{B}(i')\right] = v(i)P_0^\infty(i)\bar{\mathbf{U}}^* - \alpha(i), \tag{5.27}$$

with $\alpha(i)$ the node-based vector

$$\alpha(i) = \sum_{\substack{j\in\Omega^+(i)\\ j=\{i',i\}}} \left[c(j)+d(j)\right]\mathbf{R}(j)P_0^\infty(i') - \sum_{\substack{j\in\Omega^-(i)\\ j=\{i,i'\}}} d(j)\mathbf{R}(j)P_0^\infty(i'). \tag{5.28}$$

It is readily confirmed from eqs. (5.17) and (5.27), as was true for both continuous (Brenner & Edwards 1993) and non-diffusive discrete (Adler & Brenner 1984b) generalized Taylor-Aris modeling, that the $\mathbf{B}$ vector is uniquely defined only to within an arbitrary additive constant vector. Moreover, as in those earlier cases, the forcing function appearing on the RHS of eq. (5.27) represents the difference between the mean and "local" vertex velocities. This velocity disparity furnishes the physical mechanism underlying the origin of dispersion within the network. The time- and i_0-independence of the equation governing $\mathbf{B}(i)$ observed in eq. (5.27) furnishes *a posteriori* verification of the assumed trial solution (5.26) for $\mathbf{P}_1$. This "transport equation" for the $\mathbf{B}$-field plays a fundamental role in subsequent dispersion calculations. Its solution within the cocycle space is discussed forthwith.

Substitution of eq. (5.26) into eq. (5.9) (with $m = 1$), together with use of eq. (5.18), furnishes the following asymptotic form for $\mathbf{M}_1$:

$$\mathbf{M}_1(t) \approx \bar{\mathbf{U}}^* t + \bar{\mathbf{B}} + \exp, \tag{5.29}$$

wherein $\bar{\mathbf{B}}$ is the time-independent constant vector

$$\bar{\mathbf{B}} = \sum_{i \in V\Gamma_l} v(i) P_0^{\infty}(i)\, \mathbf{B}(i). \tag{5.30}$$

Solution of the B-Equation in the Cocycle Space

Since each of the n different $\mathbf{B}$-vectors may be determined only to within a single arbitrary, additive constant, say, $\mathbf{B}(i^*)$, the $n-1$ dimensional cocycle space furnishes a systematic method for identifying the basis node i^* as that not appearing in the basis set of the cocycle space.[3] Adapting the method of Adler & Brenner (1984b) to the problem at hand, define the following pair of $m \times 3$ matrices:

$$\beta^-(j) = P_0^{\infty}(i) \left[\mathbf{B}^{\dagger}(i) - \mathbf{B}^{\dagger}(i^*)\right] \quad \left[j \in \Omega^-(i)\right], \tag{5.31}$$

$$\beta^+(j) = P_0^{\infty}(i) \left[\mathbf{B}^{\dagger}(i) - \mathbf{B}^{\dagger}(i^*)\right] \quad \left[j \in \Omega^+(i)\right], \tag{5.32}$$

as well as the $(n-1) \times 3$ matrix,

$$\alpha^*(i) = \left[v(i) P_0^{\infty}(i) \bar{\mathbf{U}}^* - \alpha(i)\right]^{\dagger} \quad (i \neq i_0). \tag{5.33}$$

With use of the preceding matrix definitions, eq. (5.27) may be recast into the compact matrix form,

$$\mathbf{K}^{\dagger} \cdot \left[(\mathbf{c} + \mathbf{d}) \cdot \beta^- - \mathbf{d} \cdot \beta^+\right] = \alpha^*. \tag{5.34}$$

Eventual computation of the dispersivity [cf. eq. (5.47)] necessitates use of the edge-based vector,

$$\mathbf{b}(j) \stackrel{\text{def.}}{=} \mathbf{B}(i) - \mathbf{B}(i') \quad (j = \{i', i\}), \tag{5.35}$$

where the edge is oriented with its initial vertex at i'. Define an $m \times 3$ matrix, $\mathbb{B}$, whose

[3] Any arbitrary scheme may be invoked for specifying the value of an arbitrary reference node i^*. Our choice of the cocycle space is made solely for consistency with the graph theoretical techniques (Bollobas 1979) outlined in §3.4. Indeed, use of the cocycle space will prove unnecessary in the reactive case.

rows are the vectors $\mathbf{b}^{\dagger}(j)$, the matrix $\mathbb{B}$ being computed from the relationships (Adler & Brenner 1984b):

$$\beta^{-}(j) = \mathcal{B}^{-} \cdot \mathbb{B}, \quad \beta^{+}(j) = \mathcal{B}^{+} \cdot \mathbb{B}, \tag{5.36}$$

where $\mathcal{B}^{-}$ and $\mathcal{B}^{+}$ are $m \times m$ matrices involving the probability density $P_0^{\infty}(i)$. Consequently, eq. (5.34) may be rewritten as

$$\mathbf{K}^{\dagger} \cdot \left[(\mathbf{c} + \mathbf{d}) \cdot \mathcal{B}^{-} - \mathbf{d} \cdot \mathcal{B}^{+} \right] \cdot \mathbb{B} = \alpha^{*}. \tag{5.37}$$

Although the $(n-1) \times m$ coefficient matrix $\mathbf{K}^{\dagger} \cdot [(\mathbf{c} + \mathbf{d}) \cdot \mathcal{B}^{-} - \mathbf{d} \cdot \mathcal{B}^{+}]$ is not square, it is always possible to augment the coefficient matrix with additional rows containing the null sum of $\mathbf{b}(j)$ vectors along a cycle of the graph (Berge 1973), with concomitant rows of zeros in the solution vector α^{*}.

5.3.3 Second-Order Moments

Substitute the asymptotic solutions (5.16) and (5.26) into eq. (5.15), making use of eq. (5.25), so as to arrive at the following asymptotic expression for the second-order global moment:

$$\begin{aligned} \frac{d\mathbf{M}_2(t)}{dt} \approx 2\bar{\mathbf{U}}^{*}\bar{\mathbf{U}}^{*}t + \sum_{\substack{j \in E\Gamma_l \\ j \in \Omega^{+}}} [c(j) + d(j)] \, P_0^{\infty}(i') \left[\mathbf{R}(j)\mathbf{R}(j) + \mathbf{R}(j)\mathbf{B}(i') + \mathbf{B}(i')\,\mathbf{R}(j) \right] + \\ + \sum_{\substack{j \in E\Gamma_l \\ j \in \Omega^{-}}} d(j) P_0^{\infty}(i') \left[\mathbf{R}(j)\mathbf{R}(j) - \mathbf{R}(j)\mathbf{B}(i') - \mathbf{B}(i')\,\mathbf{R}(j) \right] + \exp. \end{aligned} \tag{5.38}$$

The dispersivity dyadic may be computed from the following expression (Brenner & Edwards 1993), derived from eqs. (4.12), (4.13), (5.1) and (5.9):

$$\bar{\mathbf{D}}^{*} = \frac{1}{2} \lim_{t \to \infty} \frac{d}{dt} \left(\mathbf{M}_2 - \mathbf{M}_1\mathbf{M}_1 \right). \tag{5.39}$$

The RHS of the latter may be evaluated by use of eqs. (5.25), (5.29), (5.30) and (5.38), together with use of the definition of the $\mathbf{b}(j)$ vector (5.35) and eq. (5.10), to eventually furnish the formula

$$\bar{\mathbf{D}}^* = \mathrm{sym} \sum_{\substack{j\in E\Gamma_l \\ j\in\Omega^+}} \left\{ c(j) P_0^\infty(i') + d(j) \left[P_0^\infty(i') + P_0^\infty(i) \right] \right\} \begin{bmatrix} \frac{1}{2}\mathbf{R}(j)\mathbf{R}(j) - \\ -\mathbf{R}(j)\mathbf{b}(j) \end{bmatrix} + \mathrm{sym}(\mathbf{E}), \tag{5.40}$$

with $\mathbf{E}$ the tensor

$$\mathbf{E} = \sum_{i\in V\Gamma_l} \left[\alpha(i)\mathbf{B}(i) - v(i) P_0^\infty(i)\, \bar{\mathbf{U}}^* \mathbf{B}(i) \right]. \tag{5.41}$$

Notationally, the symmetry operator for a generic matrix $\mathbf{XY}$ is defined by the expression

$$\mathrm{sym}(\mathbf{XY}) \stackrel{\mathrm{def.}}{=} \frac{1}{2}(\mathbf{XY} + \mathbf{YX}). \tag{5.42}$$

Evaluation of $\bar{\mathbf{D}}^*$ via eq. (5.40) requires knowledge of $\mathbf{B}(i)$ [as well as of $P_0^\infty(i)$].

Additional computational simplifications of eq. (5.40) are readily effected. Similar to Adler & Brenner (1984b), we identify the terms appearing in the summation (5.41) for $\mathbf{E}$ as being the negative of the RHS of eq. (5.27) multiplied by $\mathbf{B}(i)$. Consequently, the expression for $\mathbf{E}$ may be reformulated upon multiplying eq. (5.27) by $\mathbf{B}(i)$, summing over $i \in V\Gamma_l$, and using eqs. (5.10) and (5.35), so as to eventually obtain

$$\mathbf{E} = \sum_{\substack{j\in E\Gamma_l \\ j\in\Omega^+}} d(j) P_0^\infty(i)\, \mathbf{B}(i)\mathbf{b}(j) - \left[c(j) + d(j) \right] P_0^\infty(i')\, \mathbf{B}(i')\, \mathbf{b}(j). \tag{5.43}$$

To effect further simplifications, multiply eq. (5.17) by $\mathbf{B}(i)\mathbf{B}(i)$, and sum over $i \in V\Gamma_l$, using eq. (5.10), to obtain

$$\sum_{\substack{j\in E\Gamma_l \\ j\in\Omega^+}} \left\{ \left[c(j) + d(j) \right] P_0^\infty(i') - d(j) P_0^\infty(i) \right\} \left[\mathbf{B}(i)\mathbf{B}(i) - \mathbf{B}(i')\mathbf{B}(i') \right] = \mathbf{0}. \tag{5.44}$$

Writing twice the symmetric part of $\mathbf{E}$ using eq. (5.43), and adding eq. (5.44), finally yields

$$2\,\mathrm{sym}(\mathbf{E}) = \sum_{\substack{j\in E\Gamma_l \\ j\in\Omega^+}} \left\{c(j)P_0^\infty\left(i'\right) + d(j)\left[P_0^\infty\left(i'\right) + P_0^\infty\left(i\right)\right]\right\}\mathbf{b}\left(j\right)\mathbf{b}(j). \tag{5.45}$$

To arrive at a canonical form for ultimately calculating the dispersivity dyadic, define the edge-based vector,

$$\tilde{\mathbf{b}}(j) \stackrel{\text{def.}}{=} \mathbf{R}(j) - \mathbf{b}(j), \tag{5.46}$$

and substitute eq. (5.45) into eq. (5.40), thereby obtaining

$$\bar{\mathbf{D}}^* = \frac{1}{2}\sum_{\substack{j\in E\Gamma_l \\ j\in\Omega^+}} \left\{c(j)P_0^\infty\left(i'\right) + d(j)\left[P_0^\infty\left(i'\right) + P_0^\infty\left(i\right)\right]\right\}\tilde{\mathbf{b}}(j)\tilde{\mathbf{b}}(j). \tag{5.47}$$

The preceding generic dispersivity formula properly reduces to the prior result of Adler & Brenner (1984b) upon setting $d(j) = 0\ \forall j$ and $P_0^\infty(i) = \tau_0^{-1}$. Equation (5.47) represents the fundamental paradigm whereby $\bar{\mathbf{D}}^*$ can be calculated from the prescribed discrete l-scale data.

5.4 The "Simple" Network

The final section of this chapter illustrates the usefulness of the present discrete theory in computing mean solute transport rates for a "simple" network. By "simple" is meant that only one intersection (albeit, perhaps, of multiple channels) is present within the repetitive unit cell. Figure 5-1 depicts such a network, wherein the apparent complexity of the medium serves to underscore potential difficulties that would be encountered in the application of continuous Taylor-Aris dispersion theory. Numerous microfluidic devices exist whose geometries are adequately captured by this simple network model, including both micropatterned vector chromatography chips (Chou *et al.* 1999, 2000) and entropic

trapping devices (Han & Craighead 2000).[4] Explicitly, the vector chromatography chips produced by Austin and coworkers (Chou *et al.* 1999, 2000) are comprised of a rectangular array of solid (rounded) rectangular obstacles, with solute transport occurring within the solvent-filled interstices between obstacles. In effect, our analysis of such devices in Chapter 9 is equipollent with the present simple network theory, in which the unit cell consists of but a single intersection connecting a narrow channel, oriented in the y-direction, to a wider channel, oriented orthogonally in the x-direction.

Significant reductions in the computational scheme are immediately effected in the "simple" network limit. Since the unit cell is comprised of but a single intersection, the unconditional probability density assumes the form $P_0^\infty = \tau_0^{-1}$, wherein τ_0 is the total volume of the channels and intersections contained within the boundaries of the unit cell. Moreover, calculation of the dispersivity is vastly simplified by noting that $\mathbf{b} = \mathbf{0}$, owing to the fact that every edge on the local graph is a loop. Armed with the latter data, the canonical expressions (5.25) and (5.47) reduce simply to the respective forms

$$\bar{\mathbf{U}}^* = \tau_0^{-1} \sum_{\substack{j \in E\Gamma_l \\ j \in \Omega^+}} c(j)\mathbf{R}(j), \tag{5.48}$$

$$\bar{\mathbf{D}}^* = \frac{1}{2\tau_0} \sum_{\substack{j \in E\Gamma_l \\ j \in \Omega^+}} \left[c(j) + 2d(j)\right] \mathbf{R}(j)\mathbf{R}(j). \tag{5.49}$$

The latter pair of formulae render transparent several fundamental properties of the simple network. The $\mathcal{I}$-space uniformity of the network reduces the mean velocity vector to a sum of purely convective contributions. In the network-level description of the periodic geometry, diffusive contributions to the mean velocity arise from nodal differences in probability density, rather than any finer-scale $\mathbf{R}$-space gradients — the former vanishing within the single node simple network. Rather, the diffusional transport processes occurring in the network description are manifested in the dispersivity dyadic.

[4] The use of the simple network theory for the analysis of these specific devices is deferred to Chapters 9 and 10.

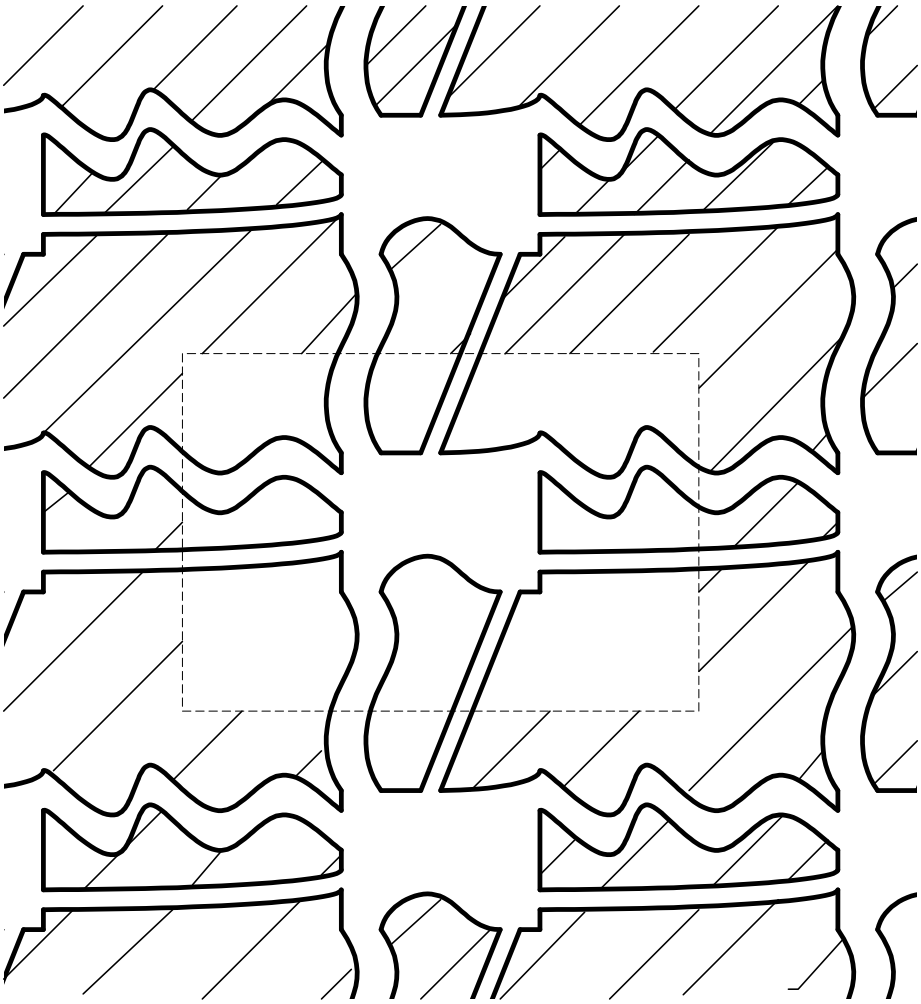

Figure 5-1: Schematic of a simple network in which the repetitive unit cell, denoted by the dashed lines, consists of a number of channels exiting and entering a single intersection. Such networks result in major simplifications of the discrete Taylor-Aris dispersion analysis scheme.

As is readily identified via eq. (5.49), dispersion within the simple network arises from two fundamental sources: (i) a contribution $d(j)\mathbf{R}(j)\mathbf{R}(j)$, representing dispersive processes occurring within the channels; and (ii) a contribution $c(j)\mathbf{R}(j)\mathbf{R}(j)$, representing the mechanical dispersion caused by the random residence times spent by a particle within the channel intersection domain before exiting the latter and entering an abutting channel.

These simple network results furnish significant insights into the mean solute transport and dispersion rates arising in such media. As such, they will prove useful in subsequent applications of our theory to the generalized Taylor-Aris dispersion phenomena occurring on chip-based microfluidic devices, whose details will be discussed in Part II.

Chapter 6

Method of Moments: Reactive Transport

6.1 Local Moments

In order to ultimately arrive at the desired paradigm for computing the macrotransport parameters $\bar{K}^*$, $\bar{\mathbf{U}}^*$ and $\bar{\mathbf{D}}^*$, the generalized moment scheme proposed by Dungan *et al.* (1990) will be adapted in a graphical manner similar to Chapter 5 to homogenize the master equation (4.10) governing reactive solute transport on the graph. In this context, define the "*non-reactive*" solute probability density,[1]

$$P\left(\mathbf{I}, i, t \,|\, i_0\right) \stackrel{\text{def.}}{=} \frac{\exp\left(\bar{K}t\right)}{A(i_0)} P_r\left(\mathbf{I}, i, t \,|\, i_0\right), \tag{6.1}$$

where the time- and position-independent reaction velocity constant $\bar{K}$ (defined globally on the network scale) and vertex field $A\left(i\right)$ (defined locally on the unit-cell scale) will be determined later. The master equation governing P is derived by substituting the

[1] We use the notation $P\left(\mathbf{I}, i, t \,|\, i_0\right)$ to indicate that this change of variables will permit a moment scheme similar to that employed in the previous chapter.

definition (6.1) into eq. (4.10) to obtain

$$\begin{aligned} v(i)\frac{dP(\mathbf{I},i,t\,|\,i_0)}{dt} =& \frac{\delta_{\mathbf{I},\mathbf{0}}\delta_{i,i_0}\delta(t)}{A(i_0)} + \left[\bar{K}-k(i)\right]v(i)P\left(\mathbf{I},i,t\,|\,i_0\right) + \\ &+ \sum_{\substack{j\in\Omega^+(i)\\ j=\{i',i\}}} c(j)P(\mathbf{I}',i',t\,|\,i_0) + d(j)\left[\begin{array}{c} P(\mathbf{I}',i',t\,|\,i_0)- \\ -P(\mathbf{I},i,t\,|\,i_0)\end{array}\right] - \\ &- \sum_{\substack{j\in\Omega^-\\ j=\{i,i'\}}} c(j)P(\mathbf{I},i,t\,|\,i_0) + d(j)\left[\begin{array}{c} P(\mathbf{I},i,t\,|\,i_0)- \\ -P(\mathbf{I}',i',t\,|\,i_0)\end{array}\right]. \end{aligned} \tag{6.2}$$

Define the non-reactive local moment as the m-adic,

$$\mathbf{P}_m(i,t\,|\,i_0) \stackrel{\text{def.}}{=} \sum_{\mathbf{I}} \mathbf{R}_{\mathbf{I}}^m P\left(\mathbf{I},i,t\,|\,i_0\right). \tag{6.3}$$

The equation governing the local moments $\mathbf{P}_m(i)$ (with time and the initial condition suppressed therein for notational simplicity) is obtained upon multiplying eq. (6.2) by $\mathbf{R}_{\mathbf{I}}^m$ and summing over $\mathbf{I}$, thereby obtaining

$$v(i)\frac{d\mathbf{P}_m(i)}{dt} = \frac{\delta_{m,0}\delta_{i,i_0}\delta(t)}{A(i_0)} + L\left[\mathbf{P}_m\left(i\right)\right] + \Gamma_m(i). \tag{6.4}$$

In the latter, the vertex operator L operating on an arbitrary vertex field $\psi(i)$ is defined as

$$\begin{aligned} L\left[\psi(i)\right] \stackrel{\text{def.}}{=}& \sum_{\substack{j\in\Omega^+(i)\\ j=\{i',i\}}} c(j)\psi\left(i'\right) + d(j)\left[\psi(i')-\psi(i)\right] - \\ &- \sum_{\substack{j\in\Omega^-\\ j=\{i,i'\}}} c(j)\psi(i) + d(j)\left[\psi(i)-\psi(i')\right] + \left[\bar{K}-k(i)\right]v(i)\psi(i). \end{aligned} \tag{6.5}$$

The first few m-adics $\Gamma_m(i)$ appearing in eq. (6.4) possess the respective forms

$$\Gamma_0(i) = 0, \tag{6.6}$$

$$\Gamma_1(i) = \sum_{\substack{j\in\Omega^+(i)\\ j=\{i',i\}}} [c(j)+d(j)]\,\mathbf{R}\,(j)\,P_0(i') - \sum_{\substack{j\in\Omega^-\\ j=\{i,i'\}}} d(j)\mathbf{R}(j)P_0(i'), \tag{6.7}$$

$$\Gamma_2(i) = 2\ \mathrm{sym}\left\{ \begin{array}{l} \displaystyle\sum_{\substack{j\in\Omega^+(i)\\ j=\{i',i\}}} [c(j)+d(j)]\left[\frac{1}{2}\mathbf{R}\,(j)\,\mathbf{R}\,(j)\,P_0(i') + \mathbf{R}\,(j)\,\mathbf{P}_1(i')\right] + \\ \qquad \displaystyle\sum_{\substack{j\in\Omega^-\\ j=\{i,i'\}}} d(j)\left[\frac{1}{2}\mathbf{R}\,(j)\,\mathbf{R}\,(j)\,P_0(i') - \mathbf{R}\,(j)\,\mathbf{P}_1(i')\right] \end{array} \right\}, \tag{6.8}$$

where the symmetry operator was defined previously by eq. (5.42).

6.2 Global Moments

Define the respective unweighted and weighted *non-reactive* global moments,

$$\mathbf{M}'_m\,(t\,|\,i_0) \stackrel{\mathrm{def.}}{=} \sum_{i\in\Gamma_l} v(i)\mathbf{P}_m(i,t\,|\,i_0), \tag{6.9}$$

$$\mathbf{M}_m\,(t\,|\,i_0) \stackrel{\mathrm{def.}}{=} \sum_{i\in\Gamma_l} v(i)A(i)\mathbf{P}_m(i,t\,|\,i_0). \tag{6.10}$$

In the latter, the node-based field $A(i)$ [cf. eq. (6.1)] arises from the necessity for introducing into macrotransport theory a fictitious initial condition (Dungan *et al.* 1990), whose significance and defining equation will be established shortly. It is possible to choose the constant $\bar{K}$ appearing in the definition (6.1) such that M'_0 is conserved for sufficiently long-times (Shapiro & Brenner 1987). However, transients arising from the initial placement, i_0, of the particle (within cell $\mathbf{I}_0 = \mathbf{0}$) persist for long times, longer than the time required for the asymptotic theory of Taylor & Aris to constitute an accurate global representation of the transport phenomena. This residual transient thereby impacts nontrivially upon the network-scale transport processes (Batycky *et al.* 1996). To

properly correct for such transients, as was done in the original derivation of Dungan *et al.* (1990), we will derive a difference equation for the fictitious initial condition $A(i)$ (in place of the literal initial condition). This scheme insures that M_0 too is conserved for all times, thereby allowing a conventional Taylor-Aris moment analysis (Dungan *et al.* 1990), involving the use of weighted moments. It will be shown that the rates of change of the weighted and unweighted moments differ only by exponentially small temporal terms, at least for sufficiently long times. As a consequence, the distinction between the two types of global moments, $\mathbf{M}'_m$ and $\mathbf{M}_m$, defined above proves irrelevant in the final macrotransport results.

The differential equation governing M_0 is derived by forming the product of $A(i)$ and eq. (6.4) [with $m = 0$ and eq. (6.6)], and summing over $i \in \Gamma_l$ to obtain

$$\begin{aligned}\frac{dM_0}{dt} =& \delta(t) + \sum_{i\in\Gamma_l} \left[\bar{K} - k(i)\right] v(i)A(i)P_0(i) + \\ &+ \sum_{\substack{j\in E\Gamma_l \\ j\in\Omega^+}} c(j)A(i)P_0(i') + d(j)A(i)\left[P_0\left(i'\right) - P_0(i)\right] - \\ &- \sum_{\substack{j\in E\Gamma_l \\ j\in\Omega^-}} c(j)A(i)P_0(i) + d(j)A(i)\left[P_0(i) - P_0\left(i'\right)\right]. \end{aligned} \tag{6.11}$$

Here and hereafter, the following compact summation notation will again be employed:

$$\sum_{\substack{j\in E\Gamma_l \\ j\in\Omega^+}} \overset{\text{def.}}{=} \sum_{i\in V\Gamma_l} \sum_{\substack{j\in\Omega^+(i) \\ j=\{i',i\}}}, \qquad \sum_{\substack{j\in E\Gamma_l \\ j\in\Omega^-}} \overset{\text{def.}}{=} \sum_{i\in V\Gamma_l} \sum_{\substack{j\in\Omega^-(i) \\ j=\{i,i'\}}}. \tag{6.12}$$

The strong connectivity of the graph furnishes the pair of identities,

$$\sum_{\substack{j\in E\Gamma_l \\ j\in\Omega^+}} \epsilon(j)\phi(i') = \sum_{\substack{j\in E\Gamma_l \\ j\in\Omega^-}} \epsilon(j)\phi(i), \tag{6.13}$$

$$\sum_{\substack{j\in E\Gamma_l \\ j\in\Omega^+}} \epsilon(j)\phi_1(i')\phi_2\left(i\right) = \sum_{\substack{j\in E\Gamma_l \\ j\in\Omega^-}} \epsilon(j)\phi_1(i)\phi_2\left(i'\right), \tag{6.14}$$

where $\phi_k(i)$ and $\epsilon(j)$ are, respectively, node- and edge-based quantities. With use of these identities, eq. (6.11) may be reformulated as

$$\frac{dM_0}{dt} = \delta(t) + \sum_{\substack{j\in E\Gamma_l \\ j\in\Omega^+}} P_0(i)d(j)\left[A(i') - A(i)\right] + \sum_{i\in\Gamma_l}\left[\bar{K} - k(i)\right]v(i)A(i)P_0(i) + \\ + \sum_{\substack{j\in E\Gamma_l \\ j\in\Omega^-}} P_0(i)\left[c(j) + d(j)\right]\left[A(i') - A(i)\right]. \tag{6.15}$$

In order that M_0 be conserved for all times, the summations appearing on the right-hand side of eq. (6.15) must vanish; explicitly,

$$\sum_{\substack{j\in\Omega^+(i) \\ j=\{i',i\}}} d(j)\left[A(i') - A(i)\right] + \sum_{\substack{j\in\Omega^-(i) \\ j=\{i,i'\}}}\left[c(j) + d(j)\right]\left[A(i') - A(i)\right] + \\ + \left[\bar{K} - k(i)\right]v(i)A(i) = 0. \tag{6.16}$$

Equation (6.16), governing $A(i)$, may be restated in compact form as

$$\left\{\mathbf{k} - \mathbf{v}^{-1}\cdot\left[\mathbf{D}\cdot\mathbf{d} - \Pi^{(-)}\cdot\mathbf{c}\right]\cdot\mathbf{D}^{\dagger}\right\}\cdot\mathbf{A} = \bar{K}\mathbf{A}, \tag{6.17}$$

where $\mathbf{A}$ is an $n\times 1$ row vector whose elements are the fictitious initial nodal conditions embodied in $A(i)$ $(i = 1, 2, \ldots, n)$. The convection and diffusion matrices, $\mathbf{c}$ and $\mathbf{d}$, were defined previously in eq. (5.19). The volume matrix, $\mathbf{v}$,[2] and reaction matrix, $\mathbf{k}$, are defined as

$$\mathbf{v} \overset{\text{def.}}{=} v(i)\delta_{i,j}, \quad \mathbf{k} \overset{\text{def.}}{=} k(i)\delta_{i,j}. \tag{6.18}$$

Equation (6.17) constitutes an eigenvalue problem for simultaneously computing the eigenvalues $\bar{K}$ and eigenvectors $A(i)$. The scheme for identifying the one, physically relevant eigenvalue $\bar{K}$, as well as the required normalization of the corresponding physically

[2]It will be clear from context whether the symbol $\mathbf{v}$ refers to the volume matrix (6.18) or the volume vector (5.22).

relevant eigenvector $\mathbf{A}$, will be specified in the following section.

With use of eq. (6.16), temporal integration of (6.15) demonstrates that

$$M_0 = \begin{cases} 0, & t < 0, \\ 1, & t \geq 0, \end{cases} \tag{6.19}$$

whereupon M_0 is indeed seen to be conserved for all times (independently of i_0). A generic equation governing the weighted global moments may also be derived with use of eq. (6.16). To do so, multiply (6.4) by $A(i)$, sum over $i \in \Gamma_l$, and use eqs. (6.13) and (6.14), thereby obtaining the expression

$$\frac{d\mathbf{M}_m}{dt} = \delta_{m,0}\delta(t) + \sum_{i \in \Gamma_l} A(i)\Gamma_m(i). \tag{6.20}$$

6.3 Asymptotic, Long-Time Limits

The following section furnishes the asymptotic, long-time limits of the first few local and global moments of the non-reactive probability density. By "long-time" is meant that the residence time, t_R, of the solute in the network is long compared with the diffusion time scale; that is $t_R \gg l^2/D_m$, where l denotes a characteristic linear dimension of the unit cell [typically the magnitude of a macroscopic jump vector, $|\mathbf{R}(j)|$] and D_m is the molecular diffusivity of the solute (Brenner & Edwards 1993). A further criterion imposed upon the definition of long-time behavior will be established later [cf. eq. (6.24)].

6.3.1 Zeroth-Order Moments

For sufficiently long times, the zeroth-order local moment (6.3) assumes the asymptotic form

$$P_0(i, t \,|\, i_0) \approx P_0^{\infty}(i) + \exp, \tag{6.21}$$

for all i_0, where "exp" denotes temporal terms that are exponentially small for sufficiently long times. The asymptotic probability density, $P_0^\infty(i)$, is independent of time as well as of the initial local position, i_0. The validity of eq. (6.21) has been established by Shapiro & Brenner (1986, 1988) via the use of eigenfunction expansions.

Substitute eq. (6.21) into eq. (6.4), set $m = 0$, and use eq. (6.6) to obtain the difference equation governing $P_0^\infty(i)$, namely

$$L\left[P_0^\infty(i)\right] = 0. \tag{6.22}$$

The latter may be recast into the compact matrix form,[3]

$$\left\{\mathbf{k} - \mathbf{v}^{-1}\cdot\mathbf{D}\cdot\left[(\mathbf{c}+\mathbf{d})\cdot\left(\Pi^{(-)}\right)^\dagger - \mathbf{d}\cdot\left(\mathbf{\Pi}^{(+)}\right)^\dagger\right]\right\}\cdot\mathbf{P} = \bar{K}\mathbf{P}, \tag{6.23}$$

where $\mathbf{P}$ is the $n\times 1$ row vector composed of the asymptotic probability densities, $P_0^\infty(i)$ $(i = 1, 2, \ldots, n)$. Similar to eq. (6.17), eq. (6.23) constitutes an eigenvalue problem posed for $P_0^\infty(i)$ and $\bar{K}$. The eigenvalue with the smallest real part (corresponding to the slowest decaying mode of the full solution) is identified as the effective reaction rate $\bar{K}^*$ (Dungan *et al.* 1990, Shapiro & Brenner 1986, 1988).[4] For all physical circumstances, the eigenvalue possessing the smallest real part is pure real (Shapiro & Brenner 1986, 1988). Moreover, the solution of this eigenvalue problem furnishes a second criterion quantifying what is meant by the phrase "long-time behavior." Upon denoting the second smallest eigenvalue of eq. (6.23) as $\bar{K}_1$, we require the residence time to satisfy the inequality

$$t_R \gg \left(\bar{K}^*\right)^{-1} - \bar{K}_1^{-1}, \tag{6.24}$$

[3]The cocycle space is not invoked for computing the vector $\mathbf{P}$ in the reactive case since the eigenvalue problem (6.23) is specified completely.

[4]By way of example, Batycky *et al.* (1996) illustrate the dominance of the slowest decaying mode by comparing the (asymptotic) macrotransport solution for a non-adiabatic unsteady heat transfer process with its exact trigonometric function expansion. Moreover, their analysis clearly illustrates the necessity for incorporating the notion of a fictitious initial condition into effective-medium models, such as in the present macrotransport model.

whereupon the effective transport process is dominated by the eigenvalue with the smallest real part, $\bar{K}^*$.

As shown below, the eigenvalue problems posed for $P_0^\infty(i)$ (6.22) and $A(i)$ (6.16) are adjoint. Thus, let $\bar{K}_P$ and $\bar{K}_A$, respectively, be eigenvalues of eqs. (6.22) and (6.16). Upon multiplying eq. (6.16) by $P_0^\infty(i)$, eq. (6.22) by $A(i)$, and summing both results over $i \in \Gamma_l$, we see that $\bar{K}_P = \bar{K}_A$. Consequently, the appropriate fictitious initial condition $A(i)$ is the eigenvector of eq. (6.16) corresponding to the eigenvalue $\bar{K} = \bar{K}^*$.

The eigenvalue problems governing $P_0^\infty(i)$ and $A(i)$ only specify each of these two fields (eigenvectors) to within arbitrary, constant multipliers. These multipliers may be uniquely determined by applying the normalization conditions (Dungan *et al.* 1990), namely

$$\sum_{i\in\Gamma_l} v(i)P_0^\infty(i) = 1, \tag{6.25}$$

$$\sum_{i\in\Gamma_l} v(i)A(i)P_0^\infty(i) = 1. \tag{6.26}$$

To verify that the weighted and unweighted zeroth-order global moments are indistinguishable at long times, substitute the asymptotic solution (6.21) into eq. (6.9), together with the normalization condition (6.25). This demonstrates that our choice of $\bar{K}$ and $A(i_0)$ conserves M_0' for long times, at least to within exponentially small terms; explicitly,

$$M_0' \approx 1 + \exp, \tag{6.27}$$

for all i_0. Moreover, the ability to formulate consistent results for M_0, eq. (6.19), and M_0', eq. (6.27), verifies the change in variables (6.1), thereby confirming our prior assertion that the solute is eventually depleted completely at each and every node, and hence throughout the network as a whole.

6.3.2 First-Order Moments

Mean Velocity Vector $\bar{\mathbf{U}}^*$

The mean velocity of the reactive tracer through the network is determined from knowledge of the asymptotic limit of the rate of growth of the first global moment via the generic expression (Dungan *et al.* 1990),

$$\bar{\mathbf{U}}^* = \lim_{t\to\infty} \frac{d\mathbf{M}_1}{dt}. \tag{6.28}$$

Substitute eq. (6.7) into eq. (6.20), set $m = 1$, and use eqs. (6.14) and (6.21) to obtain

$$\bar{\mathbf{U}}^* = \sum_{\substack{j\in E\Gamma_l \\ j\in\Omega^+}} c(j)\mathbf{R}(j)\, A(i)P_0^\infty(i') + d(j)\mathbf{R}(j)\left[A(i)P_0^\infty(i') - A(i')P_0^\infty(i)\right]. \tag{6.29}$$

Derivation of the B-equation

Subject to *a posteriori* verification, assume the following trial solution for the first-order local moment:

$$\mathbf{P}_1(i) \approx P_0^\infty(i)\left[\bar{\mathbf{U}}^* t + \mathbf{B}(i)\right] + \exp, \tag{6.30}$$

where $\mathbf{B}(i)$ is a node-based field to be determined. Substitution of eq. (6.30) into eq. (6.10), together with the choice $m = 1$, furnishes the weighted first-order global moment,

$$\mathbf{M}_1 \approx \bar{\mathbf{U}}^* t + \sum_{i\in\Gamma_l} v(i)A(i)P_0^\infty(i)\mathbf{B}(i) + \exp. \tag{6.31}$$

The difference equation governing $\mathbf{B}(i)$ is derived by substituting the trial solution (6.30) into eq. (6.4), setting $m = 1$, and using eq. (6.7). Elimination of time-dependent terms via eq. (6.22), and reactive terms via the product of $\mathbf{B}(i)$ with eq. (6.22), eventually

yields

$$\sum_{\substack{j\in\Omega^+(i)\\ j=\{i',i\}}} [c(j)+d(j)]\, P_0^\infty(i')\,[\mathbf{B}(i')-\mathbf{B}(i)] - \\ -\sum_{\substack{j\in\Omega^-(i)\\ j=\{i,i'\}}} d(j)P_0^\infty(i')\,[\mathbf{B}(i)-\mathbf{B}(i')] = v(i)P_0^\infty(i)\bar{\mathbf{U}}^*-\alpha(i), \tag{6.32}$$

with $\alpha(i)$ the node-based vector,

$$\alpha(i) = \sum_{\substack{j\in\Omega^+(i)\\ j=\{i',i\}}} [c(j)+d(j)]\,\mathbf{R}\,(j)\,P_0^\infty(i') - \sum_{\substack{j\in\Omega^-(i)\\ j=\{i,i'\}}} d(j)\mathbf{R}(j)P_0^\infty(i'). \tag{6.33}$$

Equation (6.32) defines the $\mathbf{B}$ field only to within an arbitrary additive constant vector (Brenner & Edwards 1993), whose value ultimately proves irrelevant when computing the dispersivity [cf. eq. (6.52)]. Consequently, the resulting degree of freedom may be utilized so as to conveniently allow an arbitrary reference node, say i^*, to be chosen such that $\mathbf{B}\,(i^*)=\mathbf{0}$. With the latter specification, the $(n-1)$ equations generated by (6.32) for $i\neq i^*$ suffice to determine the remaining vectors $\mathbf{B}\,(i)$.[5]

Subsequent calculations [cf. eq. (6.52)] necessitate introducing the edge-based vector field,

$$\mathbf{b}(j) \stackrel{\text{def.}}{=} \mathbf{B}(i)-\mathbf{B}(i'), \quad \left\{j\in\Omega^+(i)\right\}, \tag{6.34}$$

defined such that edge j has its initial vertex at i' and its terminal vertex at i. The m vectors, $\mathbf{b}(j)$, may be computed from the solution of the $(n-1)$ equations generated by eq. (6.32), together with the m definitions from eq. (6.34). Alternatively, a difference

[5] In the non-reactive network theory of Chapter 5, the cocycle space was invoked to provide a formal mechanism for choosing the reference node i^*. While this technique remains valid for the present reactive case, subsequent simplifications of the $\mathbf{B}$-equations will render the utility of such a formalism moot.

equation may be derived for $\mathbf{b}\,(j)$ by substituting eq. (6.34) into eq. (6.32), so as to obtain

$$\sum_{\substack{j\in\Omega^-(i)\\ j=\{i,i'\}}} d(j)P_0^\infty(i')\mathbf{b}(j) - \sum_{\substack{j\in\Omega^+(i)\\ j=\{i',i\}}} \left[c(j)+d(j)\right] P_0^\infty(i')\mathbf{b}(j) = v(i)P_0^\infty(i)\bar{\mathbf{U}}^* - \alpha(i). \quad (6.35)$$

However, the n equations contained in eq. (6.35) generally prove insufficient to solve for all m vectors $\mathbf{b}(j)$, since, for all but the most trivial networks, $m > n$. Consequently, it is necessary to augment the (non-square) coefficient matrix by noting that the sum of the $\mathbf{b}$ vectors vanishes along any cycle of the graph,

$$\sum_{j\in\text{cycle}} \mathbf{b}(j) = \mathbf{0}. \quad (6.36)$$

Superposition of the n equations provided by eq. (6.35), together with the $(m-n)$ independent cycles chosen from eq. (6.36), completely specifies the $\mathbf{b}$ vectors.

To reformulate the $\mathbf{B}$-equations in matrix form, define the pair of $n \times m$ conditioned connectivity matrices,

$$\tilde{\mathbf{\Pi}}^{(+)}_{ij} \overset{\text{def.}}{=} \begin{cases} P_0^\infty(i') & \text{if edge } j \text{ is directed from } i' \text{ to } i, \\ 0 & \text{otherwise;} \end{cases} \quad (6.37)$$

$$\tilde{\mathbf{\Pi}}^{(-)}_{ij} \overset{\text{def.}}{=} \begin{cases} P_0^\infty(i') & \text{if edge } j \text{ is directed from } i \text{ to } i', \\ 0 & \text{otherwise.} \end{cases} \quad (6.38)$$

With use of the latter, the (non-square) equation set (6.35) governing $\mathbf{b}$ adopts the form

$$\left[\tilde{\mathbf{\Pi}}^{(-)}\cdot\mathbf{d} - \tilde{\mathbf{\Pi}}^{(+)}\cdot(\mathbf{c}+\mathbf{d})\right]\cdot\mathbf{b} = \mathbf{v}\cdot\mathbf{P}\cdot\bar{\mathbf{U}}^* - \left[\tilde{\mathbf{\Pi}}^{(+)}\cdot(\mathbf{c}+\mathbf{d}) - \tilde{\mathbf{\Pi}}^{(-)}\cdot\mathbf{d}\right]\cdot\mathbf{R}. \quad (6.39)$$

Conversion between $\mathbf{b}$ and $\mathbf{B}$ is accomplished via the transformation

$$\mathbf{b} = \mathbf{D}^\dagger\cdot\mathbf{B}, \quad (6.40)$$

whereupon eq. (6.32) adopts the matrix form,

$$\left[\tilde{\mathbf{\Pi}}^{(-)} \cdot \mathbf{d} - \tilde{\mathbf{\Pi}}^{(+)} \cdot (\mathbf{c} + \mathbf{d})\right] \cdot \mathbf{D}^{\dagger} \cdot \mathbf{B} = \mathbf{v} \cdot \mathbf{P} \cdot \bar{\mathbf{U}}^{*} - \left[\tilde{\mathbf{\Pi}}^{(+)} \cdot (\mathbf{c} + \mathbf{d}) - \tilde{\mathbf{\Pi}}^{(-)} \cdot \mathbf{d}\right] \cdot \mathbf{R}. \quad (6.41)$$

The time-independence of eqs. (6.32) and (6.35) confirms, *a posteriori*, the assumed trial solution (6.30) for $\mathbf{P}_1$ as well as the resulting expression (6.31) for $\mathbf{M}_1$. Consequently, the unweighted first-order global moment may be computed from eq. (6.9) (with $m = 1$) together with eqs. (6.25) and (6.30), yielding

$$\mathbf{M}_1' \approx \bar{\mathbf{U}}^{*} t + \bar{\mathbf{B}} + \text{exp}, \quad (6.42)$$

where the time- and position-independent vector $\bar{\mathbf{B}}$ is of the form

$$\bar{\mathbf{B}} = \sum_{i \in \Gamma_l} v(i) P_0^{\infty}(i) \mathbf{B}(i). \quad (6.43)$$

Differentiation of eqs. (6.31) and (6.42) with respect to time reveals that the temporal rates of change of $\mathbf{M}_1$ and $\mathbf{M}_1'$ differ only by exponentially small terms at long times.

6.3.3 Second-Order Moments

The difference equation governing the weighted second-order global moment, $\mathbf{M}_2$, is derived from eq. (6.20) with $m = 2$. Making use of eqs. (6.8), (6.14), (6.21), (6.29) and (6.30), thereby obtains

$$\frac{d\mathbf{M}_2}{dt} \approx 2\bar{\mathbf{U}}^{*}\bar{\mathbf{U}}^{*} t + 2 \text{ sym} \left\{ \sum_{\substack{j \in E\Gamma_l \\ j \in \Omega^{+}}} [c(j) + d(j)] A(i) P_0^{\infty}(i') \begin{bmatrix} \frac{1}{2}\mathbf{R}(j)\mathbf{R}(j) + \\ +\mathbf{R}(j)\mathbf{B}(i') \end{bmatrix} \right\} +$$
$$+ 2 \text{ sym} \left\{ \sum_{\substack{j \in E\Gamma_l \\ j \in \Omega^{+}}} \left\{ d(j) A(i') P_0^{\infty}(i) \begin{bmatrix} \frac{1}{2}\mathbf{R}(j)\mathbf{R}(j) - \\ -\mathbf{R}(j)\mathbf{B}(i) \end{bmatrix} \right\} \right\} + \text{exp}. \quad (6.44)$$

Subject to *a posteriori* verification, assume a trial solution for the second-order local moment, $\mathbf{P}_2$, of the form[6]

$$\mathbf{P}_2(i) \approx P_0^{\infty}(i) \left\{ \bar{\mathbf{U}}^* \bar{\mathbf{U}}^* t^2 + 2 \text{ sym} \left[\bar{\mathbf{U}}^* \mathbf{B}(i) \right] t + 2 \bar{\mathbf{D}}^* t + \mathbf{H}(i) \right\} + \text{exp}, \tag{6.45}$$

with the constant dyadic $\bar{\mathbf{D}}^*$ and dyadic field $\mathbf{H}(i)$ to be determined forthwith.

To compute $\bar{\mathbf{D}}^*$, form the weighted second-order global moment from eqs. (6.10), with order $m = 2$, and (6.45), and differentiate the resulting expression with respect to time, so as to obtain

$$\frac{d\mathbf{M}_2}{dt} \approx 2 \bar{\mathbf{U}}^* \bar{\mathbf{U}}^* t + 2 \bar{\mathbf{D}}^* + 2 \text{ sym} \sum_{i \in \Gamma_l} v(i) P_0^{\infty}(i) A(i) \bar{\mathbf{U}}^* \mathbf{B}(i) + \text{exp}. \tag{6.46}$$

The summation appearing in eq. (6.46) may be simplified by forming the product of eq. (6.32) with $A(i)\mathbf{B}(i)$, and subsequently summing the result over $i \in \Gamma_l$, thereby yielding

$$2 \text{ sym} \left[\sum_{i \in \Gamma_l} v(i) P_0^{\infty}(i) A(i) \bar{\mathbf{U}}^* \mathbf{B}(i) \right] = 2 \text{ sym} \left[\sum_{i \in \Gamma_l} \alpha(i) A(i) \mathbf{B}(i) \right] + 2 \text{ sym} \left(\mathbf{E} \right), \tag{6.47}$$

where $\mathbf{E}$ is the constant dyadic

$$\begin{aligned} \mathbf{E} = & \sum_{\substack{j \in E\Gamma_l \\ j \in \Omega^+}} \left[c(j) + d(j) \right] P_0^{\infty}(i') A(i) \mathbf{B}(i) \left[\mathbf{B}\left(i'\right) - \mathbf{B}(i) \right] - \\ & - \sum_{\substack{j \in E\Gamma_l \\ j \in \Omega^-}} d(j) P_0^{\infty}(i') A(i) \mathbf{B}(i) \left[\mathbf{B}(i) - \mathbf{B}(i') \right]. \end{aligned} \tag{6.48}$$

The dyadic $\mathbf{E}$ may itself be simplified upon multiplying eq. (6.22) by $A(i)\mathbf{B}(i)\mathbf{B}(i)$ and eq. (6.16) by $P_0^{\infty}(i)\mathbf{B}(i)\mathbf{B}(i)$, summing both results over $i \in \Gamma_l$ with use of the identity

[6]It is necessary to consider the local moment $\mathbf{P}_2$ in the reactive case (Shapiro & Brenner 1988) in order to show that the different global moments $\mathbf{M}_2$ and $\mathbf{M}_2^{'}$ only differ by exponentially small terms at long times. We did not consider $\mathbf{P}_2$ in the non-reactive case since, by definition, $\mathbf{M}_2 = \mathbf{M}_2^{'}$.

(6.14), and forming their difference, so as to obtain the expression

$$\sum_{\substack{j\in E\Gamma_l \\ j\in\Omega^+}} \left\{[c(j)+d(j)]\,A(i)P_0^\infty(i') - d(j)A(i')P_0^\infty(i)\right\}\left[\mathbf{B}(i)\mathbf{B}(i) - \mathbf{B}(i')\mathbf{B}(i')\right] = \mathbf{0}. \quad (6.49)$$

Upon adding the null result (6.49) to eq. (6.48), and using the definition (6.34), the symmetric portion of $\mathbf{E}$ is found to possess the form

$$2\ \mathrm{sym}\,(\mathbf{E}) = -\sum_{\substack{j\in E\Gamma_l \\ j\in\Omega^+}} \left\{[c(j)+d(j)]\,A(i)P_0^\infty(i') + d(j)A(i')P_0^\infty(i)\right\}\mathbf{b}(j)\mathbf{b}(j). \quad (6.50)$$

Equation (6.47) may be further simplified by using eq. (6.33) jointly with the identity (6.14) to show that

$$\sum_{i\in\Gamma_l}\alpha(i)A(i)\mathbf{B}(i) = \sum_{\substack{j\in E\Gamma_l \\ j\in\Omega^+}} \left\{ \begin{array}{c} [c(j)+d(j)]\,\mathbf{R}(j)A(i)P_0^\infty(i')\mathbf{B}(i) - \\ -d(j)\mathbf{R}(j)A(i')P_0^\infty(i)\mathbf{B}(i') \end{array} \right\}. \quad (6.51)$$

Upon comparing eq. (6.44) with our trial solution (6.46), and making use of eqs. (6.47), (6.50) and (6.51), as well as the identity (6.14), there results the expression

$$\bar{\mathbf{D}}^* = \frac{1}{2}\sum_{\substack{j\in E\Gamma_l \\ j\in\Omega^+}} \left\{c(j)A(i)P_0^\infty(i') + d(j)\left[A(i)P_0^\infty(i') + A(i')P_0^\infty(i)\right]\right\}\tilde{\mathbf{b}}(j)\tilde{\mathbf{b}}(j), \quad (6.52)$$

where the vector $\tilde{\mathbf{b}}(j)$ is defined as it was in the non-reactive case,

$$\tilde{\mathbf{b}}(j) \stackrel{\text{def.}}{=} \mathbf{R}(j) - \mathbf{b}(j). \quad (6.53)$$

Moreover, we see that $\bar{\mathbf{D}}^*$ represents the solute dispersivity dyadic, inasmuch as $\bar{\mathbf{D}}^*$ may also calculated from its definition (Dungan *et al.* 1990), namely

$$\bar{\mathbf{D}}^* = \frac{1}{2}\lim_{t\to\infty}\frac{d}{dt}\left(\mathbf{M}_2 - \mathbf{M}_1\mathbf{M}_1\right). \quad (6.54)$$

The latter is seen to accord with the result (6.52) upon use of eqs. (6.31) and (6.46).

Equation (6.52) enforces an equality between the trial solution (6.46) and its derived formula (6.44). Consequently, *a posteriori* verification of the trial solution (6.45) is completed by deriving a solvable difference equation for $\mathbf{H}(i)$ (Shapiro & Brenner 1988). To do so, substitute the trial solution (6.45) into eq. (6.4), with $m = 2$, and use eq. (6.8). Removing the time-dependent terms via eqs. (6.22) and (6.32), and subsequently substituting for the reaction term upon multiplying eq. (6.22) by $\mathbf{H}(i)$, ultimately furnishes the governing equation for $\mathbf{H}(i)$, namely

$$\sum_{\substack{j\in\Omega^+(i)\\ j=\{i',i\}}} [c(j)+d(j)]\, P_0^\infty(i')\,[\mathbf{H}(i')-\mathbf{H}(i)] - \sum_{\substack{j\in\Omega^-(i)\\ j=\{i,i'\}}} d(j)P_0^\infty(i')\,[\mathbf{H}(i)-\mathbf{H}(i')] = \beta(i), \tag{6.55}$$

with $\beta(i)$ the symmetric forcing function

$$\beta(i) = 2\ \mathrm{sym}\left\{ \begin{array}{l} v(i)P_0^\infty(i)\left[\bar{\mathbf{U}}^*\mathbf{B}(i)+\bar{\mathbf{D}}^*\right] - \\ -\displaystyle\sum_{\substack{j\in\Omega^+(i)\\ j=\{i',i\}}} [c(j)+d(j)]\, P_0^\infty(i)\left[\frac{1}{2}\mathbf{R}(j)\mathbf{R}(j)+\mathbf{R}(j)\mathbf{B}(i')\right] - \\ -\displaystyle\sum_{\substack{j\in\Omega^-(i)\\ j=\{i,i'\}}} d(j)P_0^\infty(i')\left[\frac{1}{2}\mathbf{R}(j)\mathbf{R}(j)-\mathbf{R}(j)\mathbf{B}(i')\right] \end{array} \right\}. \tag{6.56}$$

Inasmuch as the structure of eq. (6.55) is identical to that of eq. (6.32), eq. (6.55) will possess a solution if eq. (6.32) itself possesses a solution. As was the case in the original development (Shapiro & Brenner 1987) of this moment technique, computing $\mathbf{H}$ proves unnecessary. Indeed, we have already derived formulas for all the relevant macrotransport parameters without prior knowledge of $\mathbf{H}$. Rather, the demonstrated existence of the latter time-independent, solvable equation (6.55) simply completes the *a posteriori* verification of eq. (6.45).

The latter verification permits computing $\mathbf{M}_2'$ by substituting eq. (6.45) into eq. (6.9),

choosing $m = 2$, and invoking eqs. (6.25) and (6.43). Thereby, one obtains

$$\mathbf{M}_2' \approx \bar{\mathbf{U}}^* \bar{\mathbf{U}}^* t^2 + 2 \text{ sym} \left(\bar{\mathbf{B}} \bar{\mathbf{U}}^* \right) t + 2 \bar{\mathbf{D}}^* t + \sum_{i \in \Gamma_l} v(i) P_0^{\infty}(i) \mathbf{H}(i) + \text{exp.} \tag{6.57}$$

Differentiation of the latter with respect to time, followed by subsequent comparison of the resulting expression with eq. (6.46), reveals that the time rates of change of $\mathbf{M}_2$ and $\mathbf{M}_2'$ differ only by exponentially small terms at long times.

Chapter 7

Recapitulation

This chapter presents a concise summary of the discrete macrotransport theory developed in Part I of this thesis. The particular forms of the governing equations and summations are chosen for their pedagogical value. Alternative forms of the equations, including their reformulation in compact matrix notation, may be found in the context of the derivations of the previous two chapters.

7.1 Non-Reactive Transport

Mean Solute Velocity Vector [eq. (5.25)]:

$$\bar{\mathbf{U}}^* = \sum_{\substack{j\in E\Gamma_l \\ j\in\Omega^+}} c(j)\mathbf{R}(j)P_0^\infty(i') + d(j)\mathbf{R}(j)\left[P_0^\infty(i') - P_0^\infty(i)\right]. \tag{7.1}$$

Dispersivity Dyadic [eq. (5.47)]:

$$\bar{\mathbf{D}}^* = \frac{1}{2}\sum_{\substack{j\in E\Gamma_l \\ j\in\Omega^+}} \left\{c(j)P_0^\infty(i') + d(j)\left[P_0^\infty(i') + P_0^\infty(i)\right]\right\}\tilde{\mathbf{b}}(j)\tilde{\mathbf{b}}(j). \tag{7.2}$$

$P_0^\infty(i)$-*Field* [eqs. (5.17)-(5.18)]:

$$\sum_{\substack{j\in\Omega^+(i)\\ j=\{i',i\}}} c(j)P_0^\infty(i') + d(j)\left[P_0^\infty(i') - P_0^\infty(i)\right] -$$
$$- \sum_{\substack{j\in\Omega^-(i)\\ j=\{i,i'\}}} c(j)P_0^\infty(i) + d(j)\left[P_0^\infty(i) - P_0^\infty(i')\right] = 0, \tag{7.3}$$

$$\sum_{i\in V\Gamma_l} v(i)P_0^\infty(i) = 1. \tag{7.4}$$

$\mathbf{B}(i)$-*Field* [eqs. (5.27), (5.28), (5.35) and (5.46)]:

$$\sum_{\substack{j\in\Omega^+(i)\\ j=\{i',i\}}} c(j)P_0^\infty(i')\,\mathbf{B}(i') + d(j)\left[P_0^\infty(i')\mathbf{B}(i') - P_0^\infty(i)\mathbf{B}(i)\right] -$$
$$- \sum_{\substack{j\in\Omega^-(i)\\ j=\{i,i'\}}} c(j)P_0^\infty(i)\mathbf{B}(i) + d(j)\left[P_0^\infty(i)\mathbf{B}(i) - P_0^\infty(i')\mathbf{B}(i')\right] = v(i)P_0^\infty(i)\bar{\mathbf{U}}^* - \alpha(i), \tag{7.5}$$

$$\alpha(i) = \sum_{\substack{j\in\Omega^+(i)\\ j=\{i',i\}}} \left[c(j)+d(j)\right]\mathbf{R}(j)P_0^\infty(i') - \sum_{\substack{j\in\Omega^-(i)\\ j=\{i,i'\}}} d(j)\mathbf{R}(j)P_0^\infty(i'), \tag{7.6}$$

$$\mathbf{B}(i^*) = \mathbf{0}, \tag{7.7}$$

$$\mathbf{b}(j) \overset{\text{def.}}{=} \mathbf{B}(i) - \mathbf{B}(i') \quad (j=\{i',i\}), \tag{7.8}$$

$$\tilde{\mathbf{b}}(j) = \mathbf{R}(j) - \mathbf{b}(j). \tag{7.9}$$

7.2 Reactive Transport

Mean Solute Velocity Vector [eq. (6.29)]:

$$\bar{\mathbf{U}}^{*}=\sum_{\substack{j\in E\Gamma_l\\ j\in\Omega^{+}}} c(j)\mathbf{R}\left(j\right)A(i)P_0^{\infty}(i')+d(j)\mathbf{R}\left(j\right)\left[A(i)P_0^{\infty}(i')-A(i')P_0^{\infty}(i)\right]. \tag{7.10}$$

Dispersivity Dyadic [eq. (6.52)]:

$$\bar{\mathbf{D}}^{*}=\frac{1}{2}\sum_{\substack{j\in E\Gamma_l\\ j\in\Omega^{+}}}\left\{c(j)A(i)P_0^{\infty}(i')+d(j)\left[A(i)P_0^{\infty}(i')+A(i')P_0^{\infty}(i)\right]\right\}\tilde{\mathbf{b}}(j)\tilde{\mathbf{b}}(j). \tag{7.11}$$

Mean Reaction Rate

$$\bar{K}^{*}=\min\left\{\mathrm{Re}\left(\bar{K}\right)\right\}. \tag{7.12}$$

Characteristic Eigenvalue Problem for $P_0^{\infty}(i)$ and $\bar{K}$ [eqs. (6.22) and (6.25)]:

$$\begin{aligned}\sum_{\substack{j\in\Omega^{+}(i)\\ j=\{i',i\}}} & c(j)P_0^{\infty}\left(i'\right)+d(j)\left[P_0^{\infty}(i')-P_0^{\infty}(i)\right]-\\ -\sum_{\substack{j\in\Omega^{-}\\ j=\{i,i'\}}} & c(j)P_0^{\infty}(i)+d(j)\left[P_0^{\infty}(i)-P_0^{\infty}(i')\right]\\ & +\left[\bar{K}-k(i)\right]v(i)P_0^{\infty}(i)=0,\end{aligned} \tag{7.13}$$

$$\sum_{i\in\Gamma_l} v(i)P_0^{\infty}(i)=1. \tag{7.14}$$

Adjoint Eigenvalue Problem for $A(i)$ [eqs. (6.16) and (6.26)]:

$$\begin{aligned}\sum_{\substack{j\in\Omega^{+}(i)\\ j=\{i',i\}}} & d(j)\left[A(i')-A(i)\right]+\sum_{\substack{j\in\Omega^{-}(i)\\ j=\{i,i'\}}}\left[c(j)+d(j)\right]\left[A(i')-A(i)\right]+\\ & +\left[\bar{K}-k(i)\right]v(i)A(i)=0,\end{aligned} \tag{7.15}$$

$$\sum_{i\in\Gamma_l} v(i)A(i)P_0^{\infty}(i) = 1. \tag{7.16}$$

$\mathbf{B}(i)$-*Field* [eqs. (6.35), (6.36) and (6.53)]:

$$\sum_{\substack{j\in\Omega^-(i)\\ j=\{i,i'\}}} d(j)P_0^{\infty}(i')\mathbf{b}(j) - \sum_{\substack{j\in\Omega^+(i)\\ j=\{i',i\}}} \left[c(j)+d(j)\right] P_0^{\infty}(i')\mathbf{b}(j) = v(i)P_0^{\infty}(i)\bar{\mathbf{U}}^* - \alpha(i), \tag{7.17}$$

$$\sum_{j\in\text{cycle}} \mathbf{b}(j) = \mathbf{0}, \tag{7.18}$$

$$\tilde{\mathbf{b}}(j) = \mathbf{R}(j) - \mathbf{b}(j). \tag{7.19}$$

Part II

Applications

Chapter 8

Illustrative Examples

8.1 Introduction

Up to the present juncture, this thesis has focused upon the development of a generic discrete theory for the Taylor-Aris dispersion analysis of microfluidic networks and model porous media, culminating in Chapter 7 with a pair of computational paradigms for computing the mean transport rates for non-reactive and reactive solute transport, respectively. The formulae derived in these chapters possess generic applicability, being limited only by the assumptions which are inherent in the construction of a graphical network model and the lumped-parameter model invoked to approximate the true microscale transport phenomena. The latter assumptions were discussed in detail in Chapters 1 and 3.

In the second part of this thesis, we apply the general results of our theoretical development to several specific examples. The goal of the present chapter is to illustrate the calculational mechanics of the scheme within the context of (i) a simple microfluidic device, the serpentine microchannel; and (ii) a model reactive porous medium. Both calculations are performed in exhaustive detail in the following two sections, and the results are shown to compare favorably with intuition, as well as existing theories for macroscopic transport phenomena in such media.

The computational simplicity of the scheme, as illustrated by the following examples, motivates the application of our scheme to case studies involving experimentally realized microfluidic separation processes, these being the subjects of Chapter 9 and 10. The first of these chapters elucidates the fundamental separation mechanisms which give rise to vector chromatography in microlithographic arrays. The ultimate result for the mean angle pursued by the Brownian particle, which accounts for both the asymmetry of the array and the finite size of the particle, represents a substantial improvement over existing *ad hoc* models for these separations (Duke & Austin 1998, Ertas 1998). In the second practical example, we apply our network theory to the analysis of entropic trapping devices (Han & Craighead 1999, 2000, 2002, Han *et al.* 1999). Satisfactory agreement with existing experimental results is obtained, even when employing the simplest possible network model of these devices.

Both the vector chromatography chips and entropic trapping devices are modeled using the simple network theory developed in §5.4. The analytical simplicity of the simple network, especially when compared to equivalent continuous generalized Taylor-Aris dispersion models of this type investigated previously by Dorfman & Brenner (2001), points up an important advantage of the present discrete theory. Indeed, the calculations which comprise the second part of this thesis make evident the fact that this discrete scheme, albeit less accurate than the detailed, pointwise continuous theory, is more readily applicable to engineering analyses of complex media. Further *a posteriori* motivations for applying the discrete theory are discussed in Chapter 11.

8.2 Dispersion in Serpentine Microchannels

By way of presenting an "elementary," independently confirmable, illustrative example, the present section furnishes an explicit network theory calculation of the mean velocity and dispersivity accompanying pressure-driven flow occurring in a serpentine microchannel, as depicted in Fig. 8-1. Such devices, currently proposed for compact

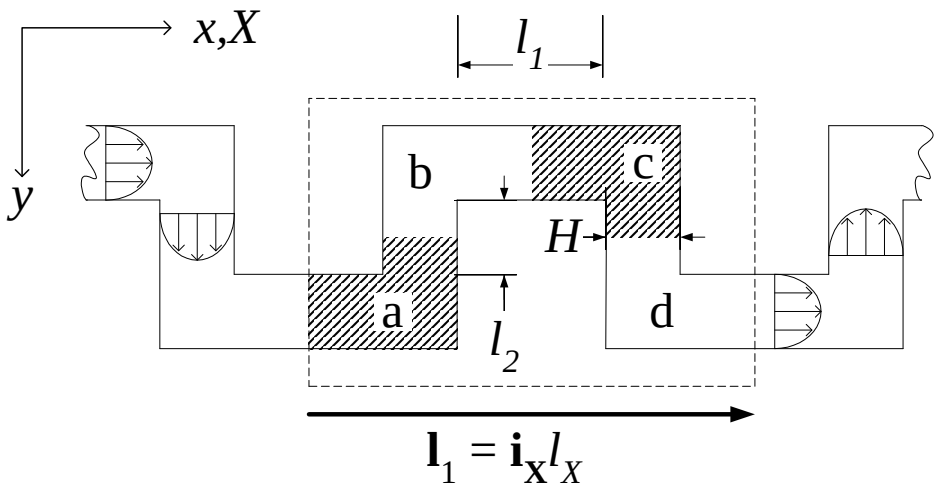

Figure 8-1: Rectangular serpentine channel comprised of infinitely extended parallel plates of constant channel width H (and area A, $A/H^2 \gg 1$). Channels oriented locally in the x- and y- direction are respectively of lengths l_1 and l_2. The unit cell of length l_X in the X-direction is indicated by the dashed box, with the periodicity and net particle transport processes occuring solely in the direction of the unit vector $\mathbf{i_X}$. Alternating shaded/unshaded regions correspond to the nodes in the local graph of Fig. 8-2.

chromatographic separations on microchips (Culbertson *et al.* 1998), have been analyzed elsewhere by Rush *et al.* (2002) within the framework of classical continuous Taylor-Aris dispersion theory for spatially periodic systems. The latter study will prove useful for verifying our discrete results in some limiting cases via comparison with the equivalent continuous results.

The network is chosen to consist of a rectangular collocation of channels possessing constant cross-sectional width H (and area A, $A/H^2 \gg 1$), arranged with period l_X in the global X-direction ($-\infty < X < \infty$). Channels oriented locally within the unit cell in the x- and y-directions possess lengths l_1 and l_2, respectively, with all channel intersections possessing equal volume. The total volume τ_0 of the unit cell accessible to the particle is written as the product of the channel area A and a characteristic linear (arc length) dimension l_s, $\tau_0 = Al_s$.

Particle transport is animated by imposing a uniform macroscopic axial pressure

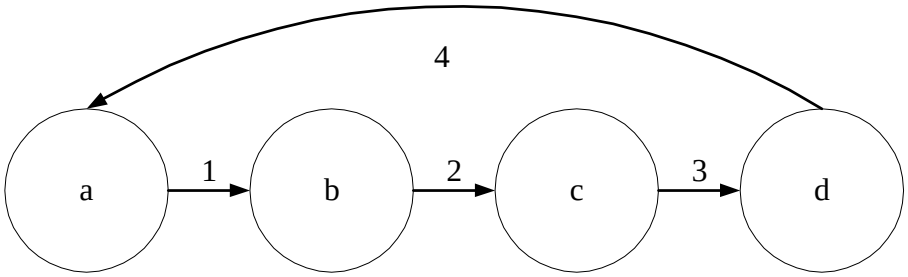

Figure 8-2: Local graph for the serpentine channel. The convective transport coefficient for all edges is equal to the volumetric fluid flow rate, $c = Q$. Edges 1 and 3 are oriented in the y-direction with diffusive transport coefficient $d_y = DA/l_2$, whereas edges 2 and 4 are oriented in the x-direction with diffusive transport coefficient $d_x = DA/l_1$.

gradient upon the interstitial fluid, giving rise to a mean solvent (and hence entrained solute particle) velocity $\bar{v}$ within the individual channels. The dispersed particles, entrained in the solvent flow, are assumed to be point-size in comparison with the channel cross-sectional width, whereupon no hydrodynamic wall effects arise in the subsequent calculations. Consequently, the molecular diffusivity of the particles in the channels is taken to be the constant scalar value D_m. Since the *net* particle (and fluid) transport is necessarily unidirectional, taking place in the X-direction, scalar notation will be employed in what follows, with the tacit understanding that all vectors and dyadics appearing within the general theory are directed entirely along the X-axis.

Figure 8-2 depicts the local graph derived from the "continuous" portrayal in Fig. 8-1. Each node consists of one-half the volume of both an x- and y-directed channel, together with an intersection, so that the nodal volumes are all equal: $v(i) = \tau_0/4$ for all i. The geometry of the serpentine configuration is captured by the following incidence

matrix, cocycle matrix and macroscopic jump vector for the local graph:

$$\mathbf{D} = \begin{bmatrix} -1 & 0 & 0 & 1 \\ 1 & -1 & 0 & 0 \\ 0 & 1 & -1 & 0 \\ 0 & 0 & 1 & -1 \end{bmatrix}, \quad \mathbf{K} = \begin{bmatrix} -1 & 1 & 0 \\ 0 & -1 & 1 \\ 0 & 0 & -1 \\ 1 & 0 & 0 \end{bmatrix}, \quad \mathbf{R} = \begin{pmatrix} 0 \\ 0 \\ 0 \\ l_X \end{pmatrix}. \tag{8.1}$$

The mean velocity $\bar{v}$ in the channels specifies the edge convection parameter, $c(j) = Q \equiv \bar{v}A$ for all j, and edge diffusivities, $d(1) = d(3) = d_y$ and $d(2) = d(4) = d_x$, wherein,

$$d_x = \frac{DA}{l_1}, \quad d_y = \frac{DA}{l_2}, \tag{8.2}$$

with D the channel-scale Taylor-Aris dispersivity prevailing within the pair of channel types. For a bounded, parallel-plate configuration of effectively infinite aspect ratio ($A/H^2 \gg 1$), the channel-scale dispersivity possesses the form (Pagitsas *et al.* 1986)[1]

$$D = D_m + \frac{1}{210}\frac{(\bar{v}H)^2}{D_m} f\left(\frac{A}{H^2}\right), \tag{8.3}$$

with $f(A/H^2) = 7.951$ in the large aspect ratio limit.

The governing matrix equation for the $P_0^\infty(i)$ appearing in eq. (5.23) is of the form

$$\begin{bmatrix} -\varphi & d_y & 0 & Q + d_x \\ Q + d_y & -\varphi & d_x & 0 \\ 0 & Q + d_x & -\varphi & d_y \\ \tau_0/4 & \tau_0/4 & \tau_0/4 & \tau_0/4 \end{bmatrix} \cdot \begin{bmatrix} P_0^\infty(a) \\ P_0^\infty(b) \\ P_0^\infty(c) \\ P_0^\infty(d) \end{bmatrix} = \begin{bmatrix} 0 \\ 0 \\ 0 \\ 1 \end{bmatrix}, \tag{8.4}$$

[1] An explicit form for the l-scale (interstitial-scale) dispersivity D is presented here for completeness. The L-scale dispersivity $\bar{D}^*$ will ultimately prove expressible as the ratio $\bar{D}^*/D$, irrespective of the exact functional form, namely (8.3), adopted for D to characterize the l-scale channel dispersion process. This is an important charactersitic of this discrete theory; namely, the fine scale processes embodied in eq. (8.3) are not explicitly resolved by our calculation scheme. Rather, our calculations serve to furnish the additional contribution of the network connectivity to the fine-scale dispersion processes.

with φ the parameter

$$\varphi = Q + d_x + d_y. \tag{8.5}$$

Clearly, eq. (8.4) possesses the solution $P_0^{\infty}(i) = \tau_0^{-1}$ for all i. Substitution into eq. (5.25) furnishes the L-scale mean velocity through the serial sequence of serpentine channels:

$$\bar{U}^* = \tau_X \bar{v}, \tag{8.6}$$

where the dimensionless parameter $\tau_X = l_X/l_s$ represents the "tortuosity" l_s of the channel projected onto the X-axis, the direction of net solute (and solvent) transport. The mean velocity $\bar{U}^*$ given by eq. (8.6) is identical to that obtained alternatively via continuous Taylor dispersion theory by Rush *et al.* (2002), as well as from intuitive arguments based upon the nominal holdup time of the solvent (and hence of the particle) as the fluid traverses a serpentine unit cell.

The structure of the cocycle matrix (8.1) identifies $B(i^*) = B(d)$. Consequently, eq. (5.34) possesses the explicit form:

$$\begin{bmatrix} -\varphi & d_y & 0 \\ Q + d_y & -\varphi & d_x \\ 0 & Q + d_x & -\varphi \end{bmatrix} \cdot \begin{bmatrix} B(a) - B(d) \\ B(b) - B(d) \\ B(c) - B(d) \end{bmatrix} = \begin{bmatrix} -\frac{3}{4} Q l_X - d_x l_X \\ \frac{1}{4} Q l_X \\ \frac{1}{4} Q l_X \end{bmatrix}, \tag{8.7}$$

whose solution, in terms of the β^- vector, is:

$$\beta^-(j) = \frac{l_X}{4V} \begin{bmatrix} \dfrac{4Dl_2 + 3\bar{v}l_1 l_2 + 2Dl_1}{D(l_1 + l_2) + \bar{v} l_1 l_2} \\ 2 \\ \dfrac{l_2(\bar{v} l_1 + 2D)}{D(l_1 + l_2) + \bar{v} l_1 l_2} \\ 0 \end{bmatrix}. \tag{8.8}$$

Conversion to $\mathbb{B}$ via eq. (5.35) is accomplished by means of the transformation matrix,

$$\mathcal{B}^{-} = (P_0^{\infty})^{-1} \begin{bmatrix} -1 & 1 & 0 & 0 \\ 0 & -1 & 1 & 0 \\ 0 & 0 & -1 & 0 \\ 1 & 0 & 0 & 0 \end{bmatrix}. \tag{8.9}$$

After transforming to $\tilde{b}$ via eq. (5.46), application of eq. (5.47) furnishes the dispersivity,

$$\frac{\bar{D}^*}{D} = \frac{\tau_X^2}{8} \left[\frac{4 + 2\tau_1\tau_2 \mathrm{Pe}_T + \tau_1\tau_2 \mathrm{Pe}_T^2}{\tau_1 + \tau_2 + \tau_1\tau_2 \mathrm{Pe}_T} \right], \tag{8.10}$$

wherein appear the following dimensionless parameters:

$$\mathrm{Pe}_T \overset{\text{def.}}{=} \frac{\bar{v} l_s}{D}, \tag{8.11}$$

$\tau_1 = l_1/l_s$, and $\tau_2 = l_2/l_s$. The latter pair represent the channel contributions to the tortuosity. The parameter Pe_T has been referred to elsewhere as the Taylor- (Sorbie & Clifford 1991) or macroscale- (Koplik *et al.* 1988) Peclet number.

The limiting behavior displayed by eq. (8.10) in the respective cases $\mathrm{Pe}_T \ll 1$ and $\mathrm{Pe}_T \gg 1$ accords with results obtained previously via classical continuous theories. Thus, Rush *et al.* (2002) examined the dispersion occurring in (intersection-free) serpentine microchannels in the limit of two-dimensional parabolic Poiseuille flow everywhere within the network, corresponding here to the limits $l_1 \to l_X/2$, $l_2 \to (l_s - l_X)/2$, and $\mathrm{Pe}_T \to 0$. The vanishingly small Peclet number in this limit implies a diffusion dominated process, where the ensuing rapid diffusive mixing renders the graph-theoretical description of the transport process essentially indistinguishable from the exact continuous description. In this limit,

$$\bar{D}^* = \tau_X^2 D, \tag{8.12}$$

in accord with the prior conclusions of Rush *et al.* (2002), as well as with existing formulas

for the effective molecular diffusivity occurring in tortuous porous media in the strict non-convective limit, $\bar{v} \to 0$ (van Brakel 1975).

In the opposite, infinite Taylor-Peclet number limit, $\mathrm{Pe}_T \to \infty$, eq. (8.10) reduces to

$$\frac{\bar{D}^*}{D_m} = \left(\frac{\tau_X l_s}{8H}\right) \mathrm{Pe} = \left(\frac{l_X}{8H}\right) \mathrm{Pe}, \tag{8.13}$$

with Pe the Peclet number, now based upon the molecular diffusivity,

$$\mathrm{Pe} \stackrel{\mathrm{def.}}{=} \frac{\bar{v}H}{D_m}. \tag{8.14}$$

The dispersivity/molecular diffusivity ratio appearing in eq. (8.13) scales linearly with Peclet number, with the proportionality coefficient functionally dependent upon the explicit array configuration. This conclusion accords with prevailing theories for convection- or hydrodynamically-dominated dispersion ("mechanical dispersion") occurring in tortuous porous media (Bear 1972, Koch & Brady 1985).

8.3 Reactive Transport in a Model Porous Medium

8.3.1 Kinematics

In this second detailed example, the general paradigm developed in Chapter 6 is applied to the model porous medium network depicted in Fig. 8-3. This medium may be envisioned as being composed of a pair of infinitely-extended parallel rows of wells, where the wells are connected via thin capillary tubes in the manner indicated in the figure. The centroids of the wells are separated by a distance l. When solute is present in well a, it is assumed to be depleted by a chemical reaction at the uniform rate k ($k > 0$). The capillaries connecting these wells possess respective cross-sectional areas A and lengths λl ($\lambda < 1$). Transport occurs within all channels by molecular diffusion, quantified by the diffusion coefficient D_m. Application of the externally applied force F gives rise to

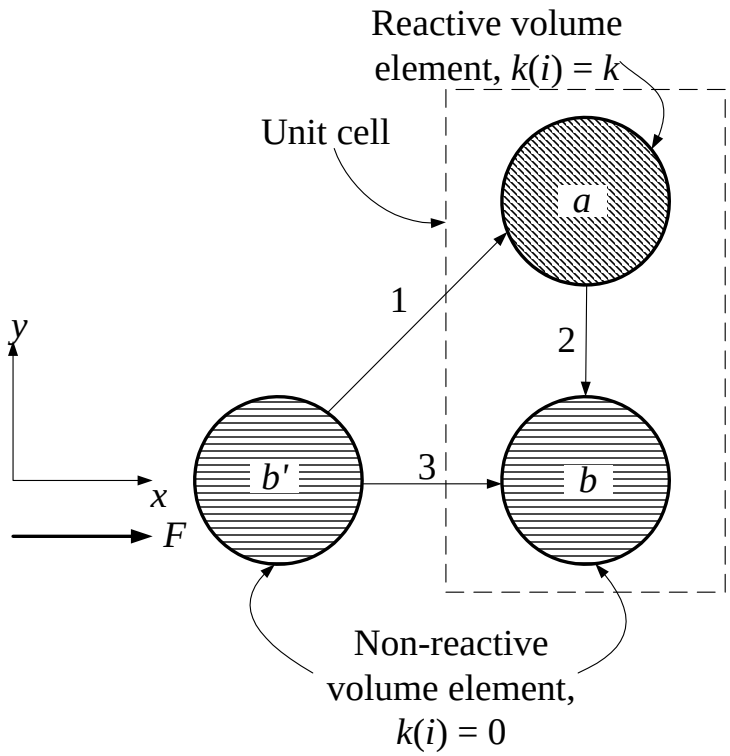

Figure 8-3: Basic graph of a model reactive porous medium. The unit cell, indicated by the dashed box, consists of two nodes, labeled a and b, connected by edges $j = \{1, 2, 3\}$. A reactive solute molecule possessing molecular diffusivity D_m is assumed not to react when present in subvolume element $v(b)$, owing, say, to the absence of a catalyst there, and to be consumed at the rate k ($k > 0$) when present in subvolume element $v(a)$, owing, say, to the presence of a catalyst. Application of an externally applied force of magnitude F in the x-direction gives rise to deterministic solute transport exclusively through edge 3.

solute transport in the x-direction. The solute is assumed to be point-size, whereupon no contribution arises from capillary-scale Taylor-Aris dispersion owing to the absence of a solvent velocity field.

The periodic unit cell, indicated by the dashed box, consists of the pair of nodes, $i = \{a, b\}$, characterized by the parameters

$$\mathbf{v} = \tau_0 \begin{bmatrix} \phi_a & 0 \\ 0 & \phi_b \end{bmatrix}, \quad \mathbf{k} = \begin{bmatrix} k & 0 \\ 0 & 0 \end{bmatrix}, \tag{8.15}$$

where $\tau_0 = v(a) + v(b)$ is the (accessible) volume of the unit cell, and ϕ_a and ϕ_b are the volume fractions of nodes a and b, respectively. The nodes are connected by a trio of edges, $j = \{1, 2, 3\}$, whose edge transport rates (5.19) and macroscopic jump vector are respectively given by

$$\mathbf{c} = \frac{D_m F A}{kT} \begin{bmatrix} 0 & 0 & 0 \\ 0 & 0 & 0 \\ 0 & 0 & 1 \end{bmatrix}, \quad \mathbf{d} = \frac{D_m A}{\lambda l} \begin{bmatrix} 1 & 0 & 0 \\ 0 & 1 & 0 \\ 0 & 0 & 1 \end{bmatrix}, \quad \mathbf{R} = l \begin{bmatrix} \hat{\mathbf{x}} \\ 0 \\ \hat{\mathbf{x}} \end{bmatrix}, \tag{8.16}$$

with kT the Boltzmann factor.

In what follows, it is useful to define the dimensionless parameters

$$\phi_e \stackrel{\text{def.}}{=} \frac{Al}{\lambda \tau_0}, \quad \text{Da} \stackrel{\text{def.}}{=} \frac{kl^2}{D_m}, \quad \text{Pe} \stackrel{\text{def.}}{=} \frac{Fl}{kT}, \tag{8.17}$$

which respectively correspond to the volume fraction of the edges, and the microscale Damkohler and Peclet numbers.

8.3.2 Macrotransport Solution

With the geometrical and phenomenological microscale transport data now specified, the eigenvalue problem (6.23) may be rendered in dimensionless form as

$$\begin{bmatrix} 2\frac{\phi_e}{\phi_a} + \mathrm{Da} & -2\frac{\phi_e}{\phi_a} \\ -2\frac{\phi_e}{\phi_b} & 2\frac{\phi_e}{\phi_b} \end{bmatrix} \cdot \begin{bmatrix} P_0^{\infty}(a) \\ P_0^{\infty}(b) \end{bmatrix} = \frac{\bar{K} l^2}{D_m} \begin{bmatrix} P_0^{\infty}(a) \\ P_0^{\infty}(b) \end{bmatrix}. \tag{8.18}$$

Upon defining the macroscopic Damkohler number as

$$\overline{\mathrm{Da}} \overset{\mathrm{def.}}{=} \frac{\bar{K}^* l^2}{D_m}, \tag{8.19}$$

the solution of the eigenvalue problem (8.18) reveals that[2]

$$\overline{\mathrm{Da}} = \frac{\phi_e}{\phi_a \phi_b} + \frac{\mathrm{Da}}{2} - \left[\left(\frac{\phi_e}{\phi_b} - \mathrm{Da} \right)^2 + \frac{\phi_e}{\phi_a} \mathrm{Da} + \frac{\phi_e^2}{\phi_a^2 \phi_b} \left(1 + \phi_a \right) \right]^{\frac{1}{2}}. \tag{8.20}$$

From inspection, we see that $\overline{\mathrm{Da}}$ vanishes with Da; likewise, $\overline{\mathrm{Da}}$ approaches infinity linearly as Da approaches infinity. Figure 8-4 displays numerical values of $\overline{\mathrm{Da}}$ (as a function of Da) for several different values of ϕ_a. $\overline{\mathrm{Da}}$ is seen to increase with Da (the apparent asymptotes appearing at $\mathrm{Da} \approx 10$ being artifacts of the semi-log plot). Owing to the fact that molecular diffusion is the sole mechanism for transporting solute into the reactive well, the overall reaction rate is much slower than that prevailing in well a. By increasing the volume of the reactive well, thereby increasing the solute residence time therein, $\overline{\mathrm{Da}}$ will increase monotonically, all other things being equal.

With use of eq. (6.25), the normalized (dimensionless) eigenvectors corresponding to

[2]The larger eigenvalue, corresponding to the more rapidly decaying transient, is similar to eq. (8.20) with a positive square root term. As was to be expected, the smallest eigenvalue is pure real.

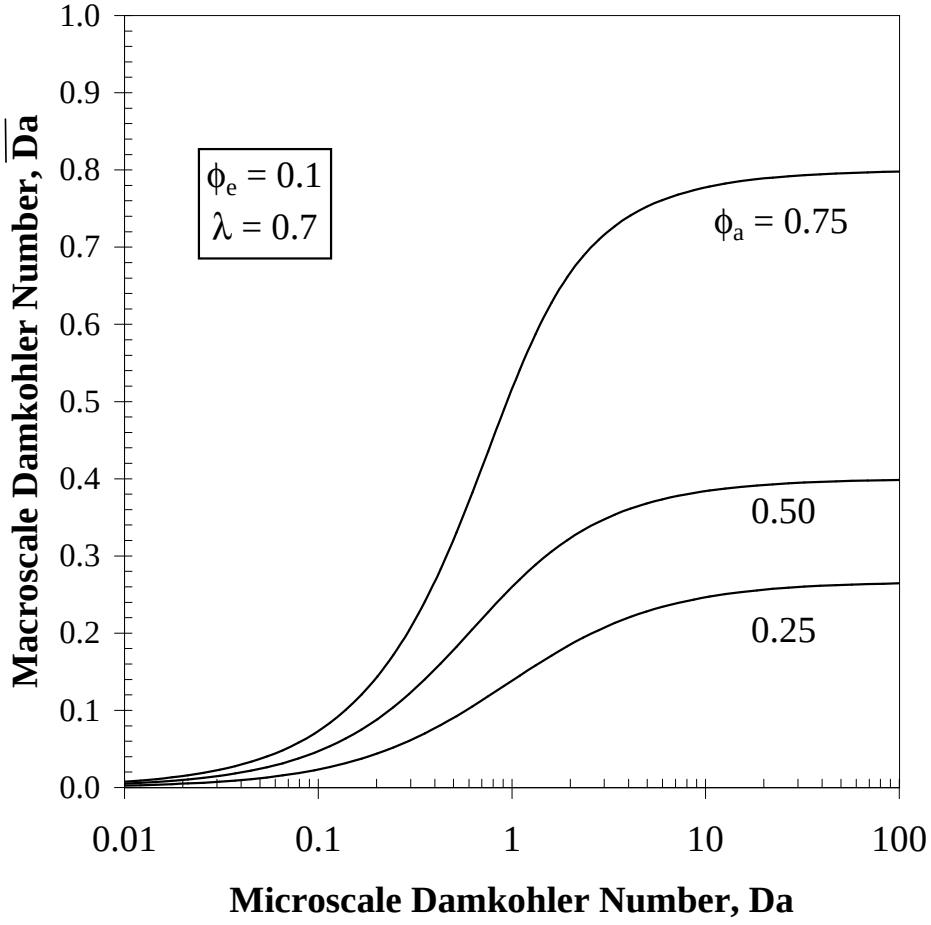

Figure 8-4: Plot of the macroscale Damkohler number, $\overline{\mathrm{Da}}$, as a function of the microscale Damkohler number, Da, for several values of the volume fraction of the reactive well, ϕ_a, and for the specified geometric attributes shown in the inset.

the smallest eigenvalue (8.20) are, respectively,

$$P_0^{\infty}(a)\tau_0 = \frac{\phi_a - \gamma}{\phi_a\,(1-\gamma)}, \tag{8.21}$$

$$P_0^{\infty}(b)\tau_0 = (1-\gamma)^{-1}\,, \tag{8.22}$$

where γ denotes the following combination of dimensionless parameters:

$$\gamma \equiv \frac{\phi_a\phi_b}{2\phi_e}\overline{\mathrm{Da}}. \tag{8.23}$$

Substitution of eq. (8.20) into eq. (6.17), together with explicitly incorporating the normalization condition (6.26) in the first row (in lieu of the equation corresponding to $i = a$), furnishes the following matrix equation for the $A(i)$:

$$\begin{bmatrix} \phi_a P_0^{\infty}(a)\tau_0 & \phi_b P_0^{\infty}(b)\tau_0 \\ 2\phi_e & \phi_b\overline{\mathrm{Da}} - 2\phi_e \end{bmatrix} \cdot \begin{bmatrix} A(a) \\ A(b) \end{bmatrix} = \begin{bmatrix} 0 \\ 1 \end{bmatrix}. \tag{8.24}$$

Solution of eq. (8.24) yields the respective fictitious initial conditions,

$$A(a) = \beta\,(1-\gamma)\,(\phi_a - \gamma)\,, \tag{8.25}$$

$$A(b) = \phi_a\beta\,(1-\gamma)\,, \tag{8.26}$$

where β is the following combination of dimensionless parameters:

$$\beta^{-1} \equiv \phi_a - 2\phi_a\gamma + \gamma^2. \tag{8.27}$$

It is readily verified that the solutions (8.25)-(8.26) satisfy eq. (6.16) for $i = a$. Moreover, $A(a) = A(b) = 1$ in the non-reactive limit, $\mathrm{Da}\rightarrow 0$, as would be expected.

Armed with knowledge of $A(i)$ and $P_0^{\infty}(i)$ the mean velocity may be calculated from

the summation (6.29), yielding

$$\bar{\mathbf{U}}^* = \hat{\mathbf{x}} D_m A \left\{ \mathrm{Pe} A(b) P_0^\infty(b) + \lambda^{-1} \left[A(a) P_0^\infty(b) - A(b) P_0^\infty(a) \right] \right\}. \tag{8.28}$$

The latter result may be simplified and rendered dimensionless via use of eqs. (8.21)-(8.22) and (8.25)-(8.26), yielding

$$\bar{\mathbf{U}}^* = \hat{\mathbf{x}} \left(\frac{D_m F}{kT} \right) \hat{U}^*, \tag{8.29}$$

in which $\hat{U}^*$ is the dimensionless scalar coefficient (i.e. speed)

$$\hat{U}^* = \lambda \beta \phi_a \phi_e. \tag{8.30}$$

The latter result reduces to $\hat{U}^* = \lambda \phi_e$ in the non-reactive Da$\rightarrow$ 0 limit, in accord with the mean velocity which would be computed directly from non-reactive network theory of Chapter 5. The dimensionless mean velocity is plotted for non-zero values of Da in Fig. 8-5. Since the solute is able to sample the tortuous diffusion path through well a, the (dimensionless) speed $\hat{U}^*$ is less than unity. The mean velocity increases with increasing reaction rate, since the solute entering well a is then depleted at a greater rate, thereby reducing its contribution to the overall transport rate. Similarly, increasing the residence time in well a causes $\hat{U}^*$ to increase. In the limit of infinite reaction rate, one would expect that no solute entering well a could contribute to the overall solute velocity, thereby leading to the value $\hat{U}^* = 1$. This contrasts with a naive limit of eq. (8.30), which would seem to imply that $\hat{U}^* = 0$. The latter incorrect limit derives from the singularity of the eigenvalue problem (8.18) at Da$\rightarrow \infty$. While not essential to this illustrative example, the proper limiting behavior could be analyzed by rescaling the problem, i.e. solving for the ratio $\bar{K}^*/k$.

The existence of numerous candidates [eqs. (6.32), (6.35), (6.39) and (6.41)] for computing the **B**-field makes the choice of its solution protocol flexible. Upon noting that

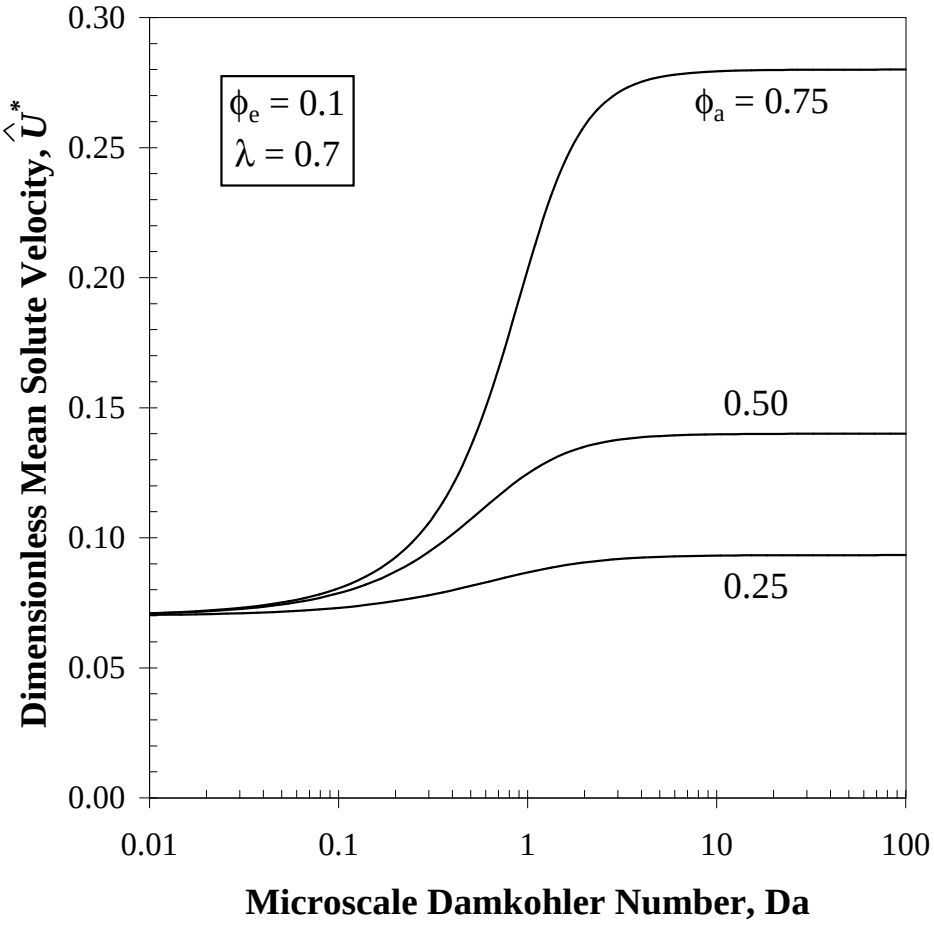

Figure 8-5: Plot of the dimensionless mean solute velocity, $\hat{U}^*$, as a function of the microscale Damkohler number, Da, for several values of the volume fraction of the reactive well, ϕ_a, and for the specified geometric attributes shown in the inset.

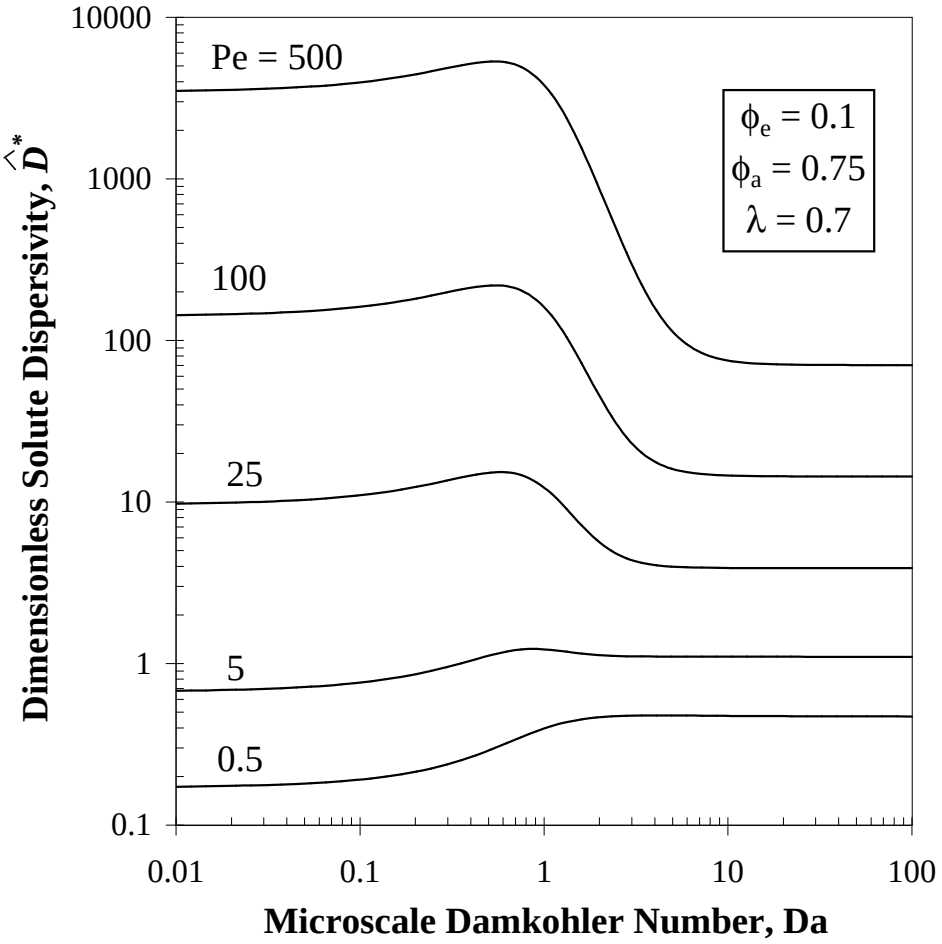

Figure 8-6: Plot of the dimensionless dispersivity, $\hat{D}^*$, as a function of the microscale Damkohler number, Da, for several values of the Peclet number, Pe, and for the specified geometric attributes shown in the inset.

the edge subsets $j = \{1, 2\}$ and $j = \{3\}$ are independent cycles on the local graph, it follows from eq. (6.36) that

$$\mathbf{b}(1) = -\mathbf{b}(2), \tag{8.31}$$

$$\mathbf{b}(3) = \mathbf{0}. \tag{8.32}$$

Use of eq. (6.35) with $i = a$ furnishes the algebraic equation,

$$\phi_e P_0^\infty(b)\tau_0 \frac{\mathbf{b}(2)}{l} - \phi_e P_0^\infty(b)\tau_0 \frac{\mathbf{b}\,(1)}{l} = \phi_a P_0^\infty(a)\tau_0 \mathrm{Pe}\bar{\mathbf{U}}^* \left(\frac{kT}{D_m F}\right) - \hat{\mathbf{x}}\phi_e P_0^\infty(b)\tau_0. \tag{8.33}$$

Together with eqs. (8.21)-(8.22), (8.30) and (8.31), this furnishes the solution

$$\frac{\mathbf{b}(1)}{l} = \frac{\hat{\mathbf{x}}}{2}\left[1 - \mathrm{Pe}\lambda\beta\phi_a\left(\phi_a - \gamma\right)\right]. \tag{8.34}$$

It is readily verified that eqs. (8.31), (8.32) and (8.34) satisfy eq. (6.35) with $i = b$.

From eq. (6.53), $\tilde{\mathbf{b}}(j) = \hat{\mathbf{x}}\tilde{b}(j)l$, wherein the dimensionless scalar coefficients $\tilde{b}(j)$ possess the respective functional forms,

$$\tilde{b}(1) = 1/2\left[1 + \mathrm{Pe}\lambda\beta\phi_a\left(\phi_a - \gamma\right)\right], \tag{8.35}$$

$$\tilde{b}(2) = 1/2\left[1 - \mathrm{Pe}\lambda\beta\phi_a\left(\phi_a - \gamma\right)\right], \tag{8.36}$$

$$\tilde{b}(3) = 1. \tag{8.37}$$

The dispersivity is calculated from (6.52) as

$$\bar{\mathbf{D}}^* = \hat{\mathbf{x}}\hat{\mathbf{x}}\frac{DAl}{2\lambda}\left\{\begin{array}{c}\left[A(a)P_0^\infty(b) + A(b)P_0^\infty(a)\right]\left[\tilde{b}^2\left(1\right) + \tilde{b}^2\left(2\right)\right] + \\ + \left(\lambda\mathrm{Pe} + 2\right)A(b)P_0^\infty(b)\tilde{b}^2(3)\end{array}\right\}, \tag{8.38}$$

which, with use of eqs. (8.21)-(8.22), (8.25)-(8.26) and (8.35)-(8.37), ultimately furnishes the dispersivity dyadic,

$$\bar{\mathbf{D}}^* = \hat{\mathbf{x}}\hat{\mathbf{x}}D_m\hat{D}^*, \tag{8.39}$$

with $\hat{D}^*$ the dimensionless scalar dispersivity,

$$\hat{D}^* = \frac{\phi_e \beta}{2} \left[3\phi_a - \gamma + \phi_a \lambda \mathrm{Pe} + (\phi_a \lambda \beta)^2 (\phi_a - \gamma)^3 \mathrm{Pe}^2 \right] . \tag{8.40}$$

In the non-reactive limit,

$$\lim_{\mathrm{Da} \to 0} \hat{D}^* = \frac{\phi_e}{2} \left[3 + \lambda \mathrm{Pe} + (\lambda \phi_a)^2 \mathrm{Pe}^2 \right] , \tag{8.41}$$

which is identical to the dispersivity which would be calculated directly from the non-reactive theory of Chapter 5.

Figure 8-6 portrays the dispersivity $\hat{D}^*$ as a function of Da for several different values of Pe. As is typically the case (Brenner & Edwards 1993), the dispersivity increases with increasing Peclet number, all other things being equal. For circumstances wherein Da < 1, the dispersivity gradually increases from its non-reactive value, eq. (8.41). Indeed, normalizing eq. (8.40) for $\hat{D}^*$ with the non-reactive value (8.41) collapses the data for Da < 1 onto a relatively thin band. At Da $= 1$, the dispersion either levels off or undergoes a precipitous drop. As Da $\to \infty$, the only contributions to $\hat{D}^*$ would be expected to arise from molecular diffusion in the non-reactive channels and mechanical dispersion resulting from the mixing process in well b. As was the case with the mean velocity, the singular nature of this limit prevents recovery of the proper limiting behavior directly from eq. (8.40).

Chapter 9

Separation Mechanisms Underlying Vector Chromatography in Microlithographic Arrays

9.1 Introduction

The use of microfabricated arrays for the chromatographic separation of Brownian particles, such as biomolecules, proffers great promise as a practical laboratory technique (Duke *et al.* 1997). Such devices typically consist of a spatially periodic, two-dimensional pattern of asymmetrically arranged obstacles embossed on a chip. Particle separation occurs within the solvent-filled channels and their intersections. For charged particles, the separation is effected by applying a time-independent electric field oriented at an angle relative to the lattice axes defining the periodic array (Chou *et al.* 1999, 2000, Duke & Austin 1998, Ertas 1998). On average, different size particles pursue chip-scale (L-scale) linear trajectories at different angles relative to the pattern. Simultaneously introducing such particles at the same point results their exit at distinctly different locations along the chip's periphery. In this Chapter, we demonstrate that this separation arises primarily from the interplay between the particle's Brownian motion and hydrodynamic wall

effects (Brenner & Gaydos 1977) connected with the finite size of the particles relative to the interstitial (l-scale) spacing between adjacent obstacles.

In a prior contribution (Dorfman & Brenner 2001) we classified this type of separation scheme as "vector" chromatography to highlight the crucial importance of the mean L-scale *direction* of the particle trajectory. Conventional "scalar" (or "unidirectional") chromatography, in contrast, relies solely upon the different L-scale mean particle *speeds* achieved through the sorting device. In the latter case, all particles move on average in the same direction, parallel to the animating force.

Our analysis focuses upon solute transport in the long-time limit $t \gg l^2/|\mathbf{D}|$, with l a characteristic linear dimension of the repetitive unit cell and $|\mathbf{D}|$ a suitable norm of the particle's l-scale molecular diffusivity tensor (Dorfman & Brenner 2001). In chips containing many obstacles (Chou *et al.* 1999, 2000), this asymptotic limit is easily achieved relative to the nominal holdup time, $t_R = L/\left|\bar{\mathbf{U}}^*\right|$, of the particle as it traverses the entire chip, with L a characteristic linear chip size and $\left|\bar{\mathbf{U}}^*\right|$ the chip-scale particle speed.

The proportionality between the applied force $\mathbf{F}$ and a given particle's mean chip-scale vector velocity $\bar{\mathbf{U}}^*$ is expressed by the relation (Dorfman & Brenner 2001)

$$\bar{\mathbf{U}}^* = \bar{\mathbf{M}}^* \cdot \mathbf{F}. \tag{9.1}$$

The proportionality coefficient $\bar{\mathbf{M}}^*$ is the chromatographic mobility dyadic of that particle, a position- and time-independent constant tensor. For a spherical particles of radius a [$a/l = O(1)$], $\bar{\mathbf{M}}^*$ is a composite phenomenological property of the particle and the chip, being functionally dependent upon (i) the particle radius; (ii) the solvent viscosity; (iii) the chip's lattice axes; (iv) the configuration and orientation of the unit cell (relative to the lattice axes); and (v) the magnitude and orientation of the force $\mathbf{F}$ relative to the lattice. Additional factors would arise for more complex, nonspherical and/or deformable molecules, such as the spring law in a bead-spring polymer model (Bird *et al.* 1987).

A directional separation is achieved when $\bar{\mathbf{U}}^*$ is not colinear with $\mathbf{F}$, i.e. when $\bar{\mathbf{M}}^*$ is anisotropic. To separate different types of particles, this anisotropy must arise from size- (or charge-) dependent interactions between the Brownian particle and the obstacle surfaces. The extent of vector separation is quantified by the relative discrimination angles, $(\theta_{UF})_i \overset{\text{def.}}{=} \cos^{-1}\left(\hat{\bar{\mathbf{U}}}_i^* \cdot \hat{\mathbf{F}}\right)$, of different species i ($i = 1, 2, \ldots N$). Here, the caret denotes a unit vector, e.g. $\bar{\mathbf{U}}_i^* = \hat{\bar{\mathbf{U}}}_i^* \left|\bar{\mathbf{U}}_i^*\right|$. In contrast, scalar chromatography is quantified by the different *magnitudes*, $\left|\bar{\mathbf{U}}_i^*\right|$, of the respective species velocities.

Prevailing theories (Duke & Austin 1998, Ertas 1998) for vector separations are restricted to point-size particles. They postulate a separation mechanism based solely upon the following conception: The particle trajectory through a unit cell possesses a bifurcation point which is caused by the asymmetry of the cell geometry and the particle's molecular diffusivity. The separation is then quantitatively rationalized by a particle-specific probability distribution function (PDF) for particle i "choosing" a particular directional bifurcation branch upon exiting a cell and entering the next cell. The PDF is different for different sized particles as a consequence of their different molecular diffusivities. Initial announcements of this separation phenomenon by Duke & Austin (1998) used the name "rectified Brownian motion" to highlight the dependence of the PDF upon such diffusive effects. However, the assumption of point-size particles lies counter to the later experiments of Chou *et al.* (1999, 2000) originally demonstrating such vector separations. In fact, the particles occupied a significant fraction of the interstitial space between adjacent obstacles.

To properly account for hydrodynamic effects, consider the l-scale, interstitial mobility dyadic $\mathbf{M}(\mathbf{x})$ of a finite-size particle, where $\mathbf{x}$ refers to the center of the particle. This mobility is both anisotropic and strongly dependent upon the instantaneous particle position $\mathbf{x}$ due to wall effects (Brenner & Gaydos 1977) — even for spherical particles. In what follows, we will show that such wall-induced effects upon the particle's mobility play a crucial role in determining $\bar{\mathbf{M}}^*$ and θ_{UF}, even to the extent of permitting vector separations when the choice of bifurcation branch is totally random!

9.2 Network Model

By way of illustration, as in Fig. 9-1, consider rectangular obstacles arranged symmetrically in a rectangular array. Here the lattice axes, characterized by unit vectors $\hat{\mathbf{X}}$ and $\hat{\mathbf{Y}}$, coincide with the obstacle axes (x, y). The charged particle moves through the array under the influence of an external force $\mathbf{F}$, which is oriented at an angle θ_{FX} relative to the X-axis. Whereas the present analysis explicitly considers spherical particles and rectangular arrays, our eventual conclusions transcend these restrictions. In particular, the spherical particle assumption may be relaxed by employing a microscale mobility dyadic $\mathbf{M}(\mathbf{x})$ valid for more complex molecules (Bird *et al.* 1987).

In general, the chromatographic mobility of a solute particle in a fluid of viscosity η may be expressed as $\bar{\mathbf{M}}^*/6\pi\eta a = \hat{\mathbf{X}}\hat{\mathbf{X}}\bar{M}_X^* + \hat{\mathbf{Y}}\hat{\mathbf{Y}}\bar{M}_Y^*$. (The Stokes law scaling is arbitrary.) Here, for a given particle, the (dimensionless) scalar components $\bar{M}_X^*$ and $\bar{M}_Y^*$ depend functionally upon the dimensionless groups characterizing the transport process — explicitly, $\bar{M}_J^* = \bar{M}_J^*\left(a/W_j, F_j l_j/kT, W_j U_j/\left|\mathbf{D}\right|, \text{etc.}\right)$, with U_j $[j = (x, y)]$ the Taylor-Aris l-scale average particle speed through a j-directed channel.[1] Vector separation ensues whenever the distinctive particle properties appearing in the arguments of these two mobility components result in the inequality $\bar{M}_X^* \neq \bar{M}_Y^*$ for a given particle i.

To compute $\bar{\mathbf{M}}^*$, we employ the network theory for generalized Taylor-Aris dispersion phenomena, whose details were discussed in the previous chapters. The micropatterned device is represented as a spatially periodic, interconnected network of channels together with their intersections. Classical Taylor-Aris particle velocities and dispersivities (Brenner & Edwards 1993) are used to quantify the convective-diffusive transport processes occurring in these channels. When the particle is present within an intersection, the choice of the particle's intersection egress channel is assumed to be furnished by a particle-size dependent "mixing rule" which simulates the physical transport processes occurring within that intersection. Although in contrast with prior models (Duke &

[1] Majuscule indices refer to L-scale directions (X, Y) and miniscule indices to l-scale directions (x, y).

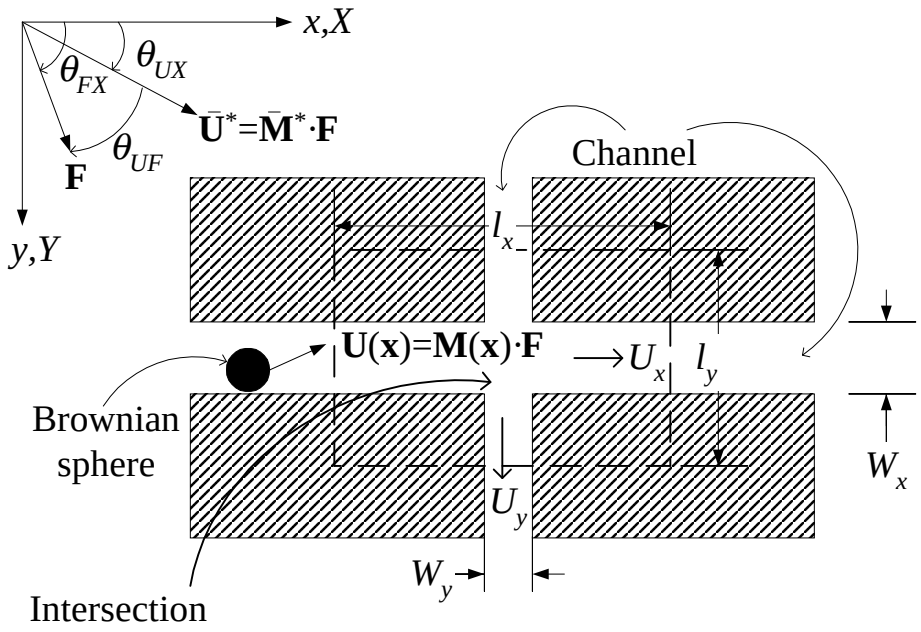

Figure 9-1: Spatially periodic microscale rectangular lattice ($l_x \neq l_y$) of rectangular obstacles (shown shaded) spaced at interstitial channel widths $W_x \neq W_y$. The position-independent external force $\mathbf{F}$ is orientated at an angle θ_{FX} with respect to the x-lattice vector of the array. With its center situated at a point $\mathbf{x} \equiv (x, y)$ within a channel, the sphere moves instantaneously with velocity $\mathbf{U}(\mathbf{x}) = \mathbf{M}(\mathbf{x}) \cdot \mathbf{F}$. The mean l-scale Taylor-Aris particle velocity components through a channel within a single cell are denoted respectively by U_x and U_y. On the chip-scale the particle moves, on average, across the chip with its (L-scale) velocity vector $\bar{\mathbf{U}}^* = \bar{\mathbf{M}}^* \cdot \mathbf{F}$. This vector is oriented at an angle θ_{UX} relative to the $x \equiv X$-axis. The disparity in angular direction between $\bar{\mathbf{U}}^*$ and $\mathbf{F}$ gives rise to the chip-scale discrimination angle θ_{UF}. Notationally, $\mathbf{x} = (x, y)$ are l-scale coordinates ($0 < x < l_x$, $0 < y < l_y$), whereas (X, Y) are L-scale coordinates.

Austin 1998, Ertas 1998), this fact is not essential to the vector separation phenomenon because of our incorporation of hydrodynamic wall effects. We will focus only upon the task of establishing the *direction* of the particle trajectory, although the general theory permits a complete Taylor-Aris dispersion analysis, including the chip-scale particle velocity $\bar{\mathbf{U}}^*$.

The network depicted in Fig. 9-1 is a so-called "simple network" (see §5.4) consisting of a single intersection joining together x- and y-directed channels at their mouths. The particle's probability density is trivial — the particle must be located within the single nodal area contained within the unit cell boundaries. Consequently, computing $\bar{\mathbf{U}}^*$ simply necessitates defining: (i) the particle's probability density "flow rate" Q_j within x- and y-directed channels; and (ii) the probability ratio K of the particle choosing x- and y-directed channels at the intersections.

For a given particle, the probability flow rate through channel j is given by $Q_j = \mu_j F_j W_j$, with μ_j the particle's l-scale mean mobility in channel j, F_j the component of the external force along the direction of the channel, and W_j the channel width. When $l_j \gg W_j$, μ_j possesses its classical Taylor-Aris dispersion value in the channel (Brenner & Edwards 1993), which includes a Boltzmann bias arising from the action of the transverse force:

$$\mu_j = \frac{\int_0^{W_j} dx_k \, M_{jj}(x_k) \exp\left(F_k x_k / kT\right)}{\int_0^{W_j} dx_k \, \exp\left(F_k x_k / kT\right)} \quad (j,k = x,y; j \neq k)\,, \tag{9.2}$$

where M_{jj} is the component of $\mathbf{M}(\mathbf{x})$ in the j direction and kT is the Boltzmann factor. For spherical particles and planar channel geometries, the pointwise mobility dyadic $\mathbf{M}(\mathbf{x})$, including wall effects, is available from rigorous hydrodynamic theory (Happel & Brenner 1983, Kim & Karrila 1991). For more complex molecules, it remains possible to make this calculation using approximate hydrodynamic theory (Jendrejack *et al.* 2000). When the chip geometry and/or the molecular shape exceed computational resources, μ_j may be determined from experiments performed using a single channel of large aspect ratio, $l_j \gg W_j$. Equation (9.2) is a generic result, rendering later conclusions based upon μ_j [cf. eq. (9.3)] independent of our spherical particle assumption.

Quantifying K depends upon the particle Peclet number, Pe, representing the ratio of convective to diffusive transport rates within the intersection. Perfect mixing (Adler & Brenner 1984b) is assumed for diffusion dominated transport, $\mathrm{Pe} \ll 1$, so that all intersectional egress channels are equally probable. This corresponds to randomizing the choice of bifurcation branch in existing point-size theories (Duke & Austin 1998, Ertas 1998). For convection dominated transport, $\mathrm{Pe} \gg 1$, the choice of intersectional egress channel is assumed to be proportional to the channel's flow rate Q_j (Sahimi *et al.* 1983). Any value of Pe can be encompassed by defining the partition coefficient, $K = \mathrm{Prob}(y)/\mathrm{Prob}(x)$, with $\mathrm{Prob}(j)$ the probability of the particle entering channel j upon exiting the intersection. Consequently, $K = 1$ and $K = Q_y/Q_x$ in the respective low and high Peclet number limits.

The preceding analysis, when brought to fruition in accordance with §5.4, enables the particle's chip-scale velocity components $\bar{U}_X^*$ and $\bar{U}_Y^*$ to be explicitly calculated. The angle θ_{UX} formed by $\bar{\mathbf{U}}^*$ and the X-axis is given by

$$\tan\theta_{UX} \stackrel{\text{def.}}{=} \frac{\bar{U}_Y^*}{\bar{U}_X^*} = \mu K \frac{W_y l_y}{W_x l_x}\frac{F_y}{F_x}, \tag{9.3}$$

with $\mu \equiv \mu_y/\mu_x$. The discrimination angle is then computed by

$$\theta_{UF} = \theta_{UX} - \tan^{-1}(F_y/F_x). \tag{9.4}$$

This analysis also furnishes the components $\bar{M}_X^*$ and $\bar{M}_Y^*$ of $\bar{\mathbf{M}}^*$, since $\bar{U}_X^*$ and $\bar{U}_Y^*$ are related to F_x and F_y by eq. (9.3).

9.3 Discussion

Several generic geometric conclusions are apparent from eqs. (9.3)-(9.4). First, when $\mathbf{F}$ is applied along a symmetry axis of the array (the X- or Y-direction), the discrimination angle $\theta_{UF} = 0$ and is independent of the particle properties. Second, for point-sized par-

ticles and perfect mixing ($\mu = K = 1$), θ_{UF} is characterized exclusively by the symmetry group of the "composite" $l \oplus L$-scale array geometry. Explicitly, the spatial arrangement of the obstacles determines the L-scale lattice symmetry, whereas the obstacle's shape determines the l-scale point-group symmetry class. The symmetry of the composite $l \oplus L$-array consists of common symmetry elements, if any, between the respective lattice and obstacle point-group rotational symmetries. These symmetries need not be the same; for example, regular pentagonal-shaped objects in a rectangular array possess no common symmetry elements (except for a center of symmetry), irrespective of the orientation of the obstacles relative to the lattice.

To clarify the preceding comments, we examine the array depicted in Fig. 9-1. When $W_x = W_y$ and $l_x = l_y$, the array consists of square obstacles in a square lattice, with coincident rotational symmetry axes. The four-fold $l \oplus L$ composite symmetry[2] of this array makes $\bar{\mathbf{M}}^*$ isotropic and $\theta_{UF} = 0$, irrespective of the orientation of $\mathbf{F}$ relative to the lattice axes. In contrast, an array with $W_x \neq W_y$ or $l_x \neq l_y$ represents either square objects in a rectangular array or rectangular objects in a square array. These lattices only possess two-fold rotational symmetry. Second-rank tensors associated with two-fold symmetry are anisotropic (Billings 1969), so particle motion is no longer colinear with the force. However, vector separation requires that the physical attributes of the particles cause the anisotropy. If the anisotropy is attributable only to the array symmetry, then all particles will move on average in the same direction, albeit in a direction no longer colinear with the force.

Thus, vector separation is possible only when the parameters μ and K appearing in eq. (9.3) differ between particles. Existing theories (Duke & Austin 1998, Ertas 1998) consider the case where K (but not μ) is a function of the particle properties. When wall effects are substantial, the simplest method for altering μ is to construct an array with different gap widths, namely $W_x \neq W_y$. Variable gap widths have a nonlinear

[2]Were the point-group symmetry rotation axes of the square obstacles not aligned with those of the square lattice, the only common symmetry element would be a center of symmetry. Consequently, the array would no longer be isotropic with respect to second rank tensors.

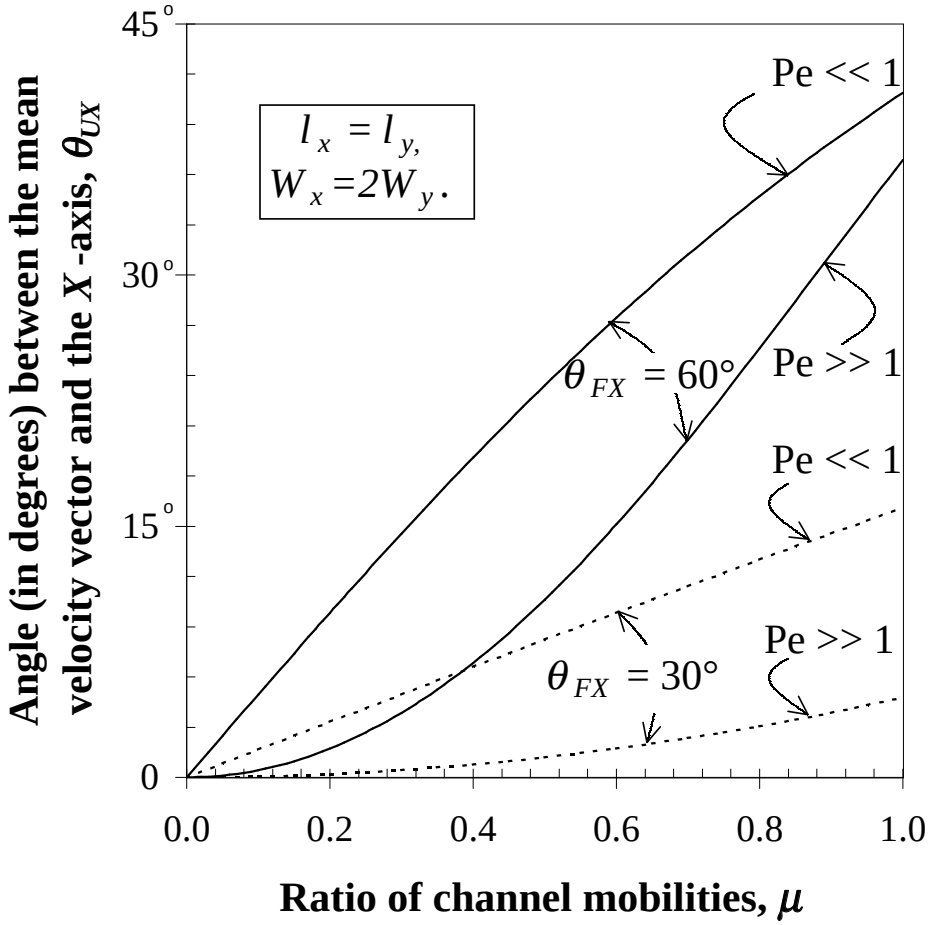

Figure 9-2: Angle θ_{UX} formed between the particle's chip-scale mean velocity vector $\bar{\mathbf{U}}^*$ and the X-axis for the conditions indicated in the inset. Solid and dashed lines correspond to angles $\theta_{FX} = 60°$ and 30°, respectively, between the applied force $\mathbf{F}$ and the X-axis.

effect upon the channel particle mobilities μ_j via eq. (9.2), as well as imparting two-fold symmetry to the array. Alternatively, even for four-fold symmetric arrays, the presence of a strong transverse force, $F_j \gg F_k$, in one of the channels biases μ_j as a consequence of the Boltzmann factor in eq. (9.2). In either case, the chromatographic mobility $\bar{\mathbf{M}}^*$ no longer possesses the four-fold point-group symmetry characterizing the array geometry. This symmetry-breaking feature underlies the fundamental mechanism of vector chromatography.

Consider the explicit example of a square lattice, $l_x = l_y$, with rectangular obstacles separated by distances $W_x = 2W_y$. The relative widths impart a wall-effect-induced preference for particle motion in the x-direction, as well as imposing the inequality $\mu \leq 1$. Figure 9-2 depicts the angle θ_{UX} as a function of μ, for the limiting cases of both perfect mixing and convection-dominated transport at the intersection. For point-size particles ($\mu = 1$), we see that the two-fold symmetry of the array results in $\theta_{UX} \neq \theta_{FX}$. For finite-size particles, vector chromatography is possible even for the case where $K = 1$, where the bifurcation branch is totally random. The range of available angles θ_{UX} is small when applying the force at the angle $\theta_{FX} = 30°$. This makes a vector separation difficult. In contrast, applying the force at an angle $\theta_{FX} = 60°$ — "against" the preferred direction — makes for an easier vector separation. This increased efficiency accords with the experimental results of Chou *et al.* (1999, 2000), where the greater component of the force coincided with the narrower channel.

Chapter 10

Modeling DNA Electrophoresis in Microfluidic Entropic Trapping Devices

10.1 Introduction

The ongoing development of microfluidic techniques (Jakeway *et al.* 2000, Kutter 2000, Slater *et al.* 1998) for DNA electrophoresis is motivated by the need for rapid, reproducible, laboratory-scale separations. Within barely several minutes of operation, these novel experimental protocols often furnish separation resolutions comparable with those achieved only after several hours of conventional slab gel electrophoresis (Han & Craighead 2000). Moreover, the microfabrication techniques (Jakeway *et al.* 2000) available for constructing such devices allow for the creation of perfectly periodic device microstructures, eliminating thereby the configurational randomness inherent in electrophoretic gels. The maturation of such microfluidic separation devices requires rationalizing, and thereby predicting, attainable separation qualities in terms of device configuration and measurable experimental parameters — a task accomplished here for microfluidic entropic trapping devices (Han & Craighead 1999, 2000, 2002, Han *et al.* 1999).

The entropic trapping (Arvanitidou & Hoagland 1991, Liu *et al.* 1999, Muthukumar & Baumgartner 1989a,b, Nixon & Slater 1996, Rousseau *et al.* 1997, Slater & Wu 1995, Smisek & Hoagland 1990) of flexible linear macromolecules (polymers), in this case DNA, constitutes a form of hindered solute transport in porous media. Explicitly, when undergoing reptation in a pore whose effective radius is less than that of the radius of gyration of the macromolecule, the polymer chain adopts an elongated, entropically unfavorable conformation. Conversely, the polymer coils up into an entropically favorable conformation when present in a void (trap) whose characteristic linear dimension exceeds that of the polymer's radius of gyration. When the porous medium consists of both voids and narrow pores, polymers of differing lengths — owing to a chain-length dependent transitional energy barrier for exiting a void — spend disproportionate amounts of time dwelling therein; hence the name, "entropic trapping."

Han & Craighead (Han & Craighead 1999, 2000, 2002, Han *et al.* 1999) exploited the chain-length dependence of entropic trapping to effect the electrophoretic separation of different length strands of DNA. Such strands would otherwise be convected at identical rates owing to their *size-independent* (Volkmuth *et al.* 1994) electrophoretic mobilities, μ_0. The microdevice developed by Han & Craighead (2000) consisted of a unidirectional, rectangular chromatography channel possessing a square wave depth, with the deeply etched traps (650 nm deep) separated at uniform intervals by narrow constrictions (90 nm deep). DNA motion across the chip was animated by applying an external electric field.

When both long and short strands of DNA were injected simultaneously into the device, Han *et al.* (1999) observed that the long strands eluted from the column first. This surprising behavior was rationalized by Han *et al.* (1999) by arguing that the polymer must escape the trap via the formation of a "beachhead," the latter envisioned as consisting of several monomer units extending into the narrow constriction. While the complex nature of this proposed escape mechanism renders it difficult to effect a "first-principles" calculation of the time necessary to form a beachhead, a semi-empirical phenomenologi-

cal model of the phenomenon [cf. eq. (10.25)] was proposed and verified experimentally by Han *et al.* (1999) within a limited region of the parameter space.

Our analysis furnishes a coarse-grained theoretical model of the workings of their device, based upon the generalized Taylor-Aris dispersion (macrotransport) scheme developed in Chapter 5. This general network modeling scheme embodies a rigorous physicomathematical paradigm for computing the two macrotransport parameters quantifying external-force animated chip-scale solute transport in periodically arrayed structures, namely the mean solute velocity $\bar{U}^*$ and dispersivity $\bar{D}^*$. This calculation utilizes knowledge of the lumped-parameter interstitial transport processes, together with a graphical decomposition of the device connectivity into node-to-node (trap-to-trap) displacements. Attention is restricted to "simple" networks (see §5.4) comprised of a repetitive sequence of equispaced, identical traps. Mean solute transport rates for more complex networks (such as those consisting of several differently-sized traps, albeit still arranged periodically) can readily be calculated within the general Taylor-Aris dispersion framework developed in Part I of this thesis.

Despite the extensive attention (Arvanitidou & Hoagland 1991, Liu *et al.* 1999, Muthukumar & Baumgartner 1989a,b, Nixon & Slater 1996, Rousseau *et al.* 1997, Slater & Wu 1995, Smisek & Hoagland 1990) focused upon modeling the microscale phenomenon of entropic trapping, quantitative characterization of the functional dependence of the average trap residence time upon the trap geometry, thermodynamics and DNA transport properties remains incomplete. One particular impediment towards developing a rational microscale theory resides in the difficulty of experimentally measuring single trapping events within controlled environments (Han *et al.* 1999). While our primary motivation here lies in attempting to rationalize the chromatographic results of Han & Craighead (2000) and some later observations (Han & Craighead 2002) on separation resolution, our theoretical analysis may be expected to assist in developing a more complete microscale model of the trapping phenomena, inasmuch as the device geometry is well defined (Han & Craighead 1999) and our analysis entails the use of easily measured,

average transport properties.

The next section presents a macrotransport analysis of the network description of Han & Craighead's device. It is supposed therein that the mean time spent in a trap presently cannot be calculated *a priori*. In lieu of such information we detail an alternative closure scheme, leading ultimately to the calculation of a trio of chromatographic parameters, namely the solute dispersivity $\bar{D}^*$, number of theoretical plates n, and the separation resolution R_s. Section 10.3 compares our theoretical predictions with observed experimental trends and available data. We conclude in Section 10.4 with suggestions for extending the scope of the present analysis.

10.2 Macrotransport Analysis

Figure 10-1 depicts the graphical decomposition of a representative entropic trapping device. Holdup in each trap, separated from its nearest neighbor by a distance l, is represented by the trap-independent average retention time, τ. No assumptions are made concerning the functional dependence of τ upon the parameters to be enumerated forthwith,[1] although the first two moments of τ over the distribution of residence times are required to be finite (Weiss 1994) in order to satisfy fundamental convergence assumptions implicit in the underlying theory [as embodied in eq. (4.2)]. Application of an externally applied electric field, with field strength E in the narrow constrictions connecting the traps, causes an individual DNA molecule therein to move with a "convective (or deterministic) velocity" $c = \mu_0 E$, where μ_0 is the electrophoretic mobility of DNA through the unbounded solvent.[2] Diffusive transport in the connecting passages between traps is parameterized by the probabilistic "diffusion velocity" $d = D/l$, with D

[1] As a consequence of its phenomenological nature, this model does not predict the observed disappearance of entropic trapping at high field strengths (Han & Craighead 2000, Rousseau *et al.* 1997), a singular limit in the underlying theory.

[2] Variations in the field strength between the narrow and deep regions of the chip occur on a length scale finer than this coarse-scale model. Consequently, we only concern ourselves with the *total* potential drop embodied by E, rather than any fine-scale field variations.

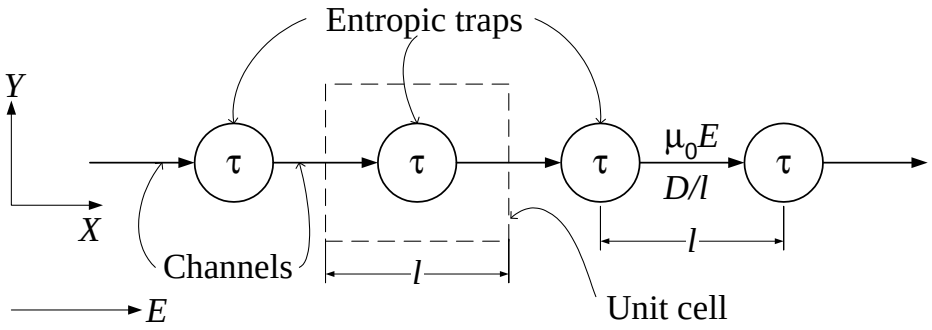

Figure 10-1: Graphical network representation of a spatially periodic entropic trapping device. The traps, represented here by circles, are separated by a distance l in the X-direction. Application of an electric field E along the X-direction gives rise to a velocity $\mu_0 E$ of the DNA within the channels connecting the traps. Diffusive transport in these channels is quantified by the interstitial-scale diffusivity D, together with a concomitant "diffusive velocity," D/l. This convective-diffusive solute transport through the device is hindered by the entropic traps, each of which retains a DNA molecule, on average, for a period of time τ. The spatial periodicity of the device is reflected by the presence of a primitive unit cell, denoted above by the contents of the dashed box. The composite device consists of a large number, N, of such cells, whereby the total length available for the separation is $L = Nl$ ($L \gg l$).

the DNA's molecular diffusivity,[3] estimated via the Zimm model (Ertas 1998, Volkmuth *et al.* 1994). Within the context of macrotransport theory for spatially periodic networks in Chapter 5, a single trap-to-trap displacement of a DNA molecule corresponds to the macroscopic "jump" of $R = l$. The composite device is assumed to consist of N ($N \gg 1$) trap/channel unit-cell pairs, giving rise to a total chip length $L = Nl$. Because the underlying theory of Chapter 5 is based upon an infinitely-extended medium, the subsequent analysis is strictly valid only in the limit $N \gg 1$.

By invoking a graphical representation of the relevant transport phenomena, the detailed quantification of the convective-diffusive transport processes occurring within a trap is effectively supplanted by introducing an average retention time, τ. As such, τ accounts for both the nominal convection time required to cross the trap and the

[3]In accordance with the notation of previous chapters, we have here that $D_m = D$.

time required to form the trap-exiting beachhead. Moreover, the length l refers to the distance between, say, the centroids of adjacent traps, rather than to the physical length of a connecting channel, the latter being strictly less than the length l. A more detailed network model might have been considered, wherein the periodic network would now consist of three, rather than two, regions: (i) the thin connecting channel; (ii) the "convective" portion of the trap; and (iii) the "beachhead" portion of the trap. Such a model would also reflect differences in electric field strength between the constrictions and the traps. However, given the difficulty in clearly distinguishing between the time required to form a beachhead and the total time spent in the trap, it is more consistent in light of the limited data available to proceed with the original, less detailed, two-region model.

To apply our Taylor-Aris network theory to the problem at hand, the "probabilistic" volume, V,[4] per unit area of the unit cell must be specified. As will be subsequently demonstrated, this probabilistic volume V is not necessarily equal to the physical volume per unit area, namely l. In this context, the nominal holdup time, t_u, within a unit cell is assumed to consist of the trapping time, τ, and the convection time required to negotiate the distance, l, between traps:

$$t_u = \tau + \frac{l}{\mu_0 E}. \tag{10.1}$$

In the absence of the entropic traps, convection occurs at the constant velocity $\mu_0 E$, equipollent to the distance (volume per unit area) $V = (\mu_0 E)\, t_u$. Consequently,

$$V = l + \tau \mu_0 E, \tag{10.2}$$

which accounts for both the physical volume of the unit cell and the additional, probabilistic volume arising from the trap's residence time.[5]

[4]The symbol V is employed here, in lieu of the notation τ_0, to avoid confusion with the trapping time τ.

[5]When the entropic trapping effect vanishes, corresponding to the fact that $\tau \to 0$, the probabilistic volume, V, becomes equal to the physical volume (per unit area), l.

Closed-form expressions for $\bar{U}^*$ and $\bar{D}^*$ were derived in §5.4 for single node ("simple") networks, such as that depicted in Fig. 10-1, leading to the values

$$\bar{U}^* = \frac{R}{V}c, \tag{10.3}$$

$$\bar{D}^* = \frac{R^2}{2V}\left(c + 2d\right). \tag{10.4}$$

Substitution of the functional forms of c and R into eq. (10.3), together with use of eq. (10.2), furnishes the mean solute speed,

$$\bar{U}^* = \left(\frac{1}{1+\varepsilon}\right)\mu_0 E, \tag{10.5}$$

with ε the ratio of trapping-to-convection time scales:

$$\varepsilon \overset{\text{def.}}{=} \frac{\tau\mu_0 E}{l}. \tag{10.6}$$

Equation (10.5) renders transparent a method for measuring ε (and thereby τ), a scheme which was rationalized intuitively in the pioneering studies of this class of devices (Han & Craighead 1999, Han *et al.* 1999). Explicitly, with holdup time t_R in a chip of length L, the mean solute velocity possesses the Lagrangian interpretation

$$\bar{U}^* = \frac{L}{t_R}, \tag{10.7}$$

whence comparison of the above with eq. (10.5) reveals that

$$\varepsilon = \frac{\mu_0 E t_R}{L} - 1. \tag{10.8}$$

Inasmuch as subsequent calculations prove to be functionally dependent upon knowledge of the parameter ε, eq. (10.8) represents the closure of our theoretical scheme, enabling τ to be computed from measurable parameters.

From eqs. (10.2), (10.4) and (10.6), the solute dispersivity adopts the form

$$\bar{D}^* = D\left(\frac{1}{1+\varepsilon}\right)\left(1+\frac{\mathrm{Pe}}{2}\right), \tag{10.9}$$

with the Peclet number, Pe, defined as[6]

$$\mathrm{Pe} \overset{\text{def.}}{=} \frac{\mu_0 El}{D}. \tag{10.10}$$

While the electrophoretic mobility μ_0 is typically independent of DNA chain-length (Volkmuth *et al.* 1994), the Peclet number is not, since D is size-dependent when approximated by the Zimm model (Ertas 1998, Volkmuth *et al.* 1994).

In the context of formulating a macroscopic model for the rational design of their entropic trapping device, Han & Craighead (2002) assert that the standard deviation of the band width as the solute band exits the device,

$$\sigma = \sqrt{2\bar{D}^* t_R}, \tag{10.11}$$

may be computed by the approximate relationship,[7]

$$\sigma \propto \sqrt{N}\tau. \tag{10.12}$$

To compare this claim with the more rigorous results of the present model, we compute the total retention time, t_R, by eq. (10.7), whence, with use of eq. (10.9), the standard deviation adopts the form

$$\sigma = L\sqrt{2\left(1+\frac{1}{\mathrm{Pe}}\right)}. \tag{10.13}$$

Clearly, our result for the standard deviation is functionally dependent upon the total

[6]The microscale Peclet number, Pe, is indistinguishable from the Taylor-Peclet number, Pe_T, defined by eq. (8.11) since the channel scale dispersion is assumed to be equal to the molecular diffusivity.

[7]It is presumed that there also exists a dimensional coefficient which renders σ in units of length.

size of the device, as embodied in L, as well as the ratio of convective and diffusive transport, as embodied in Pe. This contrasts sharply with the *ad hoc* dispersion relationship proposed by Han & Craighead (2002), which only depends upon the trapping time. One would certainly expect that molecular diffusion in the narrow channels would contribute to the band spreading, although the large values of the Peclet number (cf. Table 10.2) make this contribution small, whereupon

$$\sigma \approx L\sqrt{2} \quad (\mathrm{Pe} \gg 1). \tag{10.14}$$

Nevertheless, our result (10.13) more accurately reflects the relative contributions of the microscale physics to the macroscopic quanitity σ than does the estimate (10.12).

The theoretical plate height, H_p, is defined by the expression (Giddings 1991)

$$H_p \stackrel{\text{def.}}{=} \frac{2\bar{D}^*}{\bar{U}^*}. \tag{10.15}$$

Substitution of eqs. (10.5) and (10.9) into eq. (10.15) furnishes the nondimensional plate height per trap:

$$\frac{H_p}{l} = 1 + \frac{2}{\mathrm{Pe}}. \tag{10.16}$$

With a chip length L embodying N traps, the number, n, of theoretical plates parameterizing the chip is thereby given by the expression

$$n = \frac{L}{H_p} = \frac{N}{1 + 2\mathrm{Pe}^{-1}}. \tag{10.17}$$

Though n exhibits no explicit dependence upon τ (or ε), an implicit dependence must exist owing to the inseparable relationship (Han & Craighead 2000, Rousseau *et al.* 1997) existing between the entropic trapping phenomenon and the electric field strength E, the latter embodied in Pe. In many practical instances the Peclet number is large (cf. Table 10.2), i.e. $\mathrm{Pe} \gg 1$, whereupon the number of theoretical plates approaches the number

of traps:

$$n \approx N \quad (\mathrm{Pe} \gg 1)\,. \tag{10.18}$$

The separation resolution, R_s, at time t between solute molecules 1 and 2, injected simultaneously into the device at time $t = 0$, is defined as (Giddings 1991)[8]

$$R_s \overset{\text{def.}}{=} \frac{|X_2 - X_1|}{2(\sigma_1 + \sigma_2)}, \tag{10.19}$$

where, for the i^{th} species band, X_i and σ_i represent the respective peak position of the band and standard deviation therefrom. Inasmuch as $X_i = \bar{U}_i^* t$ and $\sigma_i = \sqrt{2\bar{D}^* t}$, the resolution at time t possesses the form

$$R_s = \frac{\left|\bar{U}_2^* - \bar{U}_1^*\right|}{2\sqrt{2}\left(\sqrt{\bar{D}_1^*} + \sqrt{\bar{D}_2^*}\right)} t^{1/2}. \tag{10.20}$$

Of particular interest is the resolution achieved as the first band, say species 2, exits the device. Consequently, with $t = L/\bar{U}_2^*$, substitution of eqs. (10.5) and (10.9) into (10.20), together with use of some algebraic manipulations and eq. (10.17), permits the resolution to be expressed as

$$R_s = \frac{1}{2}\left\{\frac{\varepsilon_1 - \varepsilon_2}{n_2^{-1/2}\left(1 + \varepsilon_1\right) + n_1^{-1/2}\left[\left(1 + \varepsilon_1\right)\left(1 + \varepsilon_2\right)\right]^{1/2}}\right\}, \tag{10.21}$$

where, for species i, ε_i and n_i refer respectively to the trapping-to-convection time ratio and the number of theoretical plates. In the large Peclet number limit, $n_1 = n_2 = N$ to

[8]Equation (10.19) represents the most general form of the resolution, rather than the simplified form frequently employed (Giddings 1991), namely $R_s = (n/16)^{1/2}\,\Delta\bar{U}^*/\left\langle \bar{U}^* \right\rangle$, where $\Delta\bar{U}^*$ is the velocity difference between the two species and $\left\langle \bar{U}^* \right\rangle$ is the average velocity. A simplified form of R_s in the large Pe limit is derived subsequently [cf. eq. (10.21)] without invoking the *ad hoc* assumptions necessary to arrive at the usual form for R_s.

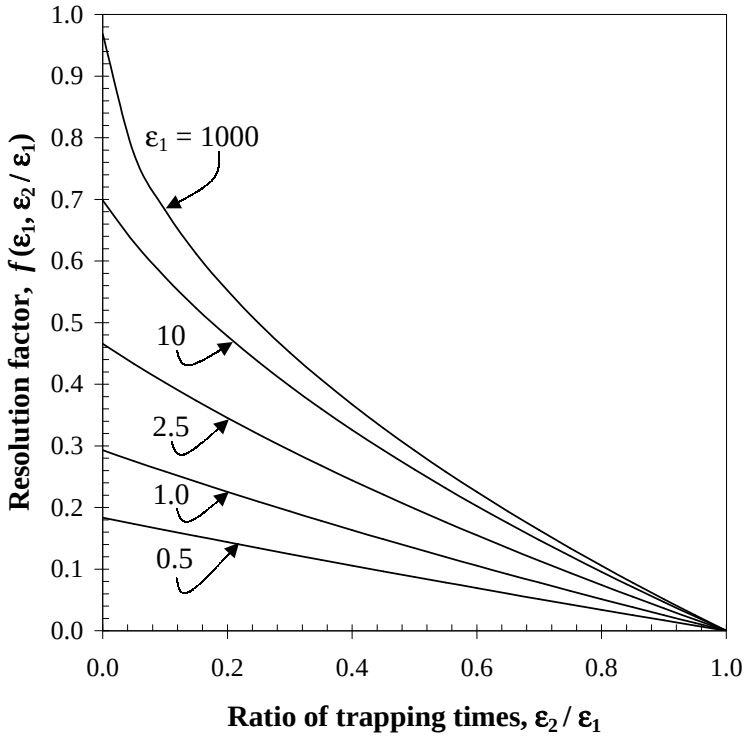

Figure 10-2: Plot of the resolution factor, $f\,(\varepsilon_1, \varepsilon_2/\varepsilon_1)$, as a function of the ratio, $\varepsilon_2/\varepsilon_1$, of the trapping times of the two species being separated, and for several values of the trapping-to-convection ratio, ε_1, of the slower-eluting species.

a satisfactory approximation, whence[9]

$$R_s = \frac{N^{1/2}}{2} f\left(\varepsilon_1, \frac{\varepsilon_2}{\varepsilon_1}\right), \tag{10.22}$$

with f the resolution factor:

$$f\left(\varepsilon_1, \frac{\varepsilon_2}{\varepsilon_1}\right) = \frac{\varepsilon_1\left(1 - \dfrac{\varepsilon_2}{\varepsilon_1}\right)}{(1+\varepsilon_1) + \left\{(1+\varepsilon_1)\left[1 + \varepsilon_1\left(\dfrac{\varepsilon_2}{\varepsilon_1}\right)\right]\right\}^{1/2}}. \tag{10.23}$$

[9]While the parameter ε_1 represents the trapping-to-convection time ratio for species 1, the combination $\varepsilon_2/\varepsilon_1$ is simply the trapping time ratio between species 2 and 1, since it was assumed that the convection time is species-independent.

Figure 10-2 displays f as a function of the ratio $\varepsilon_2/\varepsilon_1$ $(0 \leq \varepsilon_2/\varepsilon_1 \leq 1)$ for several different values of ε_1. Irrespective of the magnitude of ε_1, the resolution factor reduces trivially to $f = 0$ $(R_s = 0)$ when $\varepsilon_1 = \varepsilon_2$, since both solute peaks exit the device at the same time. The resolution increases with increasing ε_1 for all values of $\varepsilon_2/\varepsilon_1$, suggesting an opportunity for device optimization. However, the value of f saturates rapidly, yielding only incremental increases in R_s as ε_1 becomes large, especially as $\varepsilon_2/\varepsilon_1 \to 1$.

Using their approximation for σ (10.12) and an elementary model for the trapping time [cf. eq. (10.25)], Han & Craighead (2002) postulated that the separation resolution would adopt the form

$$R_s = \frac{N^{1/2}}{2}\left(\frac{\Delta N_{bp}}{N_{bp}}\right), \tag{10.24}$$

where ΔN_{bp} is the length difference between the two species being separated and N_{bp} is some characteristic number of base pairs (whereupon the ratio $\Delta N_{bp}/N_{bp}$ represents the fractional length difference). With the latter result, it would be expected that the resolution should only depend upon the total number of traps, being independent of the geometry of these traps and the magnitude of the applied electric field! In contrast, our result for the function f (10.23) possesses an implicit dependence upon the device geometry and the electric field, inasmuch as the trapping times τ_i, and thus ϵ_i, depend upon the latter design parameters. Indeed, the resolution should vanish at high fields since the trapping effect vanishes there (Rousseau *et al.* 1997), i.e. $\epsilon_i = 0\ \forall i$ implies that $R_s = 0$. Our model captures this limiting behavior, since the factor $f = 0$ identically for the case $\epsilon_1 = \epsilon_2$. In contrast, the model of Han & Craighead (2002) does not capture this limiting behavior, or, for that matter, any other structural factors which might contribute to R_s. Moreover, the experimental data (Han & Craighead 2002) indicate a clear dependence upon the field strength E, lending further credence to our discrete Taylor-Aris model of the overall chromatographic phenomenon.

10.3 Comparison with Experimental Results

Below, we compare our macrotransport predictions with the available experimental results of Han & Craighead (2000) for the entropic trapping separation of T2 (164 kbp) and T7 (37.9 kbp) DNA. Table 10.1 summarizes physicochemical data for these two DNA strands. [10] The entropic trapping device employed in these experiments possessed a chip length $L = 7$ mm and trap-to-trap distance $l = 4$ μm, corresponding to $N = 1750$ traps in series. Successful entropic trapping separations were demonstrated at electric field strengths $E = 21.0$ and 24.5 V/cm. Pertinent experimental results (Han & Craighead 2000) for these values of E are recast into our formalism in Table 10.2.

The relative importance of molecular diffusion and random trapping times upon $\bar{D}^*$ is captured in the present model by the Peclet number. Explicitly, variations in τ dominate the dispersion when $\mathrm{Pe} \gg 1$, whereas molecular diffusion dominates when $\mathrm{Pe} \ll 1$. Table 10.2 shows the relevant Peclet numbers characterizing the experimental systems studied to be large, thereby implicitly confirming the conjecture of Han & Craighead (2000) that variations in trapping times constitute the primary dispersion mechanism.

To render transparent the dependence of the dispersivity upon the field strength E (and thereby the trapping time τ), it is necessary to employ a microscale model for τ. In this context, consider the following simple model proposed by Han *et al.* (1999):

$$\tau = \tau^* \exp\left[\frac{\alpha}{EkT}\right], \tag{10.25}$$

where τ^* and α are species-specific constants, and kT is the Boltzmann factor. For the class of separations of interest, the functional form of eq. (10.25) agrees with the available experimental data of Han *et al.* (1999). In light of the fact that $\mathrm{Pe} \gg 1$ and $\varepsilon \gg 1$, the

[10] The number of persistence lengths may be different for DNA stained with intercalator dyes. For example, lambda phage DNA (48.5 kbp) stained with YOYO-1 has approximately 400 persistence lengths. Nevertheless, the results presented herein are relatively insensitive to this parameter.

Table 10.1: Physicochemical properties and transport parameters for T2 and T7 DNA. References: [1] Han & Craighead 2000, [2] Lehninger *et al.* 1993, [3] Volkmuth *et al.* 1994, [4] Ertas 1998.

	T2	T7	Ref.
Number of base pairs (kbp)	164	37.9	[1]
Number of persistence lengths	469	108	[2]
Zimm diffusion coefficient, D ($\mu\mathrm{m}^2\mathrm{s}^{-1}$)	0.370	0.769	[3,4]
Electrophoretic mobility, μ_0 ($\mu\mathrm{m\,s}^{-1}\mathrm{cm\,V}^{-1}$)	5.1	5.1	[3]

Table 10.2: Experimental parameters for the entropic separation of T2 and T7 DNA. Reference: [1] Han & Craighead 2000.

	T2		T7		Ref.
Electric field, E (V/cm)	21.0	24.5	21.0	24.5	[1]
Peclet number, Pe	1160	1360	560	650	Eq. (10.10)
Retention time, t_R (s)	1375	950	1700	1100	[1]
Trapping-to-convection time ratio, ε	20	16	25	19	Eq. (10.8)

dispersivity may be approximated as

$$\bar{D}^* \approx D\frac{\mathrm{Pe}}{2\varepsilon}. \tag{10.26}$$

With use of eqs. (10.6), (10.10) and (10.25), eq. (10.26) becomes

$$\bar{D}^* \approx \frac{l^2}{2\tau^*}\exp\left(-\frac{\alpha}{EkT}\right), \tag{10.27}$$

whence the dispersivity increases with increasing field strength.

For such large Peclet number transport, eq. (10.18) reveals that each trap approximates a single theoretical plate.[11] The latter conclusion agrees, as regards order-of-magnitude, with the reported experimental values of Han & Craighead (2000), with n varying between 10^3 and 10^4 for $N = 1750$. However, the present model fails to predict a reported (Han & Craighead 2000) dependence of n upon E and τ in the large Pe limit. This functional dependence might arise from the detailed local transport proper-

[11]For the smallest Peclet number experimentally encountered, namely Pe = 560, the relative error between the exact result (10.17) and the approximation (10.18) is only 0.35%.

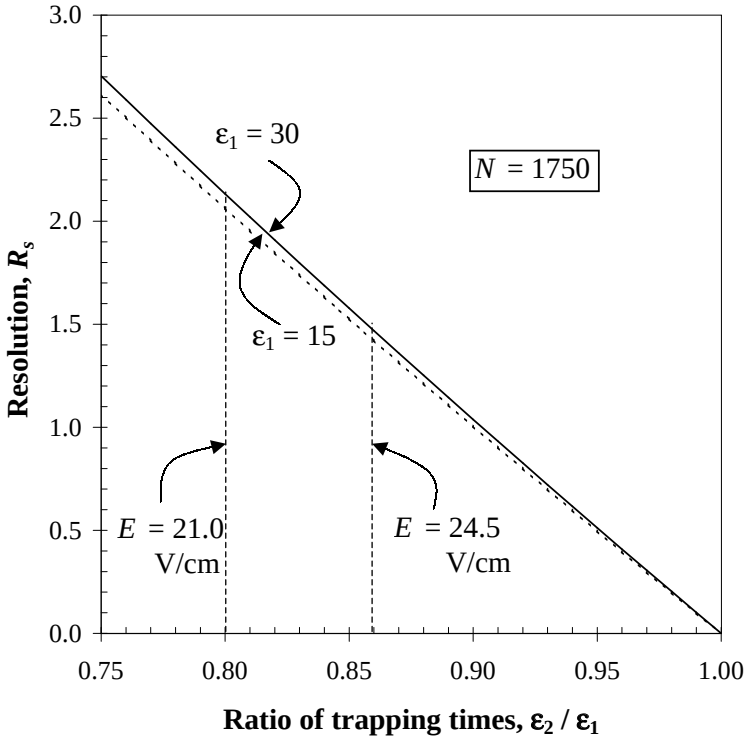

Figure 10-3: Plot of the resolution, R_s, for a device with $N = 1750$ traps as a function of the ratio, $\varepsilon_2/\varepsilon_1$, of trapping times between the two species being separated, and for two values of the trapping-to-convection time ratio, ε_1, of the slower-eluting species. The values of $\varepsilon_2/\varepsilon_1$ observed experimentally at field strengths of 21.0 and 24.5 V/cm are indicated by the vertical lines.

ties of DNA, including position-dependent effects owing to the molecule's proximity to the bounding walls, such effects arising on a length scale far smaller than the class of phenomena addressed in our model. On the other hand, the observed variations in n might simply reflect statistical variations occurring between replicate experiments, which might be expected when considering the nanometer scales involved in these experiments. Moreover, practical experimental constraints required sample loading over a single period of the device (Han & Craighead 2000), whereas our theoretical model is based upon a unit pulse input [cf. eq. (4.6)].

Upon decreasing the electric field strength, Han & Craighead (2000) observed that

the separation resolution increased. Substituting the relevant parameters appearing in Table 10.2 into eq. (10.21), and identifying T2 DNA as species 2, yields theoretical resolutions of $R_s = 2.10$ at $E = 21.0$ V/cm and $R_s = 1.48$ at $E = 24.5$ V/cm. Aside from capturing the aforementioned resolution trend, qualitative agreement is found with reported experimental values of $R_s = 1.95$ and $R_s = 0.89$ at $E = 21.0$ and 24.5 V/cm, respectively. However, our theoretical results are especially sensitive to the ratio $\varepsilon_2/\varepsilon_1$, the latter having been estimated here from a published fluorescence intensity plot (Han & Craighead 2000). Explicitly, consider the plot in Fig. 10-3 of R_s as a function of $\varepsilon_2/\varepsilon_1$. The two curves depicted, corresponding to $\varepsilon_1 = 15$ and 30, bound the experimental values, $\varepsilon_1 = 19$ and 25, for T7 DNA. Precise measurement of the magnitude of ε_1 is unnecessary, given the negligible effect upon R_s of doubling ε_1 in this parameter range; rather, it is the precise determination of the $\varepsilon_2/\varepsilon_1$ ratio which proves crucial, since the experimental values, $\varepsilon_2/\varepsilon_1 = 0.80$ and 0.86, approach the zero resolution limit, $\varepsilon_2/\varepsilon_1 \to 1$. Consequently, our quantitative agreement for R_s is tenuous at best, since it is formed from the product of an unequivocal large number, $N^{1/2}/2 \gg 1$, with a more equivocal small number, $f(\varepsilon_1, \varepsilon_2/\varepsilon_1 \to 1) \ll 1$. The validity (or lack thereof) of our predictions for R_s may be assessed more clearly as further experimental data become available pertinent to this novel separation process which allow values for ε_1 and ε_2 to be established under various operating conditions.

In rationalizing the increased resolution observed at the lower field strengths, Han & Craighead (2000) point out that the increased velocity difference, $\left|\bar{U}_2^* - \bar{U}_1^*\right|$, more than offsets an apparent increase in band broadening (10.11) at the elution time, t_R. The latter observation of increased band broadening, in conjunction with our macrotransport analysis, establishes a theoretical upper bound on the empirical parameter α appearing in eq. (10.25). Consider a pair of experiments performed in identical devices with identical DNA strands, but with different electric field strengths, E_1 and E_2 ($E_1 > E_2$), and correspondingly different holdup times, $t_{R,1}$ and $t_{R,2}$ ($t_{R,2} > t_{R,1}$). Assuming τ^* to

be independent of E, this yields the expression

$$\frac{\sigma_1}{\sigma_2} = \sqrt{\exp\left[\frac{\alpha}{kT}\left(\frac{1}{E_2} - \frac{1}{E_1}\right)\right]\left(\frac{t_{R,1}}{t_{R,2}}\right)}. \tag{10.28}$$

In conjunction with the requisite inequality $\sigma_1 < \sigma_2$, it follows that the empirical parameter α is bounded from above by the expression

$$\alpha < \left[kT \ln\left(\frac{t_{R,2}}{t_{R,1}}\right)\right]\left(\frac{1}{E_2} - \frac{1}{E_1}\right)^{-1}. \tag{10.29}$$

With the retention times appearing in Table 10.2, the preceding relation furnishes the inequality $\alpha < 1.40$ eV(V/cm) for T2 DNA and $\alpha < 1.65$ eV(V/cm) for T7 DNA at $T = 298$ K. If one accepts the premise (Han & Craighead 2002) that the parameter α is DNA-length independent, then our analysis furnishes the inequality $\alpha < 1.40$ eV(V/cm).

10.4 Concluding Remarks

Apart from the chromatographic separation applications outlined above, the analysis presented herein is potentially useful in studying the fundamental mechanism of entropic trapping. Our macrotransport analysis embodies *average* transport rates, which prevail only after the macromolecule has had the opportunity to thoroughly sample numerous traps. Consequently, statistical issues arising from single trapping experiments become irrelevant. Although eq. (10.8) provides the most straightforward, long-time metric for experimental validation of proposed microscale models of entropic trapping, our expressions for the functional dependencies of $\bar{D}^*$, n and R_s upon the pertinent experimental parameters provide a trio of internal consistency checks for such models. For example, the separation resolution (10.21) requires knowledge of the respective trapping times of two different length polymer chains, thereby providing a criterion for establishing the correctness of the scaling proposed by a microscale model within the context of a single experiment. Moreover, our theoretical upper bound on the magnitude of the empiri-

cal parameter α constitutes a further contribution of our coarse-grained model to the development of a rational microscale theory of entropic trapping.

The model of entropic trapping phenomena pursued here considers only the simplest possible network configuration for correlating the experiments of Han & Craighead (2000). A somewhat more general one-dimensional network model, based upon a distribution of trapping times, rather than a single average time, could potentially furnish even more accurate agreement with experiments, while retaining the analytical simplicity of a lumped-parameter model. Explicitly, consider a unit cell comprised of j traps, each trap being characterized by its own specific trapping time, τ_j, with such times being chosen at random from a distribution about a mean value τ. Presumably more accurate values for $\bar{U}^*$ and $\bar{D}^*$ would arise upon averaging the values $\bar{U}_k^*$ and $\bar{D}_k^*$ computed from k different unit cell configurations. At present, no rational basis exists for specifying a complete probability distribution for these times τ_j, thereby motivating our more elementary use of a single average value, τ. Results for *ad hoc* trapping time distributions, using appropriate parameters fitted from data, could be employed in this extended model, and subsequently compared with experimental results to furnish insights into the validity of such distributions.

Our model bears a peripheral relation to the so-called molecular dynamic (or kinetic) theory of chromatography (Giddings & Eyring 1955). That theory assumes the polymer molecule to exist in either an entangled (immobile) or untangled (mobile) state at each instant of time, with first-order kinetics governing state-to-state transitions. Experiments and simple analysis (Weiss *et al.* 1996, Yarmola *et al.* 1997) suggest that the non-Markovian nature of this transition process leads to anomalous diffusion in gels, although more recent work (Boguna *et al.* 2000) formally demonstrates that the probability density for such two-state models still tends asymptotically towards Gaussian behavior after the elapse of sufficient time. While the method-of-moments homogenization scheme employed in this thesis permits anomalous diffusion under well-defined circumstances (Bryden & Brenner 1996, Stone & Brenner 1999), an explanation of such

circumstances lies outside the scope of the present study. However, our global transport model is unlikely to exhibit such anomalous behavior under *any* homogenization scheme, since: (i) the vertex transport process is Markovian (Sahimi *et al.* 1983); (ii) the transition between states occurs at distinct points in space; and (iii) the first two moments of τ are bounded. Indeed, the network dispersion model considered herein could be extended to a two-dimensional, random network of traps and channels, thereby furnishing an elementary (non-kinetic) model for gel electrophoresis.

Chapter 11

Conclusion

While the generic discrete theory developed in this thesis is predicated upon the same rigorous method-of-moments homogenization scheme as was employed in continuous generalized Taylor-Aris dispersion theory when applied to spatially periodic media (Brenner 1980, Brenner & Edwards 1993), our analysis has demonstrated the greater tractability of discrete network theory over its continuous counterpart (Brenner & Edwards 1993) (the former approach being, albeit, more approximate). In the continuous theory, both the array geometry and interstitial transport physics are presumed to be known *exactly*, thereby rendering the computed macrotransport parameters $\bar{\mathbf{U}}^*$ and $\bar{\mathbf{D}}^*$ physically accurate and mathematically rigorous, at least in an asymptotic sense. Such rigor comes, however, at the expense of requiring the solution of two steady-state convection-diffusion(-reaction) partial differential equations for the continuous macrotransport fields $P_0^\infty(\mathbf{r})$ and $\mathbf{B}(\mathbf{r})$ at all interstitial unit cell points $\mathbf{r}$ (Brenner & Edwards 1993), as well as demanding precise and explicit knowledge of the phenomenological coefficients quantifying the l-scale interstitial transport processes. With the exception of but a few limiting cases, such phenomenological data are generally unavailable in the literature; even when such data are available, or calculable in principle for simple bodies such as rigid spheres, an accurate quantification of the interstitial transport physics is often nonexistent for deformable bodies (e.g. freely-draining DNA or polymer molecules). Moreover, the structure of the

governing equations renders such equations insoluble in closed-form for all but the most trivial of array geometries — even the simple networks analyzed in Chapter 9 and 10. Furthermore, the continuous theory's requisite unit cell quadratures cannot generally be effected in closed form (Dorfman & Brenner 2001), even for those rare circumstances for which closed-form solutions exist for the macrotransport fields $P_0^\infty(\mathbf{r})$ and $\mathbf{B}(\mathbf{r})$ themselves appearing in the integrands of the requisite integrals.

The comments of the preceding paragraph point out that the resources required to extract useful macroscale information from the continuous microscale theory diminish the utility of such an approach, owing not only to the unavailability of pertinent transport data, but equally to the computational effort required and concomitant errors introduced via numerical discretization of the local-scale transport parameters. Indeed, in the latter context, similarities existing between finite-difference methods for solving partial differential equations and network models have been recognized for at least 30 years (Kirkpatrick 1973), inasmuch as the desired degree of accuracy inherent in any finite-difference scheme necessitates a lumped parameter approach on the scale of the discretization. Of course, the tractability of the discrete scheme presented here arises as a consequence of the *a priori* homogenization of the exact local-scale transport into the lumped-parameter edge transport coefficients $U(j)$, $D(j)$, and $K(j)$. While asymptotic definitions exist for the latter parameters under certain limiting circumstances, one cannot hope to rigorously retain the full extent of the true local-scale transport description — in particular the complex geometry of even a well-defined, spatially periodic model porous medium. Nevertheless, the counterbalance existing between comparable approximations necessary for either a continuous or discrete model render the latter attractive for the characterization of macromolecular transport in microfluidic devices.

Bibliography

P. M. Adler and H. Brenner, *Transport processes in spatially periodic capillary networks. I. Geometrical description and linear flow hydrodynamics*, PhysicoChem. Hydrodyn., 5 (1984a), pp. 245–268.

——, *Transport processes in spatially periodic capillary networks. II. Taylor dispersion with mixing vertices*, PhysicoChem. Hydrodyn., 5 (1984b), pp. 269–285.

——, *Transport processes in spatially periodic capillary networks. III. Nonlinear flow problems*, PhysicoChem. Hydrodyn., 5 (1984c), pp. 287–297.

P. M. Adler, *Transport processes in fractals. 2. Stokes-flow in fractal capillary networks*, Int. J. Multiph. Flow, 11 (1985a), pp. 213–239.

——, *Transport processes in fractals. 3. Taylor dispersion in 2 examples of fractal capillary networks*, Int. J. Multiph. Flow, 11 (1985b), pp. 241–254.

——, *Transport processes in fractals. 4. Nonlinear flow problems in fractal capillary networks*, Int. J. Multiph. Flow, 11 (1985c), pp. 853–871.

V. Alvarado, H. T. Davis, and L. E. Scriven, *Effects of pore-level reaction on dispersion in porous media*, Chem. Eng. Sci., 52 (1997), pp. 2865–2881.

J. S. Andrade, D. A. Street, Y. Shibusa, S. Havlin, and H. E. Stanley, *Diffusion and reaction in percolating pore networks*, Phys. Rev. E, 55 (1997), pp. 772–777.

J. S. Andrade Jr., K. Rajagopal, and C. McGreavy, *Chromatography in pore networks II - The role of structure and adsorption in the band broadening*, Chromatographia, 32 (1992), pp. 345–349.

E. Arvanitidou and D. A. Hoagland, *Chain-length dependence of the electrophoretic mobility in random gels*, Phys. Rev. Lett., 67 (1991), pp. 1464–1466.

B. E. Aviles and M. D. Levan, *Network models for nonuniform flow and adsorption in fixed beds*, Chem. Eng. Sci., 46 (1991), pp. 1935–1944.

V. Balakotaiah and S. M. S. Dommeti, *Effective models for packed-bed catalytic reactors*, Chem. Eng. Sci., 54 (1999), pp. 1621–1638.

R. P. Batycky, D. A. Edwards, and H. Brenner, *On the need for fictitious initial conditions in effective medium theories of transient nonconservative transport phenomena. Some elementary unsteady-state heat conduction examples*, Chem. Eng. Comm., 152-153 (1996), pp. 173–187.

J. Bear, *Dynamics of Fluids in Porous Media*, Elsevier, New York, 1972.

C. Berge, *Graphs and Hypergraphs*, American Elsevier, New York, 1973.

B. Berkowitz and R. P. Ewing, *Percolation theory and network modeling applications in soil physics*, Surveys in Geophysics, 19 (1998), pp. 23–72.

A. R. Billings, *Tensor Properties of Materials*, Wiley-Interscience, New York, 1969.

R. B. Bird, C. F. Curtiss, R. C. Armstrong, and O. Hassager, *Dynamics of Polymeric Liquids, Vol. II*, Wiley, New York, 1987.

M. Boguna, A. M. Berezhkovskii, and G. H. Weiss, *Residence time densities for non-Markovian systems. (I). The two-state system*, Physica A, 282 (2000), pp. 475–485.

B. Bollobas, *Graph Theory: An Introductory Course*, Springer-Verlag, New York, 1979.

H. Brenner, *Dispersion resulting from flow through spatially periodic media*, Phil. Trans. Roy. Soc. (London) Ser. A., 297 (1980), pp. 81–133.

——, *Macrotransport processes: Brownian particles as stochastic averagers in effective-medium theories of heterogeneous media*, J. Stat. Phys., 62 (1991), pp. 1095–1119.

H. Brenner and P. M. Adler, *Dispersion resulting from the flow through spatially periodic porous media. II. Surface and intraparticle transport*, Phil. Trans. Roy. Soc. (London) Ser. A., 307 (1982), pp. 149–200.

H. Brenner and D. A. Edwards, *Macrotransport Processes*, Butterworth-Heinemann, Boston, 1993.

H. Brenner and L. J. Gaydos, *The constrained Brownian movement of spherical particles in cylindrical pores of comparable radius: Models of the diffusive and convective transport of solute particles in membranes and porous media*, J. Colloid Interface Sci., 58 (1977), pp. 312–356.

C. Bruderer and Y. Bernabe, *Network modeling of dispersion: Transition from Taylor dispersion in homogeneous networks to mechanical dispersion in very heterogeneous ones*, Water Resour. Res., 37 (2001), pp. 897–908.

M. D. Bryden and H. Brenner, *Multiple-timescale analysis of Taylor dispersion in converging and diverging flows*, J. Fluid Mech., 311 (1996), pp. 343–359.

C. F. Chou, O. Bakajin, S. W.P. Turner, T. Duke, S. S. Chan, E. C. Cox, H. G. Craighead, and R. H. Austin, *Sorting by diffusion: An asymmetric obstacle course for continuous molecular separation*, Proc. Natl. Acad. Sci. U.S.A, 96 (1999), pp. 13762–13765.

C. F. Chou, R. H. Austin, O. Bakajin, J. O. Tegenfeldt, J. A. Castelino, S. S. Chan, E. C. Cox, H. G. Craighead, N. Darnton, T. Duke, J. Han,

and S. W.P. Turner, *Sorting biomolecules with microdevices*, Electrophoresis, 21 (2000), pp. 81–90.

R. I. Cukier, *Diffusion controlled processes among stationary reactive sinks: Effective medium approach*, J. Chem. Phys., 78 (1983a), pp. 2573–2578.

——, *Effective medium theory of rate processes among stationary reactive sinks with the radiation boundary condition*, J. Phys. Chem., 87 (1983b), pp. 582–586.

C. T. Culbertson, S. C. Jacobson, and J. M. Ramsey, *Dispersion sources for compact geometries on microchips*, Anal. Chem., 70 (1998), pp. 3781–3789.

L. de Arcangelis, J. Koplik, S. Redner, and D. Wilkinson, *Hydrodynamic dispersion in network models of porous media*, Phys. Rev. Lett., 57 (1986), pp. 996–999.

W. M. Deen, *Hindered transport of large molecules in liquid-filled pores*, AIChE J., 33 (1987), pp. 1409–1425.

E. A. DiMarzio and C. M. Guttman, *Separation by flow*, Macromolecules, 3 (1970), pp. 131–146.

K. D. Dorfman and H. Brenner, *'Vector chromatography:' Modeling micropatterned chromatographic separation devices*, J. Colloid Interface Sci., 238 (2001), pp. 390–413.

——, *Generalized Taylor-Aris dispersion in discrete spatially periodic networks. Microfluidic applications*, Phys. Rev. E, 65 (2002a), p. 021103.

——, *Modeling DNA electrophoresis in microfluidic entropic trapping devices*, Biomed. Microdev., 4 (2002b), pp. 235–242.

——, *Separation mechanisms underlying vector chromatography in microlithographic arrays*, Phys. Rev. E, 65 (2002c), p. 052103.

——, *Generalized Taylor-Aris dispersion in spatially periodic microfluidic networks. Chemical reactions*, SIAM J. Appl. Math, (submitted, 2002d).

P. S. Doyle, J. Bibette, A. Bancaud, and J. L. Viovy, *Self assembled magnetic matrices for DNA separation chips*, Science, 295 (2002), p. 2237.

T. A. J. Duke and R. H. Austin, *Microfabricated sieve for the continuous sorting of macromolecules*, Phys. Rev. Lett., 80 (1998), pp. 1552–1555.

T. Duke, G. Monnelly, R. H. Austin, and E. C. Cox, *Sequencing in nanofabricated arrays: A feasibility study*, Electrophoresis, 18 (1997), pp. 17–22.

S. R. Dungan, M. Shapiro, and H. Brenner, *Convective-diffusive-reactive Taylor dispersion processes in particulate multiphase systems*, Proc. Roy. Soc. A, 429 (1990), pp. 639–671.

D. A. Edwards, M. Shapiro, and H. Brenner, *Dispersion and reaction in two-dimensional model porous media*, Phys. Fluids A., 5 (1993), pp. 837–848.

D. Ertas, *Lateral separation of macromolecules and polyelectrolytes in microlithographic arrays*, Phys. Rev. Lett., 80 (1998), pp. 1548–1551.

I. Fatt, *The network model of porous media. II. Dynamic properties of a single size tube network*, Trans. AIME, 207 (1956), pp. 160–163.

V. Ganesan, *Applications of Coarse Graining Approaches: Volume Averaging, Macrotransport Theory and Scaling Concepts*, Ph.D. Thesis, Massachusetts Institute of Technology, Cambridge, MA (1999).

J. C. Giddings, *Unified Separation Science*, Wiley and Sons, New York, 1991.

J. C. Giddings and H. Eyring, *A molecular dynamic theory of chromatography*, J. Phys. Chem., 59 (1955), pp. 416–421.

T. R. Ginn, *Stochastic-convective transport with nonlinear reactions and mixing: Finite streamtube ensemble formulation for multicomponent reaction systems with intra-streamtube dispersion*, J. Contam. Hydrol., 47 (2001), pp. 1–28.

J. Han and H. G. Craighead, *Entropic trapping and sieving of long DNA molecules in a nanofluidic channel*, J. Vac. Sci. Technol. A-Vac. Surf. Films, 17 (1999), pp. 2142–2147.

J. Han and H. G. Craighead, *Separation of long DNA molecules in microfabricated entropic trap arrays*, Science, 288 (2000), pp. 1026–1029.

J. Han and H. G. Craighead, *Characterization and optimization of an entropic trap for DNA separation*, Anal. Chem., 74 (2002), pp. 394–401.

J. Han, S. W. Turner, and H. G. Craighead, *Entropic trapping and escape of long DNA molecules at submicron size constriction*, Phys. Rev. Lett., 83 (1999), pp. 1688–1691.

J. Happel and H. Brenner, *Low Reynolds Number Hydrodynamics*, Kluwer Academic, Netherlands, 1983.

M. P. Hollewand and L. F. Gladden, *Modeling of diffusion and reaction in porous catalysts using a random 3-dimensional network model*, Chem. Eng. Sci., 47 (1992), pp. 1761–1770.

A. O. Imdakm and M. Sahimi, *Computer simulation of particle transport processes in flow through porous media*, Chem. Eng. Sci., 46 (1991), pp. 1977–1993.

G. Iosilevskii and H. Brenner, *Taylor dispersion in discrete reactive mixtures*, Chem. Eng. Commun., 133 (1995), pp. 53–91.

S. C. Jakeway, A. J. de Mello, and E. L. Russell, *Miniaturized total analysis systems for biological analysis*, Fresenius J. Anal. Chem., 366 (2000), pp. 525–539.

R. M. Jendrejack, M. D. Graham, and J. J. DePablo, *Hydrodynamic interactions in long chain polymers: Application of the Chebyshev polynomial approximation in stochastic simulations*, J. Chem. Phys., 113 (2000), pp. 2894–2900.

K. F. Jensen, *Microreaction engineering — Is smaller better?*, Chem. Eng. Sci., 56 (2001), pp. 293–303.

S. Kim and S. J. Karrila, *Microhydrodynamics: Principles and Selected Applications*, Butterworth-Heinemann, Boston, 1991.

S. Kirkpatrick, *Percolation and conduction*, Rev. Mod. Phys., 45 (1973), pp. 574–588.

D. L. Koch and J. F. Brady, *Dispersion in fixed-beds*, J. Fluid Mech., 154 (1985), pp. 399–427.

J. Koplik, *Creeping flow in two-dimensional networks*, J. Fluid Mech., 119 (1982), pp. 219–247.

J. Koplik, S. Redner, and D. Wilkinson, *Transport and dispersion in random networks with percolation disorder*, Phys. Rev. A, 37 (1988), pp. 2619–2636.

M. Krishnan, V. Namasivayam, R. S. Lin, R. Pal, and M. A. Burns, *Microfabricated reaction and separation systems*, Curr. Opin. Biotechnol., 12 (2001), pp. 92–98.

J. Kruger, *Effective medium theory for diffusion-controlled reactions among stationary perfect sinks*, Physica A, 166 (1990a), pp. 206–219.

——, *Effective medium theory of diffusion and chemical-reaction in the presence of stationary sinks*, Physica A, 169 (1990b), pp. 393–406.

J. P. Kutter, *Current developments in electrophoretic and chromatographic separation methods on microfabricated devices*, Trac-Trends Anal. Chem., 19 (2000), pp. 352–363.

J. Lee and J. Koplik, *Microscopic motion of particles flowing through a porous media*, Phys. Fluids, 11 (1999), pp. 76–87.

A. L. Lehninger, D. L. Nelson, and M. M. Cox, *Principles of Biochemistry*, Worth Publishers, New York, 1993.

M. Leitzelement, P. Maj, J. A. Dodds, and J. L. Greffe, *Deep bed filtration in a network of random tubes*, in Solid-Liquid Separation, J. Gregory, ed., Ellis Horwood, Chichester, U.K., 1984, pp. 273–296.

G. Y. Li and H. Rabitz, *A general lumping analysis of a reaction system coupled with diffusion*, Chem. Eng. Sci., 46 (1991), pp. 2041–2053.

L. Liu, P. S. Li, and S. A. Asher, *Entropic trapping of macromolecules by mesoscopic periodic voids in a polymer hydrogel*, Nature, 397 (1999), pp. 141–144.

K. Mattern and B. U. Felderhof, *Rate of diffusion-controlled reactions in a random array of spherical sinks*, Physica A, 143 (1987), pp. 1–20.

R. Mauri, *Dispersion, convection, and reaction in porous-media*, Phys. Fluids, 3 (1991), pp. 743–756.

C. McGreavy, J. S. Andrade Jr., and K. Rajagopal, *Size exclusion chromatography in pore networks*, Chromatographia, 30 (1990), pp. 639–644.

K. N. Mehta, M. C. Tiwari, and K. D. P. Nigam, *Effect of permeability and chemical-reaction on laminar dispersion of a solute*, Int. J. Eng. Fluid Mech., 1 (1988), pp. 351–364.

J. J. Meyers and A. I. Liapis, *Network modeling of the intraparticle convection and diffusion of molecules in porous particles packed in a chromatographic column*, J. Chromatogr. A, 827 (1998), pp. 197–213.

M. Muthukumar, *Concentration dependence of diffusion controlled processes among static traps*, J. Chem. Phys., 76 (1982), pp. 2667–2671.

M. Muthukumar and A. Baumgartner, *Diffusion of a polymer chain in random media*, Macromolecules, 22 (1989a), pp. 1941–1946.

——, *Effects of entropic barriers on polymer dynamics*, Macromolecules, 22 (1989b), pp. 1937–1941.

J. M. Nitsche and H. Brenner, *Sedimentation and dispersion of Brownian particles in spatially periodic potential fields*, J. Chem. Phys., 89 (1998), pp. 7510-7520.

G. I. Nixon and G. W. Slater, *Entropic trapping and electrophoretic drift of a polyelectrolyte down a channel with a periodically oscillating width*, Phys. Rev. E, 53 (1996), pp. 4969–4980.

M. Pagitsas, A. Nadim, and H. Brenner, *Multiple time scale analysis of macro-transport processes*, Physica A, 135A (1986), pp. 533–550.

D. Pal, *Effect of chemical reaction on the dispersion of a solute in a porous medium*, Appl. Math. Model., 23 (1999), pp. 557–566.

S. H. Park and Y. G. Kim, *The effect of chemical-reaction on effective diffusivity within biporous catalysts. 1. Theoretical development*, Chem. Eng. Sci., 39 (1984), pp. 523–531.

S. D. Rege and H. S. Fogler, *A network model for deep bed filtration of solid particles and emulsion drops*, AIChE J., 34 (1988), pp. 1761–1772.

J. Rousseau, G. Drouin, and G. W. Slater, *Entropic trapping of DNA during gel electrophoresis: Effect of field intensity and gel concentration*, Phys. Rev. Lett., 79 (1997), pp. 1945–1948.

B. M. Rush, K. D. Dorfman, H. Brenner, and S. Kim, *Dispersion by pressure-driven flow in serpentine microfluidic channels*, Ind. Eng. Chem. Res., (submitted, 2002).

W. B. Russel, D.A. Saville, and W.R. Showalter, *Colloidal Dispersions*, Cambridge University Press, Cambridge, 1989.

D. Ryan, R. G. Carbonell, and S. Whitaker, *Effective diffusivities for catalyst pellets under reactive conditions*, Chem. Eng. Sci., 35 (1980), pp. 10–16.

P. G. Saffman, *A theory of dispersion in a porous medium*, J. Fluid Mech., 6 (1959), pp. 321–349.

M. Sahimi, *Transport of macromolecules in porous media*, J. Chem. Phys., 96 (1992), pp. 4718–4728.

M. Sahimi, H. T. Davis, and L. E. Scriven, *Dispersion in disordered porous media*, Chem. Eng. Comm., 23 (1983), pp. 329–341.

M. Sahimi, G. R. Gavalas, and T. T. Tsotsis, *Statistical and continuum models of fluid-solid reactions in porous media*, Chem. Eng. Sci., 45 (1990), pp. 1443–1502.

M. Sahimi and V. L. Jue, *Diffusion of large molecules in porous media*, Phys. Rev. Lett., 62 (1989), pp. 629–632.

M. Shapiro and H. Brenner, *Taylor dispersion of chemically reactive species: Irreversible first-order reactions in bulk and on boundaries*, Chem. Eng. Sci., 41 (1986), pp. 1417–1433.

——, *Chemically reactive generalized Taylor dispersion phenomena*, AIChE J., 33 (1987), pp. 1155–1167.

——, *Dispersion of a chemically reactive solute in a spatially periodic model of a porous medium*, Chem. Eng. Sci., 43 (1988), pp. 551–571.

G. W. Slater and S. Y. Wu, *Reptation, entropic trapping, percolation, and Rouse dynamics of polymers in "random" environments*, Phys. Rev. Lett., 75 (1995), pp. 164–167.

G. W. Slater, T. B. L. Kist, H. J. Ren, and G. Drouin, *Recent developments in DNA electrophoretic separations*, Electrophoresis, 19 (1998), pp. 1525–1541.

D. L. Smisek and D. A. Hoagland, *Electrophoresis of flexible macromolecules: Evidence for a new mode of transport in gels*, Science, 248 (1990), pp. 1221–1223.

K. S. Sorbie and P. J. Clifford, *The inclusion of molecular diffusion effects in the network modeling of hydrodynamic dispersion in porous media*, Chem. Eng. Sci., 46 (1991), pp. 2525–2542.

H. A. Stone and H. Brenner, *Dispersion in flows with streamwise variations of mean velocity: Radial flow*, Ind. Eng. Chem. Res., 38 (1999), pp. 851–854.

B. J. Suchomel, B. M. Chen, and M. B. Allen, *Network model of flow, transport and biofilm effects in porous media*, Transp. Porous Media, 30 (1998), pp. 1–23.

G. I. Taylor, *Dispersion of soluble matter in solvent flowing slowly through a tube*, Proc. Roy. Soc., A219 (1953), pp. 186–203.

J. van Brakel, *Pore space models for transport phenomena in porous media: Review and evaluation with special emphasis on capillary liquid transport*, Powder Tech., 11 (1975), pp. 205–236.

N. G. van Kampen, *Stochastic Processes in Physics and Chemistry*, North-Holland, New York, 1981.

W. D. Volkmuth, T. Duke, M. C. Wu, R. H. Austin, and A. Szabo, *DNA electrodiffusion in a 2D array of posts*, Phys. Rev. Lett., 72 (1994), pp. 2117–2120.

N. Wakad and Y. Nardse, *Effective diffusivities and deadend pores*, Chem. Eng. Sci., 29 (1973), pp. 1304–1306.

G. H. Weiss, *Aspects and Applications of The Random Walk*, North-Holland, New York, 1994.

G. H. Weiss, H. Sokoloff, S. F. Zakharov, and A. Chrambach, *Interpretation of electrophoretic band shapes by a partition chromatographic model*, Electrophoresis, 17 (1996), pp. 1325–1332.

Z. Y. Yan, A. Acrivos, and S. Weinbaum, *Fluid skimming and particle entrainment into a small circular side pore*, J. Fluid Mech., 229 (1991), pp. 1–27.

E. Yarmola, P. P. Calabrese, A. Chrambach, and G. H. Weiss, *Interaction with the matrix: The dominant factor in macromolecular band spreading in gel electrophoresis*, J. Phys. Chem. B, 101 (1997), pp. 2381–2387.

L. Zhang and N. A. Seaton, *The application of continuum equations to diffusion and reaction in pore networks*, Chem. Eng. Sci., 49 (1994), pp. 41–50.

Appendix A

Nomenclature

A.1 Scalars

A.1.1 Roman

$A(i)$	fictitious initial condition (discrete)
$A(\mathbf{r})$	fictitious initial condition (continuous)
$A(j)$	characteristic edge cross-sectional area
a, b, c	subvolume element labels
$c(j)$	edge convective flow rate
$d(j)$	edge diffusive flow rate
d_x	serpentine channel x-direction diffusive flow rate
d_y	serpentine channel y-direction diffusive flow rate
$D(j)$	edge diffusivity/dispersivity
D_m	solute molecular diffusivity
$\bar{D}^*$	solute dispersivity
$\hat{D}^*$	normalized solute dispersivity
Da	Damkohler number

$\overline{\mathrm{Da}}$	macroscopic Damkohler number
E	magnitude of the applied electric field
exp	exponentially small terms
f	resolution factor
F	magnitude of the applied force
H	channel cross-section height
H_p	theoretical plate height
i	node (vertex) index
i^*	reference node
i_0	initial node
I	discrete location
j	edge index
$k(i)$	discrete local reaction rate
$K(j)$	edge mixing rule
$\bar{K}_0$	smallest eigenvalue
$\bar{K}_1$	second smallest eigenvalue
$\bar{K}_A$	eigenvalue of the $A(i)$ equations
$\bar{K}_P$	eigenvalue of the $P_0^\infty(i)$ equations
$\bar{K}^*$	mean (network-scale) solute depletion rate
kT	Boltzmann factor
l	characteristic local length scale
$l(j)$	edge length
l_s	channel arclength
l_X	serpentine jump distance
L	characteristic global length scale
m	number of edges

m_b	number of edges in the basic graph
M_{0r}	solute survival probability density
$\bar{M}_j^*$	mean mobility in channel j
n	number of nodes (the number of theoretical plates in Chapter 10)
n_b	number of nodes in the basic graph
N	total number of unit cells
N_{bp}	number of base pairs
ΔN_{bp}	difference in number of base pairs
P	non-reactive probability density
$\bar{P}$	coarse-grained probability density
P_r	reactive probability density
$P_0^\infty(i)$	asymptotic zero-order local moment of the probability density (discrete)
$P_0^\infty(\mathbf{r})$	asymptotic zero-order local moment of the probability density (continuous)
Pe	Peclet number
Pe_T	Taylor-Peclet number
Q	solvent volumetric flow rate
R_s	separation resolution
t	time
t_R	total device residence time
t_u	unit cell residence time
$U(j)$	edge velocity
$\bar{U}^*$	mean solute velocity
$\hat{U}^*$	normalized mean solute velocity

$v(i)$	node volume
$v_e(j)$	edge volume
$\bar{v}$	average velocity
V	probabilistic volume
W	channel width
X_i	position of band i

A.1.2 Greek

α	empirical trapping time parameter
β	reactive porous medium parameter
γ	reactive porous medium parameter
$\delta(t)$	Dirac delta function
$\delta_{i,j}$	Kronecker delta function
ε	ratio of trapping time-scale to convection time-scale
$\epsilon(j)$	generic edge parameter
η	solvent viscosity
θ_{FX}	angle between the applied force and the X-axis
θ_{UF}	angle between the mean velocity and applied force
θ_{UX}	angle between the mean velocity and the X-axis
λ	fractional length of the edges
μ	ratio of electrophoretic mobilities
μ_j	electrophoretic mobility in edge j
μ_0	freely draining electrophoretic mobility
σ	standard deviation of solute band
σ_i	standard deviation of solute band i

τ	trapping time
τ_0	unit cell volume
$\partial\tau_0$	unit cell surface area
τ_X	serpentine tortuosity
τ^*	empirical trapping time parameter
$\phi(i)$	generic vertex paramter
ϕ_a	volume fraction of well a
ϕ_b	volume fraction of well b
ϕ_e	volume fraction of the edges
φ	serpentine total flow rate
$\psi(i)$	vertex field

A.2 Vectors

A.2.1 Roman

$\mathbf{A}$	fictitious initial conditions
$\mathbf{b}(j)$	difference in $\mathbf{B}$ across an edge (unit-cell)
$\tilde{\mathbf{b}}(j)$	difference in $\mathbf{B}$ across an edge (macroscopic)
$\mathbf{B}(i)$	$\mathbf{B}$ field (discrete)
$\mathbf{B}(\mathbf{r})$	$\mathbf{B}$ field (continuous)
$\bar{\mathbf{B}}$	total weighted $\mathbf{B}$
$\mathbf{e}(j)$	edge unit vector
$\mathbf{F}$	applied force
$\mathbf{i}_x$	unit vector
$\mathbf{I}$	discrete position
$\mathbf{I}_0$	initial discrete position

$\mathbf{J}$	non-reactive flux density
$\mathbf{J}_r$	reactive flux density
$\mathbf{J}_0^\infty$	asymptotic flux density
$\mathbf{l}_k$	basic lattice vector
$\mathbf{P}$	asymptotic zeroth-order probability densities
$\mathbf{r}$	continuous position vector
$\mathbf{r}_{i_0}$	initial continuous position vector
$\mathbf{R}$	global continuous position vector
$\mathbf{R_I}$	discrete position vector
$\mathbf{R}_{\mathbf{I}_0}$	initial discrete position vector
$\mathbf{R}_{\mathcal{I}_0}$	initial global-discrete position vector
$\mathbf{R}(j)$	macroscopic jump vector
$\mathbf{U}(j)$	edge velocity vector
$\mathbf{U}(\mathbf{r})$	solute velocity vector (continuous)
$\bar{\mathbf{U}}^*$	mean solute velocity vector
$\hat{\bar{\mathbf{U}}}^*$	average velocity unit vector
$< \mathbf{U}^C >_j$	average edge convective solute velocity
$< \mathbf{U}^F >_j$	average edge force-driven solute velocity
$\mathbf{v}$	node volume vector
$\mathbf{V}$	arbitrary vector
$\mathbf{x}$	position vector
$\hat{\mathbf{x}}$	unit vector
$\hat{\mathbf{X}}$	unit vector
$\hat{\mathbf{y}}$	unit vector
$\hat{\mathbf{Y}}$	unit vector

A.2.2 Greek

$\alpha(i)$	forcing function
$\xi_H(e_j)$	cocycle vector

A.3 Tensors and Matrices

A.3.1 Roman

$\mathcal{A}$	coefficient matrix for $\mathbf{P}$
$\mathbb{B}$	matrix of $\mathbf{b}(j)$
$\mathcal{B}^+$	transition matrix
$\mathcal{B}^-$	transition matrix
$\mathbf{c}$	convective volumetric flow rate matrix
$\mathbf{d}$	diffusive volumetric flow rate matrix
$\bar{\mathbf{D}}^*$	solute dispersivity dyadic
$\mathbf{D}$	incidence matrix
$\mathbf{D}(\mathbf{r})$	solute diffusivity dyadic (continuous)
$\mathbf{D}(j)$	solute diffusivity dyadic (discrete)
D_{ij}	incidence matrix
$\mathbf{E}$	a dyadic
$\mathbf{J}_m$	moment flux density
$\mathbf{k}$	reaction matrix
$\mathbf{K}(K_{ij})$	cocycle matrix
$\mathbf{H}$	a dyadic

$< \mathbf{M} >_j$	average mobility dyadic in edge j
$\bar{\mathbf{M}}^*$	chromatographic mobility dyadic
$\mathbf{M}_m$	m^{th} global moment (weighted)
$\mathbf{M}'_m$	m^{th} global moment (unweighted)
$\mathbf{M}_{mr}$	reactive total moments
$\mathbf{P}_m$	m^{th} local moment
$\mathbf{v}$	volume matrix

A.3.2 Greek

α^*	cocycle attenuated forcing function
β^+	difference in $\mathbf{B}$ vectors
β^-	difference in $\mathbf{B}$ vectors
$\beta(i)$	forcing function on $\mathbf{H}$
Γ_m	forcing function for $\mathbf{P}_m$
$\Pi_{ij}^{(+)}$	entering incidence matrix
$\tilde{\Pi}_{ij}^{(+)}$	conditioned entering incidence matrix
$\Pi_{ij}^{(-)}$	exiting incidence matrix
$\tilde{\Pi}_{ij}^{(-)}$	conditioned exiting incidence matrix
ζ	arbitrary tensor valued function

A.4 Graphs, Sets and Spaces

E	edge space
H	cocycle space
$\mathcal{I}$	$l \oplus L$ discrete global space
$\mathcal{L}$	derived lattice
$\mathbf{R}$	$l \oplus L$ continuous global space
$\mathbf{R}_\infty$	domain of the continuous space
V	vertex space
Γ_b	basic graph
Γ_g	global graph
Γ_l	local graph
Λ	simple lattice
$\Omega^+(i)$	set of entering edges incident to i
$\Omega^-(i)$	set of exiting edges incident to i

A.5 Operators

L	discrete convection-diffusion-reaction operator [eq. (6.5)]
min	minimum
Re	real part
sym	symmetry operator [eq. (5.42)]
$\dagger$	transpose operator
$\bar{\zeta}$	ensemble average operator
$\|\zeta\|$	jump operator